



Delft University of Technology

## From micro-mechanisms of damage initiation to constitutive mechanical behavior of bainitic multiphase steels

Shakerifard, Behnam

**DOI**

[10.4233/uuid:230fffcf-b313-4f9f-bec0-e619bc62b0d4](https://doi.org/10.4233/uuid:230fffcf-b313-4f9f-bec0-e619bc62b0d4)

**Publication date**

2019

**Document Version**

Final published version

**Citation (APA)**

Shakerifard, B. (2019). *From micro-mechanisms of damage initiation to constitutive mechanical behavior of bainitic multiphase steels*. [Dissertation (TU Delft), Delft University of Technology].  
<https://doi.org/10.4233/uuid:230fffcf-b313-4f9f-bec0-e619bc62b0d4>

**Important note**

To cite this publication, please use the final published version (if applicable).

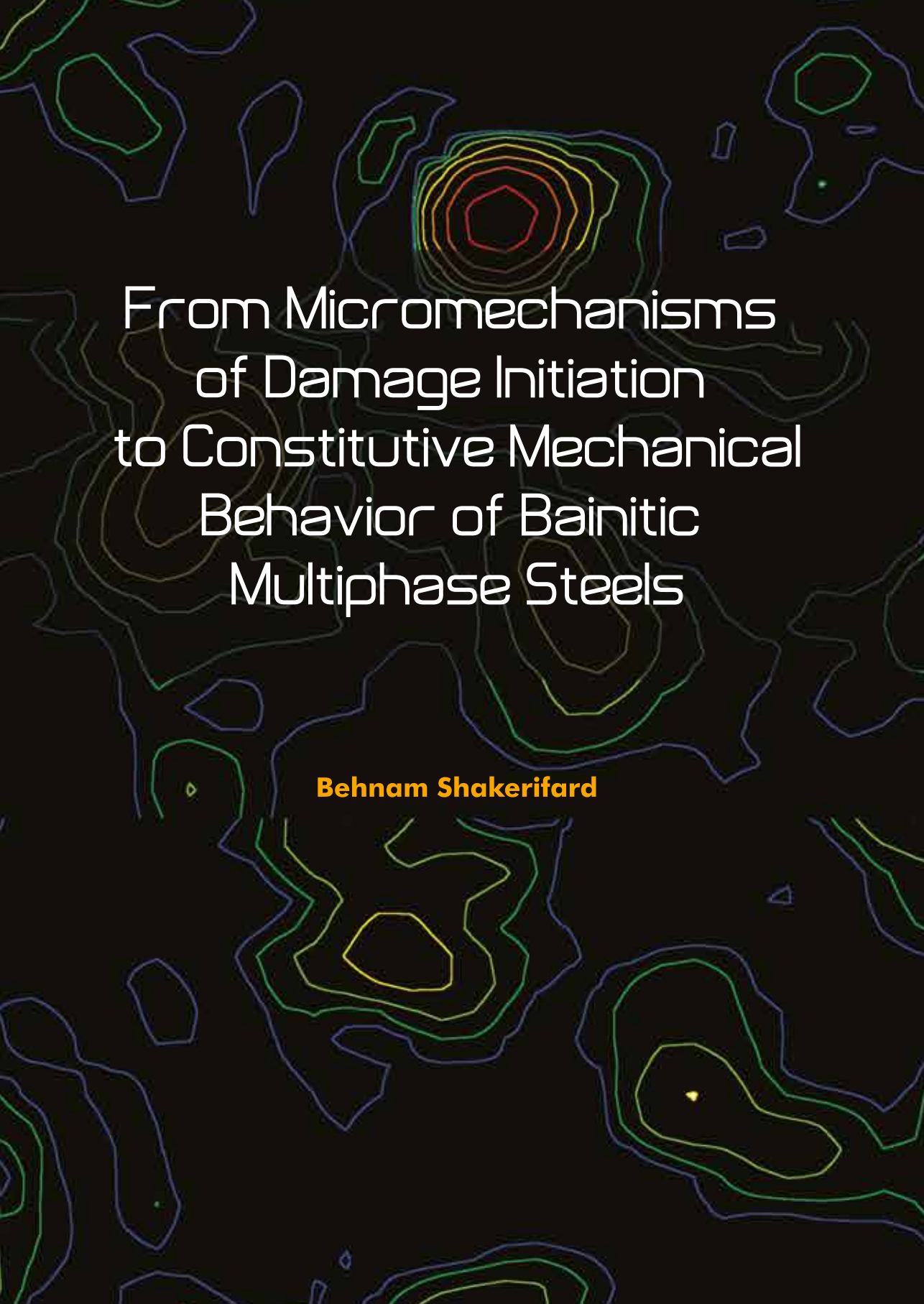
Please check the document version above.

**Copyright**

Other than for strictly personal use, it is not permitted to download, forward or distribute the text or part of it, without the consent of the author(s) and/or copyright holder(s), unless the work is under an open content license such as Creative Commons.

**Takedown policy**

Please contact us and provide details if you believe this document breaches copyrights.  
We will remove access to the work immediately and investigate your claim.



# From Micromechanisms of Damage Initiation to Constitutive Mechanical Behavior of Bainitic Multiphase Steels

**Behnam Shakerifard**



# Propositions

Accompanying the dissertation

## From micro-mechanisms of damage initiation to constitutive mechanical behavior of bainitic multiphase steels

Behnam Shakerifard

1. It is possible to estimate the strain rate sensitivity of steels without performing high strain rate tests (from thesis).
2. It is important to first understand the involved hierarchical failure processes and their importance in fracture and then study the involved micro-mechanisms (from thesis).
3. In bainitic multiphase steels, it is essential to control the macroscopic response of the material not by delaying damage nucleation but rather by retardation of deformation localization, which is governed by the topology of 2nd phase constituents (from thesis).
4. The macroscopic mechanical response of polycrystalline aggregates is governed by their intrinsic statistical nature. Therefore, homogenization-based crystal plasticity models are more relevant than full-field methods (from thesis).
5. Strict regulations are detrimental for problem solving and human sympathy.
6. Scientific communities strongly need people with human empathy in order to internally communicate science.
7. Currently, society needs to invest more in social and human sciences than in technology.
8. Life is like metallography, there is always something to polish.
9. Being critical is not a trend, it is rather an intrinsic state of a mind.
10. Politics and ethics are often in conflict. It is necessary to practice more ethically in politics.

*These propositions are regarded as opposable and defendable, and have been approved as such by Prof. dr. ir. L.A.I. Kestens and Prof. dr. ir. J. Sietsma.*



# **From micro-mechanisms of damage initiation to constitutive mechanical behavior of bainitic multiphase steels**

## **Dissertation**

For the purpose of obtaining the degree of Doctor of Philosophy

at Delft University of Technology

by the authority of the Rector Magnificus, prof. dr. ir. T.H.J.J. van der Hagen,

chair of the Board of Doctorates

to be defended publicly on

Monday 24<sup>th</sup> of June 2019

By

**Behnam SHAKERIFARD**

Master of Science in Materials Science and Engineering,

Delft University of Technology, the Netherlands.

Born in Mashhad, Iran

This dissertation has been approved by the promoters:  
Prof. dr. ir. L. A. I. Kestens  
Dr. J. Galan Lopez

**Composition of the doctoral committee:**

Rector Magnificus,	chairperson
Prof. dr. ir. L. A. I. Kestens	Delft University of Technology, promoter
Dr. ir. J. Galan Lopez	Delft University of Technology, copromoter

**Independent Members:**

Prof. dr. ir. J. Sietsma	Delft University of Technology, the Netherlands
Prof. dr. ir. A. Van Bael	Catholic University of Leuven (KU Leuven), Belgium
Prof. dr.ir. L. Delannay	Catholic University of Leuven (UC Louvain), Belgium
Prof. dr.ir. R. Petrov	Ghent University of Technology, Belgium
Dr. S. M. C. van Bohemen	TATA Steel, IJmuiden, the Netherlands

**Reserved Member:**

Prof. dr. I. Richardson	Delft University of Technology, Netherlands
-------------------------	---

The research described in this thesis was carried out in the MPMP group, Department of Materials Science and Engineering, Faculty of Mechanical, Maritime and Materials Engineering.



Keywords: Steel; Damage; Dynamic properties; Crystal Plasticity.

Printed by: IPSKAMP Printing

Front & Back: Demonstrate the crystallographic orientation and topological mechanisms leading to damage initiation

Copyright © 2019 by B. Shakerifard,

ISBN 978-94-028-1514-6

An electronic version of this dissertation is available at <https://repository.tudelft.nl/>

Author email: [b.shakerifard@tudelft.nl](mailto:b.shakerifard@tudelft.nl) / [behnam.shakerifard@gmail.com](mailto:behnam.shakerifard@gmail.com)



*To my parents and lovely sister ...*



## Summary

Global warming, continuous demand on energy from fossil fuels as a limited natural resource, and customers' high expectations regarding product quality are three global challenges that the automotive industry is facing. Fuel consumption reduction has a significant impact on preserving fossil fuels, lowering fossil fuel dependency and the CO<sub>2</sub> emissions that result in global warming. Weight reduction of car bodies, as so called Bodies-In-White (BIW), is one possible solution that the automotive industry can invest on. However, there are other conflicting parameters to weight reduction such as passenger safety and formability, which need to be considered simultaneously.

Although lightweight metals in vehicles have been used more and more over the last three decades, steel alloys are still a promising candidate for the structural components of BIW and chassis. This is true for economic and technological reasons. Steel production is cheaper than that of aluminum and magnesium, and it is associated with centuries worth of experience and knowledge.

In recent years, second-generation Advanced High Strength Steels (AHSSs) have been a landmark in terms of superior improvement in ductility, with strength comparable to that of the first generation. However, the high production cost due to alloying elements and the delayed cracking of Twinning-Induced Plasticity steel grades after formability process are the main obstacles of this generation for extensive implementation in automotive vehicles. All the drawbacks of the first and second generations of AHSSs provide an opportunity for researchers and steel manufacturers to develop the third generation of AHSSs.

The third generation of AHSSs is expected to fill the gaps and solve the drawbacks of the two previous generations. Bainitic steels with second phase constituents (*i.e.* martensite and retained austenite) are an example of third generation steels.

Understanding complicated multiphase microstructures and their role in damage initiation in order to improve the macroscopic mechanical response and formability for the automotive application is crucial and challenging. Many researchers have addressed this challenge via computational modelling and experiments. However, there are still aspects which need further study by both advanced experimental and modelling techniques.

The aim of this thesis is to address the micro-mechanisms of damage initiation in bainitic multiphase steels under static loading condition. This study reveals if there is any hierarchical correlation between

damage and forming behavior. In order to achieve this goal, advanced experimental characterization techniques and Crystal Plasticity (CP) based model are used. In order to understand the dynamic mechanical response of bainitic multiphase steels under high strain rate deformations (*i.e.* crash events and some forming processes), high strain rate mechanical tests are carried out.

The quasi-static and dynamic mechanical response of bainitic multiphase steel are studied in chapter 4. A positive strain rate sensitivity is observed for the all bainitic steels under consideration in this thesis. It is shown that tensile properties (both strength and ductility) are increased at high strain rates resulting in improvement of energy absorption. It is also shown that the presence of second phase constituents decreases the strain rate sensitivity. It is demonstrated that the finer microstructure exhibits a lower strain rate sensitivity. Moreover, a comprehensive literature survey on various steel grades in chapter 4 revealed that steels with higher strength demonstrate lower strain rate sensitivity. This correlation is approximated by a power law function, in which the strain rate sensitivity factor of the Johnson-Cook model is correlated to the yield stress at the reference strain rate (quasi-static).

Many studies have been conducted by advanced characterization and modelling techniques on first generation advanced high strength steels to understand the damage initiation micro-mechanisms. This has led to a good understanding on the role of phase contrast and topology in the formation of stress/strain partitioning between soft and hard phases. Eventually, at a critical moment these incompatibilities are locally relaxed by nucleation of voids in the context of the ductile failure process. However, a critical question is, whether all these various mechanisms leading to void nucleation, involved at different length scales, are equally important for the global failure of the material. The answer to this question strongly depends on the intrinsic character of materials. Particularly, the global mechanical response of the polycrystalline materials is governed by its microstructure, which is of a statistical nature. Bearing this in mind, it is observed that bainitic multiphase steels demonstrate a delay in damage initiation at the bainite/martensite interface compared to the first generation of advanced high strength steels (*i.e.* dual phase and interstitial-free steels), in which voids are nucleating at terminal stages of deformation prior to the final failure. Subsequently, in chapter 5, it is shown that the failure of the material is not the direct consequence of earlier damage nucleation and even higher volume fraction of the nucleated voids but rather the deformation localization is the key factor leading to global fracture. The meso-scale arrangement of the hard phase (martensite) determines whether or not the material goes through the deformation instability at an earlier stage and thus fractures at lower strain levels. The martensite banding phenomenon is shown to have a detrimental effect on the global mechanical response of bainitic multiphase steels by promoting local shear band formation and thus deformation instability. The topology of martensite bands has two different effects: first on void nucleation activity, and second on promoting deformation instability. The coarser and more connected network of martensite bands results in a lower void nucleation activity while it causes earlier

deformation localization. However, the finer and more fragmented networks of martensite bands leads to a higher void nucleation activity while it delays deformation localization.

Despite the vast efforts that have been spent to develop experimental and modelling tools to understand the role of micro-mechanical heterogeneities and their topology in damage nucleation, few methods have been proposed to resolve the crystallographic orientation aspect of damage initiation. In chapter 6, a new electron backscatter diffraction (EBSD) based method was examined to address the correlation between crystallographic orientation and void initiation. In this regard, 33 voids are analysed using the Orientation Distribution Function (ODF). By comparing the deformation texture at the uniform strain region (UODF) with the Voids-ODF (VODF), it is observed that after void nucleation, stress relaxation is governed by the growth process of voids rather than local plasticity around the voids. In other words, although voids act as stress concentrators, the stress is dominantly relaxed by the void growth process. Therefore, it is expected that VODF may reveal the orientations from which damage will initiate. However, it is important to mention that these orientations around voids experience some rotations during further plasticity. This is observed as a result of small deviation between VODF and UODF.

In chapter 7, the Visco-Plastic Self-Consistent (VPSC) crystal plasticity based model with a physical hardening model provides a strong tool to predict the anisotropic flow behaviour of bainitic multiphase steels under various loading conditions. The VPSC model is not considered as a damage model among the continuum damage models. However, it is used to predict the damage initiation sites in the Euler orientation space based on the evolution of stress/strain components and their partitioning between orientations of polycrystalline aggregate. The model calculates the stress/strain components of each grain at any desired macroscopic strain level based on various parameters such as crystallographic orientation, dislocation density, grain size and phase fractions. Various components of the strain tensor are considered and it is shown that the  $\varepsilon_{23}$  component exhibits the highest difference (incompatibility) between all the simulated grains and phases. This strain component is visualised in the Euler orientation space in order to be compared with the VODF map. It is observed that the most damaged orientations coincide with maximum and minimum values of the  $\varepsilon_{23}$  strain component. However, this correspondence is not observed completely with the equivalent von Mises strain map. Therefore, this may explain the fact that in order to study damage initiation critical strain components that may induce damage need to be considered.

Eventually, the general outcomes of this research work are concluded and summarised in chapter 8.



## Samenvatting

De opwarming van de aarde, de continue vraag naar energie van fossiele brandstof als uitputbare natuurlijke grondstof en de hoge verwachtingen van de consument omtrent de kwaliteit van producten zijn drie wereldwijde uitdagingen waarmee automobiel-industrie geconfronteerd wordt. Het verminderen van het brandstofverbruik heeft een significante impact op het behoud van fossiele brandstoffen, de afhankelijkheid van fossiele brandstoffen en de CO<sub>2</sub> uitstoot met als gevolg de opwarming van de aarde. Het verminderen van het gewicht van de carrosserie van een auto, de zogenaamde ‘Bodies-in-White’ (BIW), is één van de mogelijke oplossingen waarop de automobielsector kan inzetten. Er zijn echter ander ook parameters die tegen gewichtsvermindering ingaan, zoals de veiligheid van passagiers en de vervormbaarheid die tegelijkertijd in overweging genomen moeten worden.

Hoewel lichtgewicht metalen in voertuigen meer en meer gebruikt werden in de laatste dertig jaar zijn staallegeringen nog steeds een veelbelovende kandidaat als structurele component van de BIW en het chassis. Dit is het geval vanuit economisch en technologisch oogpunt. Staalproductie is goedkoper dan aluminium- en magnesiumproductie en is gebaseerd op eeuwenlange ervaring en kennis.

Tweede generatie geavanceerde stalen met grote sterkte (advanced high strength steels, AHSSs) zijn de afgelopen jaren een mijlpaal geweest wat betreft vooruitgang in ductiliteit, met sterktes vergelijkbaar met de eerste generatie. Echter, de hoge productiekosten door legeringselementen en de vertraagde breuk van TWIP-stalen na het vervormingsproces vormen de voornaamste obstakels voor uitgebreide toepassing in voertuigen van deze generatie staal.

De verwachting is dat de derde generatie AHHSSs de tekortkomingen en nadelen van de eerste twee generaties zal oplossen. Bainitisch staal met tweede fase componenten (Martensiet en overgebleven Austeniet) zijn een voorbeeld van derde generatie staal.

Het begrijpen van de gecompliceerde meerfase microstructuren en hun rol in schade-initiatie, om de macroscopische mechanische respons en de vervormbaarheid voor automobieltoepassingen te verbeteren, is cruciaal en uitdagend. Veel onderzoekers zijn deze uitdaging aangegaan met behulp van computermodellering en experimenten. Er zijn echter nog

aspecten die verder onderzoek vereisen met geavanceerde experimentele en modelleertechnieken.

Het doel van dit proefschrift is om de micro-mechanismen van schade-initiatie in bainitisch multifase staal onder statische belasting te bestuderen. Dit onderzoek onthult of er enige hiërarchische correlatie is tussen schade en vervormingsgedrag. Hiertoe worden geavanceerde experimentele karakteriseringstechnieken en een model voor kristalplasticiteit gebruikt. Om de dynamische mechanische respons van de bainitische multifasestalen onder snelle rekvervormingen (bijvoorbeeld botsingen en sommige vervormingsprocessen) te begrijpen, worden er mechanische testen met hoge reksnelheden uitgevoerd.

De quasi-statische en dynamische mechanische respons van bainitisch meerfase staal wordt bestudeerd in hoofdstuk 4. Een positieve gevoeligheid voor reksnelheid wordt waargenomen voor alle bainitische stalen die bekeken zijn in dit onderzoek. Er wordt getoond dat rekeigenschappen (zowel sterkte als ductiliteit) beter worden op hoge vervormingssnelheid, wat leidt tot verbeterde energie-opname. Er wordt ook getoond dat de aanwezigheid van tweede fase componenten de gevoeligheid voor reksnelheid verlaagt. Er wordt aangetoond dat de fijnere microstructuur een lagere gevoeligheid voor reksnelheid vertoont. Daarnaast toonde een uitgebreid literatuuronderzoek naar diverse staalsoorten in hoofdstuk 4 aan dat sterkere stalen minder gevoelig zijn voor reksnelheid. Dit verband kan worden benaderd met een machtswet waarin de gevoelighedsfactor voor reksnelheid uit het Johnson-Cook model gecorreleerd wordt aan de rekgrens bij de referentie-reksnelheid (quasi-statisch).

Veel onderzoek aan eerste generatie AHSSs is uitgevoerd d.m.v. geavanceerde karakterisering- en modelleringstechnieken, om de micro-mechanismen voor schade-initiatie te begrijpen. Dit heeft geleid tot een goed begrip van de rol van fasecontrast en topologie in de formatie van spanning/rekverdeling tussen zachte en harde fasen. Op een kritiek punt worden deze mispassingen uiteindelijk lokaal gerelaxeerd door nucleatie van holtes als onderdeel van het ductiel falen. Een cruciale vraag hierbij is of de diverse mechanismen die tot vorming van holtes leiden, die zich op verschillende lengteschalen afspelen, even belangrijk zijn voor het overall falen van het materiaal. Het antwoord op deze vraag is sterk afhankelijk van het intrinsieke karakter van materialen. Vooral de overall mechanische respons van polykristallijn materiaal wordt bepaald door de microstructuur, die statistisch van aard is. Met dit in gedachten wordt er waargenomen dat in bainitisch multifase staal schade aan het bainitisch/martensitisch grensvlak vertraagd begint vergeleken met de eerste generatie AHSS (d.w.z. tweefase en

interstitieel-vrije stalen), waarin holtes nucleören tegen het einde van de deformatie voor het uiteindelijke falen. Daarop wordt in hoofdstuk 5 getoond dat het falen van het materiaal niet het directe gevolg is van eerdere schadenuucleatie of zelfs niet van een hogere volumefractie genucleerde holtes, maar dat eerder de gelocaliseerde deformatie de centrale factor is die tot overall falen leidt. De mesa-schaal verdeling van de harde fase (martensiet) bepaalt of het materiaal wel of niet in een vroeg stadium een deformatie-instabiliteit doormaakt en dus breekt bij lage rek. Het fenomeen van bandvorming in martensiet blijkt een negatief effect te hebben op de overall mechanische respons van bainitisch meerfase staal doordat het de formatie van lokale afschuivingsbanden veroorzaakt en dus instabiliteit in de deformatie. De verdeling van martensietbanden heeft twee verschillende effecten: ten eerste op het nucleeren van holtes, en ten tweede op het bevorderen van instabiliteit in de deformatie. Een grover en meer verbonden netwerk van martensietbanden resulteert in een verminderde nucleatie van holten terwijl het een eerdere localisatie van de deformatie veroorzaakt. Echter, fijnere en meer gefragmenteerde netwerken van martensietbanden leiden tot meer nucleatie van holten terwijl ze localisatie van deformatie vertragen.

Grote inspanningen zijn gedaan om experimentele en modelleringstechnieken te ontwikkelen om de rol van micro-mechanische heterogeniteiten en hun verdeling in het nucleeren van schade te begrijpen. Desondanks zijn er maar weinig methoden voorgesteld om kristallografische oriëntatie-aspecten van het initiëren van schade te verduidelijken. In hoofdstuk 6 is gekeken naar een nieuwe EBSD methode om de correlatie tussen kristallografische oriëntatie en het nucleeren van holtes te bekijken. Hiertoe zijn 33 holten geanalyseerd met de Oriëntatie Verdelingsfunctie (Orientation Distribution Function, ODF). Door de deformatietextuur in de uniform gerekte regio (UODF) te vergelijken met de holten-ODF (Voids-ODF, VODF) wordt het duidelijk dat na nucleatie van holten de relaxatie van spanningen wordt bepaald door het groeiproces van holten en niet door de lokale plasticiteit rond holten. Anders gezegd, hoewel holten spanningen concentreren wordt spanning voornamelijk gerelaxeerd door relaxatie bij de groei van holten. Daarom valt te verwachten dat VODF zal verduidelijken vanuit welke oriëntaties schade initieert. Het is echter belangrijk erop te wijzen dat deze oriëntaties tijdens verdere plasticiteit ietwat zullen roteren. Dit resulteert in een klein verschil tussen VODF en UODF uitkomsten.

In hoofdstuk 7 geeft het Visco-plastisch Zelf-consistent (Visco-Plastic Self-Consistent, VPSC) kristalplasticiteit-gebaseerde model met het een fysisch hardingsmodel een krachtig middel om anisotroop vervormingsgedrag van bainitisch meerfase staal onder diverse belastingen te

modelleren. Het VPSC model wordt niet gezien als een schademodel onder de continuum schademodellen. Desondanks wordt het gebruikt om de initiëring van schade in de Eulerruimte, gebaseerd op de evolutie van spanning/rekcomponenten en hun verdeling tussen orientaties van polykristallijne aggregaten te voorspellen.

Het model berekent de spanning/rek-onderdelen van iedere korrel voor ieder gewenst macroscopisch reknivo gebaseerd op diverse parameters zoals kristallografische oriëntatie, dislocatiedichtheid, korrelgrootte en fasefracties. Diverse componenten van de rektensor worden meegenomen er er wordt getoond dat de  $\varepsilon_{23}$ -component het grootste verschil (incompatibiliteit) toont tussen alle gesimuleerde korrels en fasen. Deze rekcomponent wordt gevisualiseerd in de Eulerruimte om vergeleken te worden met het VODF overzicht. Er wordt waargenomen dat de meest beschadigde oriëntaties degenen zijn met maximale en minimale waarden van de  $\varepsilon_{23}$  rekcomponent. Echter, deze overeenstemming wordt niet volledig waargenomen met het equivalente von Mises rekoverzicht. Dit verklaart daarom mogelijk waarom kritische rekcomponenten die mogelijk schade induceren moeten worden meegenomen om initiatie van schade te bestuderen.

Aan het einde worden de algemene resultaten van dit onderzoek samengevat in hoofdstuk 8.

# Contents

List of Figures .....	I
List of Tables .....	VI
Chapter 1 Introduction.....	1
1.1    Steels development in automotive industry .....	1
1.2    The importance of failure mechanisms on BIW formability prediction.....	3
1.3    Thesis objective and outline.....	4
References.....	6
Chapter 2 Literature review: Strain rate dependence of mechanical properties and ductile failure micro-mechanisms.....	7
2.1    Introduction.....	7
2.2    Strain rate dependence of mechanical properties.....	9
2.3    Ductile failure mechanisms.....	12
2.3.1    Phase contrast and topology.....	14
2.3.2    Crystallographic orientation.....	18
References.....	21
Chapter 3 Materials and methodology.....	23
3.1    Materials .....	24
3.1.1    High silicon grade .....	24
3.1.2    Low silicon grade.....	25
3.1.3    Laboratory setup and for hot and cold rolling .....	26
3.1.4    Dilatometry .....	27
3.1.5    Vatron annealing simulator .....	28
3.2    Mechanical test .....	29
3.2.1    Micro-hardness test.....	29
3.2.2    Tensile test .....	29
3.2.3    Split Hopkinson Tensile Bar .....	31
3.3    Digital Image Correlation (DIC).....	34

3.4	Microstructure characterization .....	35
3.4.1	Inclusions .....	36
3.4.2	Grain size .....	36
3.4.3	Constituents characterization .....	37
3.4.4	X-ray Diffraction .....	37
3.4.5	Wavelength Dispersive Spectroscopy.....	37
3.5	Crystal orientation mapping.....	38
3.6	Damage quantification and image processing .....	39
3.7	Plastic deformation modelling .....	40
3.7.1	Johnson-Cook model .....	41
3.7.2	Visco-Plastic Self-Consistent (VPSC) model.....	41
	References.....	49
Chapter 4	Strain rate dependent dynamic mechanical response of bainitic multiphase steels	
	51	
4.1	Introduction.....	52
4.2	Results.....	53
4.2.1	Microstructure characterization .....	53
4.2.2	Mechanical response.....	56
4.2.3	Flow behavior modelling .....	59
4.3	Discussion .....	61
4.4	Conclusion .....	67
	References.....	68
Chapter 5	Effecting of banding on micro-mechanisms of damage initiation in	
	bainitic/martensitic steels .....	69
5.1	Introduction.....	70
5.2	Results.....	71
5.2.1	Microstructure characterization .....	71
5.2.2	Micro-hardness .....	73
5.2.3	Tensile properties.....	74
5.2.4	Damage analysis .....	75
5.2.5	Fractography .....	82
5.3	Discussion .....	83
5.4	Conclusion .....	86
	References.....	87
Chapter 6	Crystallographically resolved damage initiation in advanced high strength steels	
	89	
6.1	Introduction.....	90
6.2	Results and discussion .....	91

6.2.1	Mechanical response .....	91
6.2.2	Void mapping.....	91
6.2.3	Correlation between crystallographic orientation and damage .....	93
6.3	Conclusion .....	97
References.....		98
Chapter 7	Crystal plasticity based modelling of bainitic/martensitic steels .....	99
7.1	Introduction.....	100
7.2	Material definition .....	102
7.2.1	Mechanical parameters .....	103
7.2.2	Material texture and microstructural parameters .....	103
7.3	Fitting of model parameters .....	106
7.3.1	Input data .....	106
7.3.2	Modelling of tensile test.....	107
7.3.3	Fitting procedure .....	107
7.3.4	Deformation mode .....	108
7.4	Results and discussion .....	108
7.4.1	Mechanical response under static and dynamic loading conditions .....	109
7.4.2	Model sensitivity to microstructural variables.....	110
7.4.3	Damage prediction .....	112
7.5	Conclusion .....	119
References.....		121
Chapter 8	Conclusion .....	123
8.1	Abstract .....	123
8.2	Summary .....	124
Appendix A	Transformation diagrams .....	A-1
A.1	Continuous Cooling Transformation (CCT) diagrams .....	A-1
A.2	Time Temperature Transformation (TTT) diagrams .....	A-2



# List of Figures

Figure 1-1. Elongation at fracture against tensile strength of 3 steel generations. Diagram based on the World Auto Steel. ....	2
Figure 2-1 Microstructure of a bainitic steel with bainite (B), martensite (M) and retained austenite (A):(a) Scanning and (b) Transmission electron micrographs. $\alpha$ is the bainitic ferrite, $\gamma$ is the thin film of A and M/A shows the martensite and austenite islands [3]. ....	8
Figure 2-2 Dash crash box structure [13, 15]. ....	9
Figure 2-3 Comparison of static and dynamic FLD's for S235, DC04, AISI409 and CMnAl TRIP[16]. The region under the V-curve is considered as a safe region. ....	10
Figure 2-4 Schematic illustration of critical stress for the initiation of martensite transformation as a function of temperature [18-20]. ....	11
Figure 2-5. An example of damage mechanisms at different length scales which lead to global failure: (a) a high strain rate ( $687 \text{ s}^{-1}$ ) tensile deformation of a bainitic steel loaded along Rolling Direction (RD), (b) contiguous collection of $\sim 1000$ SEM micrographs of the fracture sample in (a), (c) the corresponding image processed version of (b) with clear distribution of voids and (d) etched microstructure of the fractured bainitic multiphase steel introduced in chapter 3. ....	14
Figure 2-6 Local critical strain for damage nucleation in a DP steel corresponding to different damage mechanisms with respect to: (a) damage inside ferrite grains F or inside martensite islands M; (b) average angle $\theta$ between ferrite grain boundary segment and tensile direction ( $\pm 5^\circ$ ) for ferrite grain boundary F/F damage; (c) ferrite channel width for martensite/ferrite phase boundary M/F damage; and (d) phase boundary radius at different bridging martensite M thickness for M/F damage. Corresponding microstructures are shown topologically [39]. ....	15
Figure 2-7 Damage micro-mechanisms in the DP steel: (a, b and c) schematic illustration of the involved damage micro-mechanisms with different microstructural configurations and (d) quantitative analysis of individual features corresponding to each damage mechanisms at each average global strain level [42]. ....	17
Figure 2-8 Nano-chemical analysis at a PAGB: (a) an example of EBSD image quality map and corresponding APT lift-out (SE image) of a PAGB-bearing martensite island and (b) illustrates the corresponding reconstructed APT data set [42]. ....	17
Figure 2-9 In-situ deformation of a micro-tensile specimen: (a, b and c) are the optical microscopy of the specimen at different strain levels, (d, e and f) distribution of equivalent strain and (g, h and i) distribution of equivalent stress analysed with consideration of the habit-plane-dependent yielding [55]. The distribution of equivalent stress and strains is derived from the CPFEM simulation. ....	19

Figure 2-10 CPFEM simulation of a micro-tensile specimen during the tensile deformation: (a, b and c) distribution of equivalent strain and (d, e and f) distribution of equivalent stress analysed without consideration of the habit-plane-dependent yielding [55]. .....	20
Figure 3-1 Schematic of the laboratory set-up for hot rolling at Tata Steel in IJmuiden. ....	26
Figure 3-2 Vatron annealing simulator at TKSE Duisburg and the corresponding schematic illustration of annealing cycles. ....	28
Figure 3-3 Schematic illustration of the tensile specimen geometry. Lt=83mm, Lc=37.5mm, L0=25mm, b0=6.25mm. ....	30
Figure 3-4 Split Hopkinson Tensile Bar (SHTB) setup at Ghent University: (a) SHTB specimen geometry and (b) SHTB setup. ....	32
Figure 3-5 Schematic demonstration of SHTB setup: a pneumatic force impulses the fork, which hits the impactor. The impactor is then accelerated towards to anvil of the input bar, generating an incident wave directed to the specimen [19]. ....	32
Figure 3-6 SHTB waves generation in the input and output bar: (a) LaGrange diagram of a SHTB experiment, where the length of the input and output bars are 6 m and 3.2 m, respectively. The arrows indicate whether the wave is in tension or compression. The vertical green lines indicate the placement of the strain gauges, in the regions of the bar where only one wave is present at a time. (b) Real signals measured by strain gauges [19]. ....	33
Figure 3-7 DIC analysis; (a) GL5 specimen with the speckle pattern at the gauge and (b) effective plastic strain calculation. ....	35
Figure 3-8 SEM micrographs of the inclusions and their corresponding chemical analysis:(a) a MnS stringer along the rolling direction (RD) and (b) Al2O3 particle. The x-axis of the curves is along the RD and the y-axis is along the normal direction (ND). ....	36
Figure 3-9 Principal components of an EBSD system.....	39
Figure 4-1. Strain rate sensitivity factor as a function of initial yield stress, i.e. A parameter of J-C model. C and G in the legend indicate whether the strain rate sensitivity was calculated or given respectively. ....	52
Figure 4-2. SEM micrographs (left) and IQ+phase maps (right) of the microstructures of the LoSi grade: (a and a2) HT sample, (b and b2) LT sample and (c and c2) LB sample. Dark regions, i.e. low IQ regions, of EBSD maps correspond to martensitic regions. ....	54
Figure 4-3. SEM micrographs (left) and IQ+phase maps (right) of the microstructures of the HiSi grade; (a and a2) HT sample, (b and b2) LT sample and (c and c2) SB sample. Dark regions of EBSD maps correspond to martensitic regions. ....	55
Figure 4-4. Engineering flow curves of all sample from both grades: (a, b and c) the flow curves of the HT, LT and LB samples from LoSi grade and (d, e and f) the flow curves of the HT, LT and SB samples from HiSi grade. The dashed curves are the high strain rate tests. ....	57
Figure 4-5. Ultimate tensile strength as a function of strain rates; (a) LoSi samples and (b) HiSi samples.....	58
Figure 4-6. DIC analysis; (a) uniform elongation as a function of strain rates and (b) displacement used as a virtual extensometer for the calculation of engineering strain. ....	58
Figure 4-7. Energy absorption of both HiSi and LoSi grades (a) at 5% of deformation and (b) at the UTS point.....	59
Figure 4-8. Experimental and simulated static and dynamic tensile curves for all the materials: (a, b and c) flow curves of the LoSi grade and (d, e and f) flow curves of the HiSi grade. ....	61

Figure 4-9. Strain rate sensitivity factor as a function of initial yield stress, i.e. A parameter of J-C model. C and G in the legend indicate whether the strain rate sensitivity was calculated or given, respectively. The green points are the C factors of the current studied materials. ....	62
Figure 4-10. The effect of retained austenite and martensite (M blocks+ATM) on UTS and uniform elongation of the HiSi grade samples: (a) influence of retained austenite on the uniform elongation and (b) influence of martensite on UTS and uniform elongation. ....	63
Figure 4-11. The dynamic to static true stress ratio as a function of the logarithmic dynamic to static strain rate for (a) LoSi samples and (b) HiSi samples. The slope indicates the strain rate sensitivity factor. ....	65
Figure 4-12. Strain rate sensitivity factor as a function of second phase constituents: (a) total fraction of martensite and RA and (b) total martensite fraction (M+ATM) versus RA fraction and strain rate sensitivity factor as a function of RA in the HiSi grade. ....	66
Figure 4-13. Correlation between grain size and mechanical properties: (a) initial yield stress A as a function of inverse square root of grain size and (b) strain rate sensitivity factor C as a function of grain size. ....	67
Figure 5-1. Microstructure characterization of both samples. The HT sample: (a) SEM micrograph where the dashed rectangle indicates the location of the EBSD analysis. The solid arrow is the position of the EPMA line analysis, (b) overlaid IQ and phase maps (solid white arrows show dark bands with low IQ value). The LT sample: (c) SEM micrograph, (d) overlaid IQ and phase maps. (e) EPMA chemical analysis with four arrows corresponding to the bands in the HT sample showed in (a) and (f and g) schematic illustration of the bands topology of the HT and LT samples, respectively. ....	72
Figure 5-2. Box plot of micro-hardness measurements of low and high temperature samples: (a) Vertical micro-hardness profile of the LT and HT samples austenized at 820 and 920°C performed with 10 gf load (Indentation is conducted every 50 $\mu\text{m}$ ), and (b) Horizontal micro-hardness measurements on the martensitic bands and the matrix of both samples loaded with 5 gf. ....	74
Figure 5-3. Engineering uni-axial tensile curve of the low and high temperature samples loaded along the RD. ....	75
Figure 5-4. SEM micrographs of the LT sample: (a and b) micrographs of the interrupted sample at 9.5% elongation RD parallel to loading direction (RD//LD) etched by Nital and (c and d) micrographs of the fractured sample (RD//LD) etched by Klemm. Dashed circles depict the carbide related voids. ....	77
Figure 5-5. SEM micrographs of the HT sample: (a and b) micrographs of the fractured sample (RD //LD) etched by Nital close to the fracture surface and (c and d) micrographs of the fractured sample (RD// LD) etched by Klemm. ....	78
Figure 5-6. Two EBSD analysis on the interrupted LT sample at the strain level of 9.5%. The Banded region is indicated by the two dashed lines and voids are indicated by white arrows: (a) Inverse pole figure (IPF) overlaid by image quality (IQ) map reveals a void initiated between two martensitic band along the shear band shown by yellow dashed lines and (b) a IPF+IQ map of another void initiated along a martensite band. ....	78
Figure 5-7. EBSD analysis on the interrupted HT sample at the strain level of 5%. The Banded region is indicated by the two dashed lines. (a) SEM micrographs, (b) IPF+IQ map, (c) KAM map and (a1, a2, and a3) the corresponding GROD and BC maps of regions indicated by dashed rectangle in the SEM micrograph 7(a). B, FB, ATM and M corresponds to bainite, fine bainite, tempered martensite and MA island, respectively. High angle grain boundaries ( $>15^\circ$ ) are	

indicated by the black line in GROD maps. White regions within GROD maps are pixels with low CI value.....	79
Figure 5-8. Approximately 1000 contiguous high resolution SEM micrographs (each $\approx$ 27x32 $\mu\text{m}^2$ ): (a) high temperature and (b) low temperature samples. Dashed circle lines are examples of MnS fracture and delamination from the matrix. ....	81
Figure 5-9. Void quantification: (a) void density vs. local true plastic strain and (b) void area fraction vs. local true plastic strain. ....	81
Figure 5-10. (a) Box plot of voids perimeter and (b) true plastic strain vs. distance from the fracture surface.....	81
Figure 5-11. SEM fractographs of the LT sample revealing features of both ductile and brittle fracture: (a) Fibrous (ductile)zone with traces of stair-like deformation slip called serpentine glide, (b) two regions of fracture including ductile and cleavage fracture and (c) Small traces of cleavage facets in the fibrous zone. ....	82
Figure 5-12. SEM fractographs of the HT sample revealing features of both ductile and brittle fracture: (a) Fibrous (ductile)zone with traces of stair-like deformation slip called serpentine glide, (b) two regions of fracture including ductile and cleavage fracture and (c) large traces of cleavage facets in the fibrous zone. ....	83
Figure 6-1. Engineering flow curve of the material under quasi-static loading condition. Mechanical properties calculated from the tensile curve. ....	91
Figure 6-2. Void mapping analysis: (a) distribution of voids within the microstructure (in order to enhance the visual contrast between voids and the background matrix, voids are enlarged approximately 100x) and (b) void area fraction and void density as a function of true plastic strain.....	92
Figure 6-3. Schematic illustration of orientation selection on an overlapped image quality and inverse pole figure map; (a) complete area of analysis, (b) area selected around the void with faces approximately equal to 3 times of a void diameter and (c) remaining area. ....	93
Figure 6-4. 3D void ODF (3D-VODF). Three $\varphi_2$ sections ( $\varphi_2=15, 45$ and $75^\circ$ ) consist of the dominant components with regard to voids orientations. ....	94
Figure 6-5. $\varphi_2=45^\circ$ section of ODFs of the material at two different deformation levels; (a) Uniform deformation UODF (calculated from 796000 data points), (b) post uniform VODF (131000 data points), (c) post uniform NVODF (460000 data points) and (d) Necking or post uniform ODF consist of the merged ODFs in b and c. ....	95
Figure 6-6. The overlapped VODF and UODF of the material at two different deformation levels; (a) $\varphi_2=15$ , (b) $\varphi_2=45$ , (c) $\varphi_2=75^\circ$ . ....	96
Figure 7-1. VPSC formalism: the behavior of individual grains at the microscopic scale and the whole polycrystal at the macroscopic scale are related by the micro-macro connection and the grain interaction scheme, based on the solution of the Eshelby problem. ....	102
Figure 7-2. $\varphi_2 = 45^\circ$ section of the orientation distribution function of the HT sample: (a) Bainite and (b) martensite. ....	104
Figure 7-3. $\varphi_2 = 45^\circ$ section of the orientation distribution function of the LT sample: (a) Bainite and (b) martensite. ....	104
Figure 7-4. Input data needed for the VPSC simulation for both HT and LT samples and their corresponding phases: (a) Grain aspect ratio and (b) Grain inclination with respect to the rolling direction. ....	105

Figure 7-5. Block diagram that shows how the Python script used to fit the material parameters (fitsx.py) reads experimental data and a template file to generate input for VPSC based on a guess of the parameters and, after running a VPSC90 simulation for each of the experiments, calculates a new guess for the parameters based on the error between simulated and experimental curves using the Levenberg–Marquardt algorithm [14]. .....	107
Figure 7-6. Comparison of the flow response between experiments and simulations: (a) The LT sample and (b) The HT sample. Data points demonstrate the experimental curves and lines are simulated curves at low (LD// RD and TD) and high strain rates (LD//RD). .....	110
Figure 7-7 Model sensitivity evaluation: (a) individual flow response of bainite and martensite, (b) influence of carbide volume fraction, (c) influence of GNDs and (d) grain size effect...	111
Figure 7-8. Orientation distribution function $\varphi_2 = 45^\circ$ of the HT sample: (a) texture calculated from interrupted tensile sample at 5% deformation and (b) simulated texture by VPSC at the similar strain level. .....	113
Figure 7-9. Orientation distribution function $\varphi_2 = 45^\circ$ of the HT sample: (a) texture calculated from the neck region of the fractured tensile sample and (b) simulated texture by VPSC at the strain level 75%.....	113
Figure 7-10. Evolution of maximum difference of strain and stress components ( $d\epsilon_{ij}$ and $ds_{ij}$ ) during the tensile test of HT sample until 75% of deformation: (a) stress components and (b) strain components. The blue curve demonstrates the true tensile curve of HT sample. .....	114
Figure 7-11. The $\varepsilon_{23}$ component maps at three different sections overlaid with VODF derived from section 6.2.3: (a) $\varphi_2=15^\circ$ , (b) $\varphi_2=45^\circ$ and (c) $\varphi_2=75^\circ$ . The VODF intensity lines are depicted at (c).....	116
Figure 7-12. The $\varepsilon_{\text{von Mises}}$ maps at three different sections overlaid with VODF derived from section 6.2.3: (a) $\varphi_2=15^\circ$ , (b) $\varphi_2=45^\circ$ and (c) $\varphi_2=75^\circ$ . The VODF intensity lines are depicted at (c).....	117
Figure 7-13. The $s_{33}$ maps at three different sections overlaid with VODF derived from section 6.2.3: (a) $\varphi_2=15^\circ$ , (b) $\varphi_2=45^\circ$ and (c) $\varphi_2=75^\circ$ . The VODF intensity lines are depicted at (c). .....	118

## List of Tables

Table 3-1 Chemical composition of the HiSi grade.....	25
Table 3-2. Chemical composition of the LoSi grade. ....	25
Table 3-3. Measured and calculated values of $Ac1$ , $Ac3$ , $Bs$ and $Ms$ for LoSi and HiSi (°C). .....	27
Table 3-4. Samples nomenclature and associated annealing cycles. ....	29
Table 4-1. Microstructural variables of LoSi samples. ....	56
Table 4-2. Microstructural variables of HiSi samples. ....	56
Table 4-3. Materials parameters used for the Johnson-Cook model. ....	60
Table 5-1. Microstructural variables of the high and low temperature samples.....	73
Table 5-2. Tensile properties of the high and low temperature samples along the RD. ....	75
Table 7-1 Average grain properties of both phases in the HT and LT samples. ....	105
Table 7-2 Microstructural variables: $v_f$ is the volume fraction of the phase, $d$ is the lath size, $\rho$ dislocation density, $v_c$ is the volume fraction of carbides and $d_c$ is the size of carbides. ....	105
Table 7-3. Fitted parameters in VPSC for both LT and HT samples (R-square = 0.96) except $C2$ and $\sigma_{imb2}$ , which were taken from [10]. ....	109
Table 7-4. Latent hardening coefficients. ....	109

# Chapter 1 Introduction

## 1.1 Steels development in automotive industry

Global warming, continuous demand on energy from fossil fuels as a limited natural resource, and customers' high expectations regarding product quality are three global challenges that the automotive industry is facing. Fuel consumption reduction has a significant impact on preserving fossil fuels, lowering fossil fuel dependency and the CO<sub>2</sub> emissions that result in global warming. Weight reduction of car bodies, as so called Bodies-In-White (BIW), is one possible solution that the automotive industry can invest on. It has been estimated that a reduction of 10% in the total vehicle weight could make 8 to 10 % gain in fuel efficiency [1]. However, there are other conflicting parameters to weight reduction such as passenger safety and formability, which need to be considered simultaneously. Generally, government policies are geared toward car safety enhancement. As an example, the National Highway Traffic and Safety Administration in the USA has a policy to enhance side impact intrusion performance and to increase the standard velocity for frontal crash tests [2]. Therefore, vehicle safety and integrity during a crash event are design consideration priorities. This is normally assessed by the energy absorption of the car BIW during a crash event, which is referred to as *crashworthiness*. Inevitably, simultaneously optimizing weight reduction, crashworthiness and formability is a challenge that material suppliers and researchers are confronting. This challenge has resulted in new strategies to improve the mechanical properties of steels, as the main metal used in BIW, and/or to incorporate new alternative lightweight materials such as aluminium and magnesium alloys.

Although lightweight metals in vehicles have been used more and more over the last three decades, steel alloys are still a promising candidate for the structural components of BIW and chassis. This is true for economic and technological reasons. Steel production is cheaper than that of aluminum and magnesium, and it is associated with centuries worth of experience and knowledge. The deep understanding of the role of chemical composition, heat treatment and forming processes resulted in technological advances in steel production and its performance. Consequently, different steel grades for various applications have been developed based on the required specifications and mechanical properties. The combined enhancement of strength and ductility is hard to achieve due to the intrinsic

conflicting behavior of these two properties. However, considerable understanding of microstructures and their micro-mechanical behavior has resulted in remarkable improvement in the properties of steels. A progressive combination of ductility and strength has enabled manufacturers to make the BIW with thinner sheets, which reduces weight while meeting stricter passenger safety requirements. Since, the late 1970s, three generations of Advanced High Strength Steels (AHSSs) have been developed [3]. Figure 1.1 illustrates these three generations of steel grades and reveals, qualitatively, their corresponding position inside the elongation and strength diagram.

Strengthening mechanisms such as solid solution hardening, precipitation, grain refinement and hardening by the presence of second phase constituents and phase transformation by plastic deformation (TRIP effect) have caused tremendous advances in strength. For instance, first-generation AHSSs such as Dual Phase (DP), Complex Phase (CP), TRansformation Induced Plasticity (TRIP) and Martensitic (MS) steels mainly benefit from second phase and hardening by TRIP effect as strengthening mechanisms. Their strength is three to five times that of low-strength steels, at the expense of ductility.

In recent years, second-generation AHSSs have been a landmark in terms of superior improvement in ductility, with strength comparable to that of the first generation. Aluminum-aided Lightweight with Induced Plasticity (L-IP), Austenitic Stainless Steels (AUST.SS) and TWinning Induced Plasticity (TWIP) are examples of this generation. However, the high production cost due to alloying elements and the delayed cracking of TWIP grades in particular [4] are the main obstacles of this generation for extensive implementation in automotive vehicles.

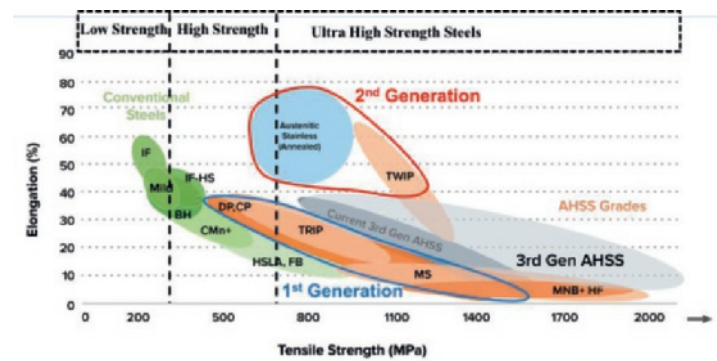


Figure 1-1. Elongation at fracture against tensile strength of 3 steel generations. Diagram based on the World Auto Steel.

All the drawbacks of the first and second generations of AHSSs provide an opportunity for researchers and steel manufacturers to develop the third generation of AHSSs. This generation is expected to fill

the gaps and solve the drawbacks of the last two generations. AHSS should increase to 15% (250 kg) of the total vehicle weight by 2020 [3]. Therefore, third generation serves as a good candidate for extensive study and development. Bainitic steels with second phase constituents (*i.e.* Martensite and Retained austenite) are an example of third generation steels.

## 1.2 The importance of failure mechanisms on BIW formability prediction

Sheet Metal Forming (SMF) in automotive applications is an important requirement for material suppliers. Many experiments and simulations are performed in order to predict the forming limits of steel sheets, which are determined either by the sheets' failure or deformation localization during various forming processes.

In order to predict the strain path of the material during different forming processes and estimate the limits of safe deformation, **Forming Limit Diagrams** (FLDs) are commonly used. These diagrams were initially introduced by Keeler *et al.* [5], and they detect the safe regions of formability for various strain paths by analyzing maximum and minimum principal strains. The FLDs rely on strain localization and fracture as two criteria of failure. When it comes to strain localization as a failure criterion, **Forming Limit Curves** (FLCs) are used. These curves identify the point of necking during different strain paths. For instance, mild and conventional high-strength steels reveal localized necking as their failure mode prior to fracture. However, AHSSs may fail through sudden failure with or without limited localization, while their fracture surface exhibits typical dimple topology associated with ductile fracture. Many researchers have proposed **Fracture Limit Curves** (FrLCs) as an alternative solution to separate necking and fracture as two failure criteria to detect the safe forming limits of such steels [6-9]. The power of these curves relies on macroscopic assessment of the safe forming capacity of materials, with no attention paid to underlying damage micro-mechanisms involved at the microstructure level during plastic deformation.

In order to enhance the formability at the macroscopic level, a deep understanding over micro-mechanisms of failure and damage initiation is necessary. There is a series of phenomena at the microscopic level during the ductile failure process, such as void initiation, growth and coalescence, which eventually leads to macroscopic failure [10].

In the complex microstructure of the AHSSs, the initiation and evolution of damage is governed by two different types of microstructural features: *(i)* phase boundaries and *(ii)* polycrystalline aggregate of the metals matrix. Depending on the microstructure and its heterogeneous nature, the involved micro-mechanisms change. The role of inclusions in the **Interstitial Free (IF)** and the martensite phase in DP steels is an example of phase heterogeneity that has been studied [11].

Understanding complicated multiphase microstructures and their role in damage initiation is crucial and challenging in order to improve the macroscopic mechanical response and formability for the automotive application. Many researchers have addressed this challenge via computation modelling and experiments. However, there are still aspects which need further study by both advanced experimental and modelling techniques.

### 1.3 Thesis objective and outline

The aim of this thesis is to address the micro-mechanisms of damage initiation in bainitic multiphase steels under the static loading conditions. This study reveals if there is any hierarchical correlation between damage and forming behavior. In order to achieve this goal, advanced experimental characterization techniques and Crystal Plasticity (CP) based model are used. In order to understand the mechanical response of bainitic multiphase steels under high strain rate deformations (*i.e.* crash events and some forming processes), dynamic mechanical tests are carried out. Eventually, this thesis is structured in eight chapters, as follows:

In **Chapter 2**, a comprehensive literature review is presented. First, an introduction to bainitic multiphase steels is given in order to understand their microstructural features and mechanical properties. Second, the importance of high strain rate deformations is demonstrated. Third, ductile damage mechanisms involved at various length scales from nano to macro are discussed. More specifically, the role of second-phase microstructural constituents and their topological effect (size, shape and distribution) on the evolution of stress/strain incompatibilities/partitioning during the plastic deformation is illustrated. Fourth and final, the impact of anisotropic plastic response of the polycrystalline medium in damage initiation is illustrated.

In **Chapter 3**, the overall experimental techniques and modelling methods employed in this thesis are introduced. Special attention is payed to illustrate the general setup and procedure of dynamic mechanical tests carried out by the Split Hopkinson Tensile Bar (SHTB). Besides, the crystal orientation mapping conducted by the Electron Backscatter Diffraction (EBSD) technique is introduced.

Additionally, the phenomenological hardening model of Johnson-Cook is introduced. The Visco-Plastic Self-Consistent (VPSC) model is combined with a physical hardening model in order to simulate the anisotropy of the mechanical response under quasi-static and dynamic loading conditions. Eventually, the VPSC model is used to predict damage initiation sites based on stress/strain partitioning among the simulated grains.

In **Chapter 4**, the microstructural characteristics of the developed bainitic multiphase steels are quantified. The static and dynamic mechanical response profiles are analyzed. Later, the role of microstructural variables on static and dynamic mechanical properties is discussed. In addition, the strain rate sensitivity of various steel grades and its correlation to microstructural variables and the strength of the steels are investigated.

In **Chapter 5**, damage initiation micro-mechanisms under static loading conditions are addressed. The effect of micro and meso-scale heterogeneities on the local damage nucleation activity and global failure of the bainitic multiphase steels are studied.

**Chapter 6** introduces a new post-mortem texture-based approach to study the correlation between crystallographic orientation and damage initiation sites. These results of this analysis will be compared with the results derived from the crystal plasticity model in order to validate the predicted potential damage initiation sites based on stress/strain partitioning. In addition, this method can further explain whether void growth or local plasticity is more dominant in dissipation of plastic work after the initiation of voids.

Among different crystal plasticity models, in **Chapter 7**, the visco-plastic self-consistent crystal plasticity model is combined with a physical hardening law in order to simulate the anisotropy of global mechanical response under the quasi-static and dynamic loading conditions. Moreover, susceptible damage initiation sites based on the maximum stress/strain incompatibilities are predicted and validated with the results derived in chapter 6.

Finally, the general conclusions of the thesis are listed in **Chapter 8**.

## References

- [1] A. Morita, Aluminium alloys for automobile applications, Proc. of ICAA-6 vol. 1(1998) (1998) 25–32.
- [2] J.R. Fekete, Current challenges in implementing Advanced High Strength Steels, International Conference on Microalloyed Steels: Processing, Microstructure, Properties and Performance (2007) pp. 1-9.
- [3] J.G.S. David K. Matlock, Emmanuel De Moor, and Paul J. Gibbs, Recent developments in advanced high strength sheet steels for automotive applications: An overview, JESTECH 15(1) (2012) 1-12.
- [4] L.C. B. C. De Cooman, H. S. Kim, Y. Estrin, S. K. Kim and H. Voswinckel, State-of-the-Science of High Manganese TWIP Steels for Automotive Applications, Microstructure and Texture in Steels and Other Materials, Springer (2009) 165-183.
- [5] S.P.K.a.W.A. Backhofen, Plastic Instability and Fracture in Sheet Stretched over Rigid Punches,, ASM Transactions Quarterly Vol. 56(No. 11) (1963) 25-48.
- [6] R.J. Bourcier, D.A. Koss, A Fracture Limit Diagram for Determining Hydrogen Embrittlement of Sheet under Multiaxial Loading Conditions, Scripta Metallurgica 16(5) (1982) 515-518.
- [7] A.K. Ghosh, Criterion for Ductile Fracture in Sheets under Biaxial Loading, Metall Trans A 7(4) (1976) 523-533.
- [8] M. Jain, J. Allin, D.J. Lloyd, Fracture limit prediction using ductile fracture criteria for forming of an automotive aluminum sheet, International Journal of Mechanical Sciences 41(10) (1999) 1273-1288.
- [9] H. Takuda, K. Mori, N. Takakura, K. Yamaguchi, Finite element analysis of limit strains in biaxial stretching of sheet metals allowing for ductile fracture, International Journal of Mechanical Sciences 42(4) (2000) 785-798.
- [10] J. Lin, Y. Liu, T.A. Dean, A review on damage mechanisms, models and calibration methods under various deformation conditions, International Journal of Damage Mechanics 14(4) (2005) 299-319.
- [11] O. Leon-Garcia, Micromechanisms of Failure under Static Loading in Sheet Metals for Automotive Applications, Technische Univeriteit Delft, Delft, 2013.

# **Chapter 2 Literature review: Strain rate dependence of mechanical properties and ductile failure micro-mechanisms**

**Abstract.** This chapter provides a general overview of the required knowledge in order to understand and further study the content covered in this thesis. In the beginning, in section 2.1, a brief introduction to bainitic steels with regard to their mechanical properties and microstructural characteristics is presented. In section 2.2, first the necessity and importance of high strain rate deformations in different applications is explained. In addition, a comprehensive literature survey of various steel grades tested under dynamic loading conditions is presented. Besides, the correlation between microstructure and strain rate hardening/softening is addressed. Moreover, ductile failure mechanisms involved at various length scales are introduced in section 2.3. In particular, the individual role of micro-mechanical heterogeneities and their corresponding topology in damage initiation micro-mechanisms is further explained in subsection 2.3.1. Eventually, the impact of crystallographic orientation on deformation anisotropy and damage initiation is illustrated in subsection 2.3.2.

## **2.1 Introduction**

Bainitic complex phase steels, as third generation Advanced High Strength Steels (AHSSs), are promising candidates for automotive applications due to their low manufacturing cost and enhanced mechanical properties [1, 2]. Their satisfactory high strength (tensile strength ranging from 1300 to 1800 MPa) caused by the presence of the bainitic matrix (or lath like ferritic matrix) and martensite phase as a second phase constituent, often combined with enhanced ductility through the stabilization of austenite phase at room temperature (total elongation over 14%), result in an optimum combination of strength, ductility and formability [3-8]. Bainitic multiphase steels with higher microstructural

homogeneity in terms of phase contrast demonstrate improved stretch flangeability (quantified normally by the hole expansion test) compared to the first generation of AHSSs such as low alloy TRIP and DP steels [9, 10]. Carbide free bainitic multiphase steels with lath-like bainitic matrix are designed to achieve very good stretch-flangeability due to less phase contrast between bainite and martensite compared to polygonal ferrite [3]. In addition, it has been reported by Nagasaka *et al.* that the presence of martensite phase as a hard constituent does not lead to deterioration of the deep drawability in this bainitic steels [11]. Figure 2-1 demonstrates a carbide free bainitic matrix with martensite and retained austenite as second phase constituents. Lath shape bainitic ferrite is revealed using Transmission Electron Microscopy (TEM) (cf. fig.2-1b).

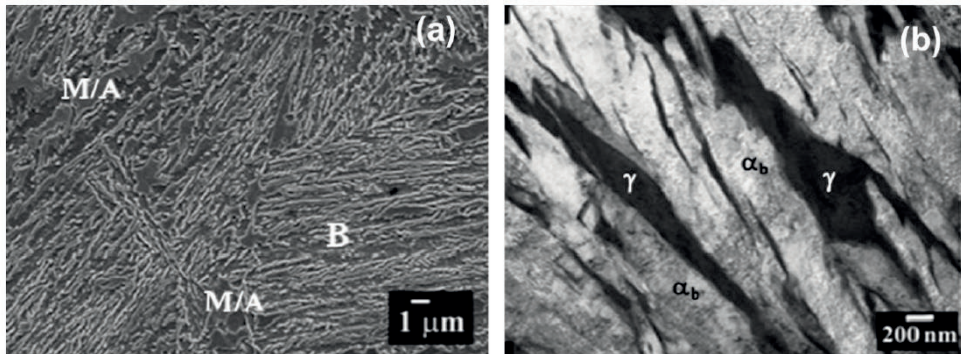


Figure 2-1 Microstructure of a bainitic steel with bainite (B), martensite (M) and retained austenite (A);(a) Scanning and (b) Transmission electron micrographs.  $\alpha_b$  is the bainitic ferrite,  $\gamma$  is the thin film of A and M/A shows the martensite and austenite islands [3].

Developing and employing bainitic steels with improved mechanical properties allows to lowering the Body-In-White (BIW) weight, which leads to energy saving and pollution reduction. Therefore, understanding the effect of microstructure on mechanical response of the material and micro-mechanical behavior of microstructure is crucial in order to design a bainitic steel with enhanced mechanical properties.

## 2.2 Strain rate dependence of mechanical properties

The dynamic mechanical response of steels is significant for steel manufacturers from two different perspectives. First, dynamic behavior is important to assess the crashworthiness characteristics, which are assessed by the energy absorption of the car body panel during a crash event. It is reported that during such an event, strain rates reach up to  $10^2 \text{ s}^{-1}$  and  $10^3 \text{ s}^{-1}$  at hinge points and folds, respectively [12]. For instance, Ultra-Light Auto Steel Body - Advanced Vehicle Concept (ULAS-AVC) assigns requirements for design and also evaluates the performance of car bodies during crash events. In Figure 2-2 shown by ULAS-AVC, it is illustrated that the dash crash box structure is designed firstly to absorb impact energy in full frontal and 40% offset crash events. Employing AHSSs in this structure ensure that crash loads are widely distributed through the vehicle at reduced mass [13]. Second, some forming processes such as magnetic pulse forming, hydroforming and explosive forming, involve very high strain rates and thus it is of crucial importance to control material response to dynamic loading [14].

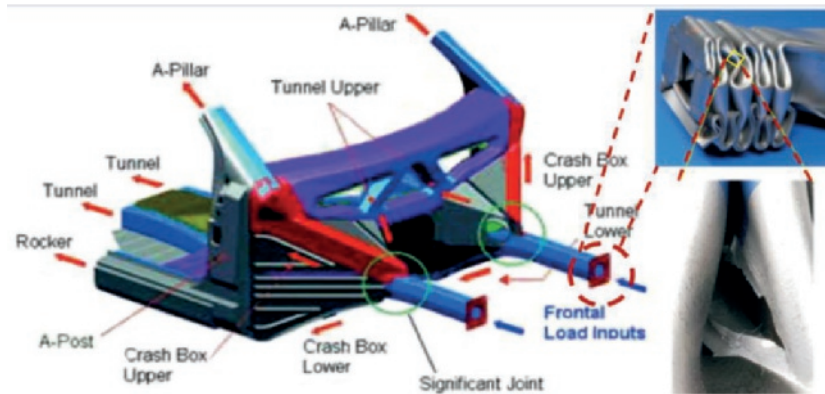


Figure 2-2 Dash crash box structure [13, 15].

Two simultaneous processes are normally involved during high strain rate deformations, which affect the mechanical response of materials. First, strain hardening due to the plastic deformation. Second, thermal softening due to the adiabatic temperature rise. As a result of the dependency of ductility, plastic flow stresses, and thus energy absorption and formability to the strain rate, many researchers have studied the high strain rate mechanical response of various steel grades of the first generation of AHSSs.

Verleysen *et al.* [16] have studied the forming behavior of sheet metals under high strain rates. They have predicted the Forming Limit Diagrams (FLD) of the structural steel S235, the drawing steel DC04, the ferritic stainless steel AISI409 and the CMnAl Transformation Induced Plasticity (TRIP) steels

based on a uni-axial high strain rate test and using the Marciniak-Kuczynski (M-K) method. Their FLD curves, shown in figure 2-3, reveal an enhanced forming limit behavior for the TRIP steel (upward shift) while for the other steels the reduced ductility under uniaxial loading leads to lower forming limit capacity (downward shift) under dynamic loading conditions compared to their corresponding static FLDs.

Moreover, the correlation between microstructure and properties has always been an important and vital subject to study. This is due to the fact that the overall mechanical response of materials is governed primarily by their microstructures. Various multiphase steels with retained austenite (RA) as a second phase constituents have been studied under high strain rate deformations. The TRIP effect retardation mechanisms involved during the dynamic loading condition have been investigated by different researchers.

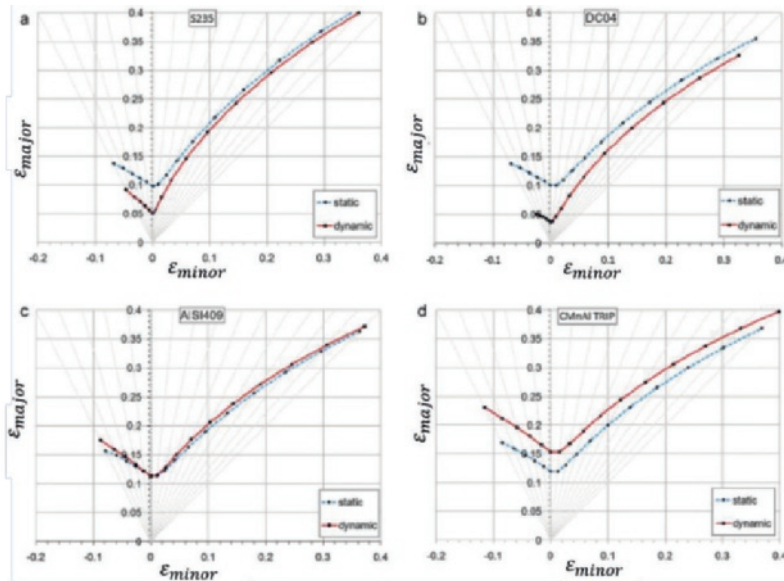


Figure 2-3 Comparison of static and dynamic FLD's for S235, DC04, AISI409 and CMnAl TRIP [16]. The region under the V-curve is considered as a safe region.

Van Slycken *et al.* [17] have studied the general dynamic mechanical response of a multi-phase TRIP, ferritic and austenitic steels. They have observed a delay of the TRIP effect because of adiabatic

temperature rise at high strain rates. Thermodynamically, this phenomenon was initially investigated by Olsen *et al.* in 1972 [18]. Controlled by the austenite and martensite free Gibbs energy as a function of temperature, depicted in figure 2-4(a) [19, 20],  $M_s$  is the start temperature of thermal martensite transformation. At this temperature, the martensite transformation is initiated at pre-existing nucleation sites during cooling, driven by the difference in chemical free energy  $\Delta G_{M_s}^{\gamma \rightarrow \alpha'}$  of the two phases. Besides, at  $T_0$  temperature both phases have identical free energy and are in stable equilibrium ( $G_\gamma = G_\alpha$ ). Nevertheless, below  $T_0$  but above  $M_s^\sigma$  martensite does not transform spontaneously due to the insufficient driving force ( $\Delta G_{T_1}^{\gamma \rightarrow \alpha'}$ ) and it requires additional mechanical energy ( $U'$ ). Therefore, if this mechanical energy is added to  $\Delta G_{T_1}^{\gamma \rightarrow \alpha'}$ , then it becomes equal to  $\Delta G_{M_s}^{\gamma \rightarrow \alpha'}$  (i.e.  $\Delta G_{T_1}^{\gamma \rightarrow \alpha'} + U' = \Delta G_{M_s}^{\gamma \rightarrow \alpha'}$ ) assuming that the critical driving force needed for the martensite transformation remains constant over the temperature range of interest [21]. As shown in figure 2-4(a), the chemical driving force  $\Delta G_T^{\gamma \rightarrow \alpha'}$  for the martensite transformation decreases by increasing temperature and thus the required mechanical energy  $U'$  for the transformation increases. Bolling *et al.* [22] have demonstrated that at temperature above  $M_s^\sigma$ , the stress needed to trigger martensite transformation exceeds the yield stress of the parent austenite phase, and the transformation can only occur after a specific amount of plastic deformation in the austenite phase. Therefore, the temperature region of  $M_s^\sigma < T < M_d$  is usually referred to as the strain-assisted transformation regime, while  $M_s < T < M_s^\sigma$  is nominated as the stress-induced transformation regime. Figure 2-4(b) depicts the schematic illustration of stress required for the initiation of martensite transformation at different temperatures.

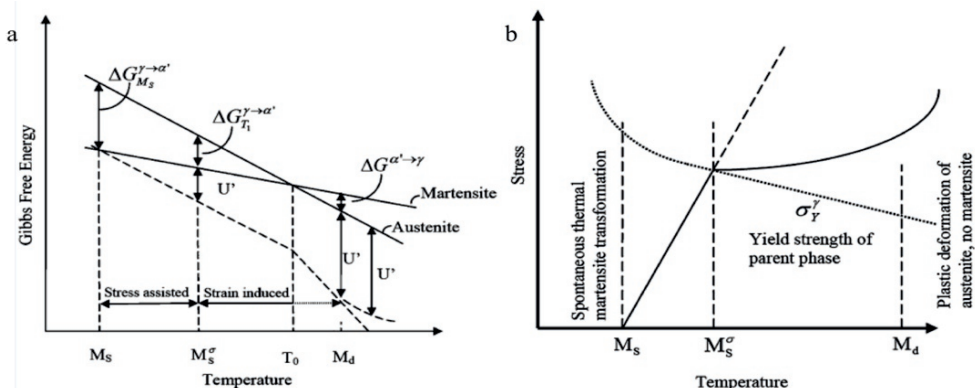


Figure 2-4 Schematic illustration of critical stress for the initiation of martensite transformation as a function of temperature [18-20].

Nevertheless, Choi *et al.* [23] have reported in their study on a duplex stainless steel that the different strength of individual phases of ferrite and austenite affect the retardation of strain-induced martensitic transformation due not only to the adiabatic temperature rise during high strain rates but also to strain partitioning, which becomes more pronounced by increasing strain rates. Eventually, this would affect the tensile properties under dynamic loading of multiphase steels with austenite phase as a micro-constituent. In addition, the retardation of the TRIP effect was also observed by Wei *et al.* [24]. They have shown that increasing the strain under both static and dynamic loading conditions results in a higher percentage of TRIP effect. In a fundamental investigation using nano-indentation conducted by Li *et al.* [25] on Al containing TRIP steels, it was reported that the competitive deformation mechanisms of TRIP and Twinning Induced Plasticity (TWIP) in the RA phase is governed by three energy terms: (i) the Stacking Fault Energy (SFE), (ii) the austenite to martensite transformation Gibbs energy and (iii) the strain energy, which is dependent of strain rate. Consequently, the interplay between TRIP and TWIP would affect the strain rate sensitivity. Besides, in a study conducted by Tsai *et al.* [26], on the deformation mode of the RA under high strain rate in a nanostructured bainitic steel, it was shown that twinning was the dominant carrier of plastic strain in blocky RA rather than martensite formation. In addition, it was concluded that not only the strain rate but also the strain mode affects the deformation mode of RA.

In the case of ferritic-martensitic Dual Phase (DP) steels, Wang *et al.* [27] have reported the effect of martensite volume fraction on the mechanical response under high strain rate deformations. They have shown that the higher the martensite volume fraction, the lower is the strain rate hardening, while fully martensitic steel demonstrates even strain rate softening. Conversely, the ferrite phase plays a dominant role on the strain rate hardening and work hardening effect. Similar effects have been reported by Yu *et al.* and Oliver *et al.* in DP 600 and DP 1400 steels [28, 29]. In a recent study, Rahmaan *et al.* [30] have observed an isotropic behavior of strain rate sensitivity in DP600, TRIP 780 and AA5182-O by performing dynamic tests in three different orientations with respect to the sheet rolling direction (RD).

### 2.3 Ductile failure mechanisms

Ductile failure in metals is a consequence of a sequence of events taking place at various length scales starting from nano, micro and eventually to macro-scale. At these scales, the characteristics of the involved mechanisms are different, although they are correlated. Figure 2-5 illustrates various length scales with regard to ductile failure during a high strain rate deformation at  $687\text{ s}^{-1}$ .

An overall overview on ductile damage mechanisms is well summarised by León-García [31]. It is well known that the nano-mechanisms leading to failure are mainly related to the formation and interaction of dislocations with defects (i.e. phase interfaces and grain boundaries), which can result in dislocation pile-ups. Therefore, at certain moment, when a critical stress is reached, dislocation coalescence causes the formation of cavities as proposed by Zener [32]. In other words, the separation of atomic bonds results in *formation of voids* during plastic deformation. Normally, brittle particles or weak atomic bonds, for instance between dissimilar atoms or regions where crystal lattice is more distorted, are more susceptible to the separation. The separation can be further facilitated by stress concentration triggered from dislocation pile-ups. Following the initiation of voids, the void growth process starts by of further separation of atomic bonds which is governed by complicated interaction between dislocations and voids [33, 34].

Changing the length scale from nano to micro and meso scale unravels different aspects of ductile damage initiation mechanisms. At this length scale, microstructural heterogeneities such as second phase constituents (intermetallic particles and/or precipitates, and hard phases) play a significant role in introducing stress/strain incompatibilities within a microstructure. The interfaces of these constituents with the surrounding matrix are ready sites to void formation due to different micro-mechanical response of these phases, polycrystalline matrix (soft) and second phase constituents (hard), to the macroscopically imposed deformation. Figure 2-5(d) demonstrates a bainitic matrix loaded under dynamic loading conditions, where micro-voids at the interface of bainite (soft phase) and martensite (hard phase) are observed. However, in the case of single phase polycrystalline metals, voids are initiated at grain boundaries as a result of anisotropy of plasticity among grains according to their corresponding crystallographic orientations [35]. The *Void growth* is governed by the stress/strain states in the matrix around the initiated voids. After the initiation of voids, the plastic work can be dissipated by void growth and further plasticity which results in local hardening. The competition between these two mechanisms decides the rate of void growth during plastic deformation. Subsequent to void growth, the *void coalescence* event occurs as a consequence of the deformation path in the matrix controlled by local microstructural features (i.e. crystallographic orientation, distribution of hard phase and voids). Consequently, the coalescence event leads to the formation of cracks as depicted in figure 2-5(c and d). This event denotes the beginning of the fracture process.

Macro-cracks within the microstructure may have two different characters with regard to growth rate: stable and unstable. This character is determined by their propagation speed and stress/strain states related to the structure geometry and loading conditions. The propagation of macro-cracks is initially stable. Due to the stress concentration at the crack tip, thus, deformation is confined to this region,

which is denominated as the Fracture Process Zone (FPZ). Crack propagation is further continued within this zone [31]. Nevertheless, the interaction between the crack and the state of strain/stress reaches a critical point, in which it propagates in a fast and unstable manner, and therefore the global failure of the structure is observed (cf. Figure 2-5).

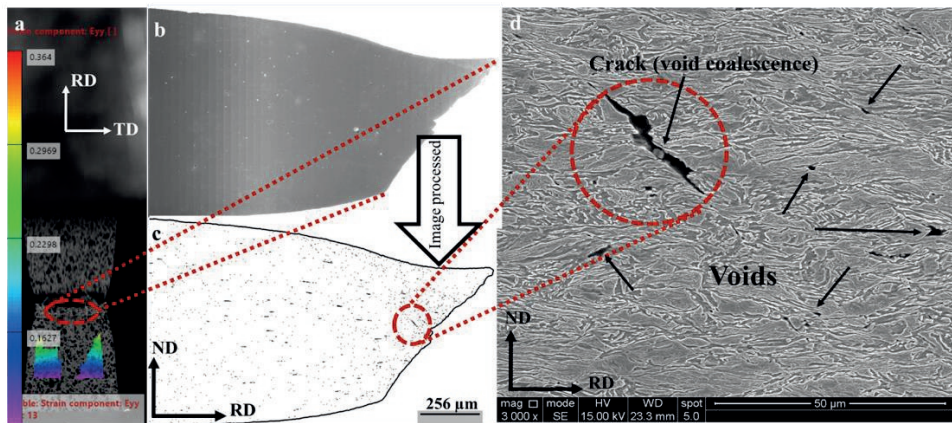


Figure 2-5. An example of damage mechanisms at different length scales which lead to global failure: (a) a high strain rate ( $687 \text{ s}^{-1}$ ) tensile deformation of a bainitic steel loaded along Rolling Direction (RD), (b) contiguous collection of  $\sim 1000$  SEM micrographs of the fracture sample in (a), (c) the corresponding image processed version of (b) with clear distribution of voids and (d) etched microstructure of the fractured bainitic multiphase steel introduced in chapter 3.

Generally, damage initiation micro-mechanisms in multiphase metals can be classified into two parts. First, the effect of phase contrast and its topology (size, shape and distribution). Second, the role of crystallographic orientation, which is inevitable in a polycrystalline medium. In section 2.3.1, a comprehensive literature survey with an emphasize on the role of phase contrast and topology in damage initiation micro-mechanisms in multiphase steels are illustrated. Moreover, in section 2.3.2, another aspect involved in damage initiation, which is related to crystallographic orientation and the anisotropy of plastic deformation, is explained.

### 2.3.1 Phase contrast and topology

It has been well established that micro-mechanical heterogeneities on stress/strain partitioning have a significant effect on the damage initiation and the dominant void formation mechanisms involved in ductile failure. Tasan and Yan *et al.* [36-39] have studied the topological aspect of damage initiation

micro-mechanisms by advanced experimental techniques integrated with crystal plasticity (CP) models in ferritic and martensitic dual-phase (DP) steels. It was shown that the strain partitioning between ferrite and martensite during uniaxial tensile loading is highly affected by the topology (size, shape and distribution) of the martensite. Yan *et al.* have coupled various probe-analysis techniques such as scanning electron microscopy imaging methods (i.e. electron backscatter diffraction, electron channel contrast imaging) and microscopic-digital image correlation ( $\mu$ -DIC) to overcome different challenges corresponding to simultaneous mapping of micro-strains within a DP microstructure during the macroscopically imposed deformation. They have shown that damage nucleation in DP steel is in most cases not strain controlled but rather stress-controlled process, and it is strongly dependent on martensite morphology and percolation [39].

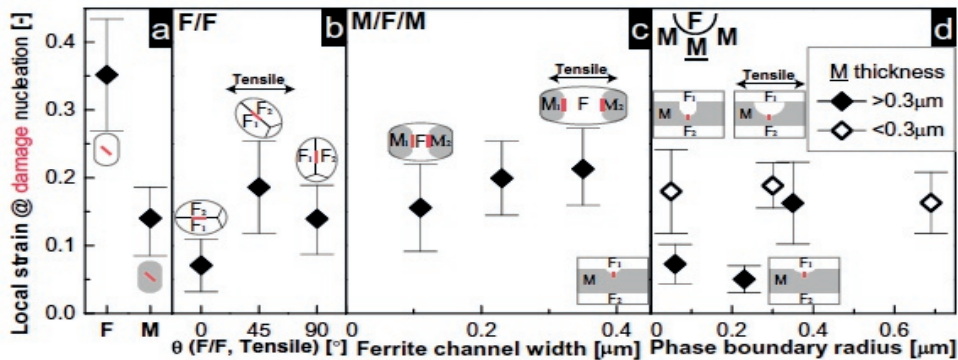


Figure 2-6 Local critical strain for damage nucleation in a DP steel corresponding to different damage mechanisms with respect to: (a) damage inside ferrite grains F or inside martensite islands M; (b) average angle  $\theta$  between ferrite grain boundary segment and tensile direction ( $\pm 5^\circ$ ) for ferrite grain boundary F/F damage; (c) ferrite channel width for martensite/ferrite phase boundary M/F damage; and (d) phase boundary radius at different bridging martensite M thickness for M/F damage. Corresponding microstructures are shown topologically [39].

Figure 2-6(a) and (b-d) show the local critical strain for damage nucleation at the bulk and interface-dominated damage mechanisms. It is important to note that this graph is based on the comparison made at similar global strain. In addition, damage incidents with similar neighboring ( $\sim 4 \mu\text{m}$  distance) microstructure and strain fields are selected. In case of bulk related damages, it is shown that the critical strain needed for the ferrite (damage inside ferrite grains) is higher than that of martensite. Despite, the high difference between bulk related damage mechanisms F and M, the difference between the critical strain of all interface-dominated damage mechanisms is small as depicted in figure 2-6(b-d). However, the critical strain trends observed in figure 2-6 individually for F/F (fig. 2-6b), M/F/M (fig. 2-6c) and notched-M (fig. 2-6d) reveal that the interface-dominated damage mechanisms are strongly controlled

by the local microstructure morphology and phase percolation. Beside the effect of martensite morphology on damage nucleation activity, in another study conducted by Tasan *et al.* [37], the particular role of martensite dispersion and ferrite grain size on strain distribution was investigated. They have demonstrated that, when the microstructure becomes finer and the martensite content increases, strain partitioning behavior reveals remarkable changes. In general, coarse ferritic regions still accommodate significant amounts of strain. However, based on the distribution and fraction of martensite, the heterogeneity of plastic strain accommodation changes. They have shown that the homogeneous dispersion of fine martensite phase throughout the ferritic matrix allows more of the ferritic regions to engage in accommodating the plastic deformation. In contrary, when the martensite fraction is lower but the existing martensite islands are large and blocky, these martensite regions undergo higher stress, and thus the strain is more dominantly accommodated in only certain ferritic grains that lay in locations of highest shear. Therefore, they have concluded that the latter type of microstructures experience earlier macroscopic deformation localization and thus failure takes place at much lower global strain levels compared to the microstructures with finer dispersion of martensite. Although they have observed that homogeneous dispersion of fine martensite resulted in a higher damage nucleation activity, this type of microstructure fails at higher levels of strain through arresting micro-voids by local hardening of the ferritic matrix.

Ahmad and Lai *et al.* showed that the martensite volume fraction plays an important role in transition of the dominant damage mechanism by either martensite tearing, at high martensite fraction to interface decohesion at decreased martensite fraction [40, 41].

Recently, Archie *et al.* [42], investigated the role of interfaces (*i.e* phase, prior austenite grain (PAG) and grain boundaries) and their chemistry on micro-mechanisms of void initiation. It was shown that at low strain levels, most of the damage sites initiated by martensite tearing where located at PAGBs (cf. fig. 2-7a). However, this mechanism becomes less prominent at higher strain levels, and instead, it was shown that deformation bands and ferrite grain boundaries adjacent to ferrite/martensite interfaces are the susceptible damage initiation sites.

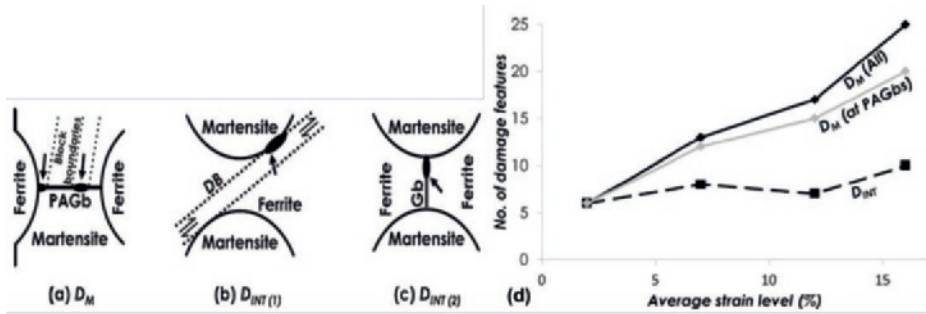


Figure 2-7 Damage micro-mechanisms in the DP steel: (a, b and c) schematic illustration of the involved damage micro-mechanisms with different microstructural configurations and (d) quantitative analysis of individual features corresponding to each damage mechanisms at each average global strain level [42].

Moreover, Archie *et al.* showed that nano-chemical segregation of Mn resulted in interface weakening at PAGBs using Atom Probe Tomography (APT). Referring to [43–46], the local enrichment of Mn might be directly responsible for the low grain boundary cohesion, either due to vacancy-Mn pair formation [43], or by grain boundary relaxation [46]. However, it is also well known that C and B are considered as grain boundary strengtheners [47, 48]. Figure 2-8 depicts the APT result with regard to the segregation of Mn at a PAGB.

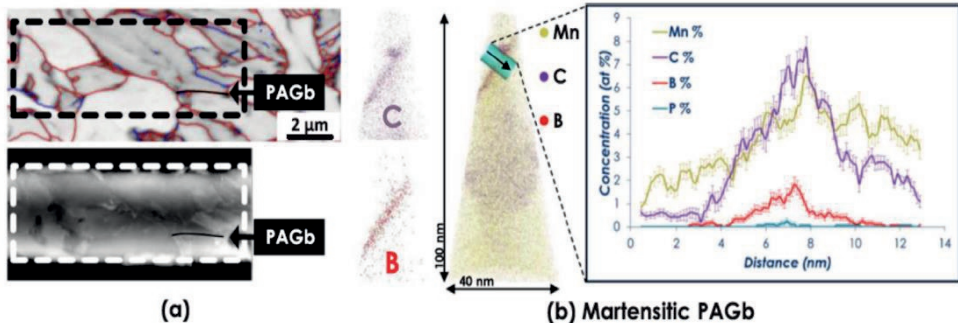


Figure 2-8 Nano-chemical analysis at a PAGB: (a) an example of EBSD image quality map and corresponding APT lift-out (SE image) of a PAGB-bearing martensite island and (b) illustrates the corresponding reconstructed APT data set [42].

### 2.3.2 Crystallographic orientation

In the previous section, the role of phase contrast and topology on damage initiation micro-mechanisms involved in ductile failure has been addressed. Nevertheless, in the case of polycrystalline materials, the role of crystallographic orientation on stress and strain partitioning is crucial. This has been studied for single phase polycrystalline materials by Asaro *et al.* [49], where they have demonstrated the effect strain rate sensitivity and strain hardening rate of slip systems on failure strain and localized necking. However, in the multi-phase polycrystalline material, the competitive role of mechanical phase contrast and crystallographic orientation on stress/strain partitioning is an area of discussion. In a systematic study by de Geus *et al.* [50], it is demonstrated that the effect of the second phase constituents over grain's orientation anisotropy on strain partitioning increases by higher mechanical contrast between two phases. However, this effect has been studied by some idealized assumptions in a crystal plasticity framework on a randomly oriented virtual microstructure.

In the results reported by Tasan *et al.* [37], based on their analysis on grains Taylor factor, they have shown that the influence of grain size on strain partitioning is more dominant than the crystallographic orientation of grains. However, in other studies carried out by in situ neutron diffraction combined with self-consistent (SC) models on a duplex stainless steel (DSS) [51, 52], they have studied the stress-strain evolution between constituent phases and grains with different crystallographic orientations. In the later work [52], it was shown that at higher macroscopic stresses, when all grains in both constituent phases deform plastically, the role of grain's anisotropy on stress-strain partitioning is more significant than the phase contrast stresses. Moreover, the role of crystallographic orientation on damage initiation at relatively higher level of plastic deformations was also reported by Needleman *et al.* and Nugent *et al.* on metal-matrix and rigid fiber composites, respectively [53, 54].

Employing a micro-tensile specimen, Kwak *et al.* [55] have shown, for a dual phase bainitic-martensitic steel, that strain concentrates in bainitic grains oriented favorably for in-habit-plane slip, thus, this has given rise to low-ductility fracture. In addition, they performed Crystal Plasticity Finite Element Method (CPFEM) simulations with and without considering the habit-plane-orientation-dependent yielding. In their simulations, the microstructure is generated through complete characterization of micro-tensile specimen by EBSD technique. Therefore, the distribution of hard and soft phases and their corresponding crystallographic orientations are taken into account in their finite element mesh. Figure 2-9 demonstrates the condition of habit-plane-orientation-dependent yielding and the corresponding in-situ optical microscopy of the micro-tensile specimen during deformation at different

strain levels. The white lines show interphase boundaries between bainitic matrix and the martensite phase, while black lines are high angle grain boundaries. By comparing the fracture process (cf. fig. 2-9a, b and c) and the associated CPFEM simulation, it is observed that more strain is accommodated by bainitic regions at the vicinity of bainite and martensite boundaries. In addition, the stress is concentrated at the interface between bainite and martensite (cf. fig. 2-9g, h and i). Overall, it is clear that the simulation can predict the damage process. However, in figure 2-10 where simulation is conducted without considering the habit-plane-orientation-dependent yielding, the stress-strain partitioning is not clearly observed between bainite and martensite. Moreover, the overall failure process is not predicted well by comparing the fracture process shown in figure 2-9(a, b and c).

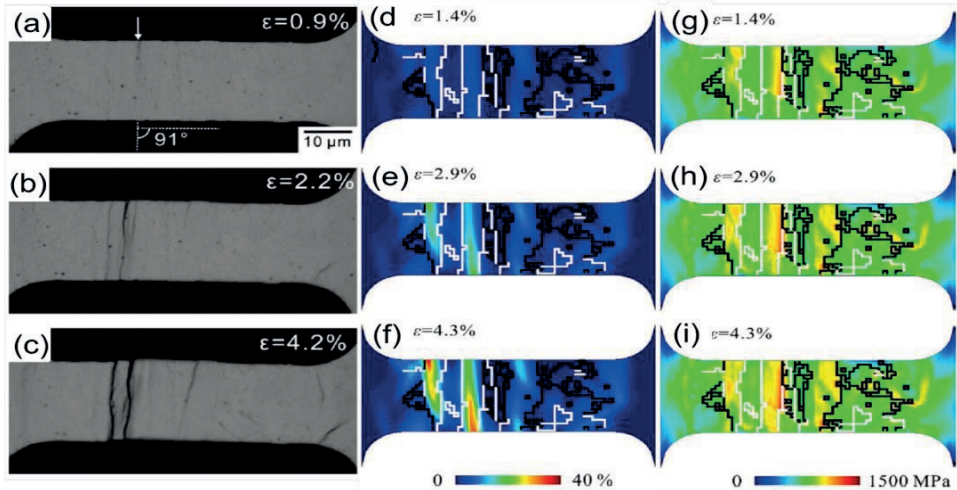


Figure 2-9 In-situ deformation of a micro-tensile specimen: (a, b and c) are the optical microscopy of the specimen at different strain levels, (d, e and f) distribution of equivalent strain and (g, h and i) distribution of equivalent stress analysed with consideration of the habit-plane-dependent yielding [55]. The distribution of equivalent stress and strains is derived from the CPFEM simulation.

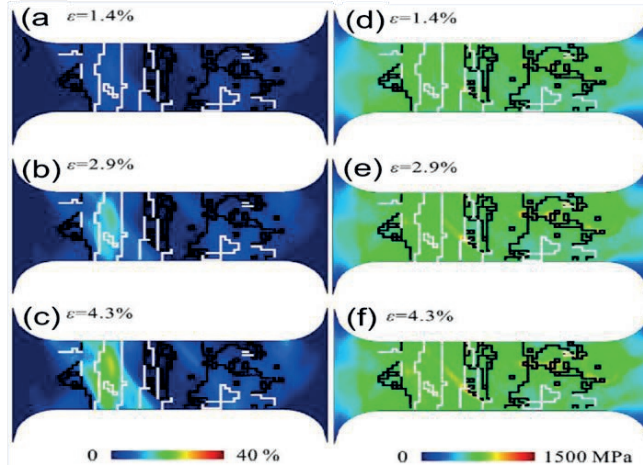


Figure 2-10 CPFEM simulation of a micro-tensile specimen during the tensile deformation: (a, b and c) distribution of equivalent strain and (d, e and f) distribution of equivalent stress analysed without consideration of the habit-plane-dependent yielding [55].

## References

[1] J.G.S. David K. Matlock, Emmanuel De Moor, and Paul J. Gibbs, Recent developments in Advanced High Strength Sheet Steels for automotive applications-An Overview, JESTECH 15(1) (2012) 1-12.

[2] R. Kuziak, R. Kawalla, S. Waengler, Advanced high strength steels for automotive industry: a review, Arch Civ Mech Eng 8(2) (2008) 103-117.

[3] F.G. Caballero, S. Allain, J. Cornide, J.D. Puerta Velásquez, C. García-Mateo, M.K. Miller, Design of cold rolled and continuous annealed carbide-free bainitic steels for automotive application, Mater Design 49 (2013) 667-680.

[4] F.G. Caballero, H.K.D.H. Bhadeshia, Design of novel high-strength bainitic steels, Thermec, Mater Sci Forum 2003, pp. 1337-1342.

[5] F.G. Caballero, H.K.D.H. Bhadeshia, K.J.A. Mawella, D.G. Jones, P. Brown, Design of novel high strength bainitic steels: Part 1, Mater Sci Tech-Lond 17(5) (2001) 512-516.

[6] F.G. Caballero, H.K.D.H. Bhadeshia, K.J.A. Mawella, D.G. Jones, P. Brown, Design of novel high strength bainitic steels: Part 2, Mater Sci Tech-Lond 17(5) (2001) 517-522.

[7] F.G. Caballero, C. García-Mateo, J. Chao, M.J. Santofimia, C. Capdevila, C.G. de Andres, Effects of morphology and stability of retained austenite on the ductility of TRIP-aided bainitic steels, Isij Int 48(9) (2008) 1256-1262.

[8] Y. Wang, K. Zhang, Z. Guo, N. Chen, Y. Rong, A new effect of retained austenite on ductility enhancement in high strength bainitic steel, Mat Sci Eng a-Struct 552 (2012) 288-294.

[9] M. Mizui, H. Takechi, T. Sekine, Effects of Strengthening Mechanisms on Fatigue Damage for 600 Mpa Class Hot-Rolled High-Strength Sheet Steels, Tetsu to Hagane-Journal of the Iron and Steel Institute of Japan 76(3) (1990) 414-421.

[10] T. M, Material characterization at high strain rates for optimizing car body structures for crash events, Nippon Steel, 2003, pp. 22-6.

[11] A. Nagasaka, K. Sugimoto, M. Kobayashi, S. Hashimoto, Effects of warm forming on stretch-flangeability of a TRIP-aided dual-phase sheet steel, Tetsu to Hagane-Journal of the Iron and Steel Institute of Japan 83(5) (1997) 335-340.

[12] C.P. Salisbury, M.J. Worswick, R. Mayer, High rate constitutive modeling of aluminium alloy tube, J Phys IV 134 (2006) 43-48.

[13] Official site of the european new car assessment programme. (<https://www.autosteel.org/programs/ulsab-avc>) (2018).

[14] D.A. Oliveira, M.J. Worswick, M. Finn, D. Newman, Electromagnetic forming of aluminum alloy sheet: Free-form and cavity fill experiments and model, Materials Processing Technology 170(1) (2005) 350-362.

[15] C.C. Tasan, Micro-mechanical Characterization of Ductile Damage in Sheet Metal, TU Eindhoven, Universiteitsdrukkerij TU Eindhoven, 2010.

[16] P. Verleysen, J. Peirs, J. Van Slycken, K. Faes, L. Duchene, Effect of strain rate on the forming behaviour of sheet metals, Materials Processing Technology 211(8) (2011) 1457-1464.

[17] J. Van Slycken, P. Verleysen, J. Degrieck, J. Bouquerel, B.C. De Cooman, Dynamic response of aluminium containing TRIP steel and its constituent phases, Mat Sci Eng a-Struct 460-461 (2007) 516-524.

[18] G.B.O.a.M. COHEN, A mechanism for the strain-induced nucleation of martensitic transformations, Journal of the Less-Common Metals 28 (1972) 107-118.

[19] H.K.D.H. Bhadeshia, Mathematical modelling of weld phenomena 2, Institute of Materials, London, 1995.

[20] M.C.G.B.O.W.S. Owen, Martensite : a tribute to Morris Cohen, ASM International, Ohio, USA, 1992.

[21] J.R. Patel, M. Cohen, Criterion for the Action of Applied Stress in the Martensitic Transformation, Acta Metall Mater 1(5) (1953) 531-538.

[22] G.F. Bolling, R.H. Richman, Plastic Deformation-Transformation of Paramagnetic F C C Fe-Ni-C Alloys, Acta Metall Mater 18(6) (1970) 673-&.

[23] J.Y. Choi, J. Lee, K. Lee, J.Y. Koh, J.H. Cho, H.N. Han, K.T. Park, Effects of the strain rate on the tensile properties of a TRIP-aided duplex stainless steel, Mat Sci Eng a-Struct 666 (2016) 280-287.

[24] X.C. Wei, R.Y. Fu, L. Li, Tensile deformation behavior of cold-rolled TRIP-aided steels over large range of strain rates, Mat Sci Eng a-Struct 465(1-2) (2007) 260-266.

[25] K. Li, V.S.Y. Injeti, R.D.K. Misra, Z.H. Cai, H. Ding, On the strain rate sensitivity of aluminum-containing transformation-induced plasticity steels: Interplay between TRIP and TWIP effects, Mat Sci Eng a-Struct 711 (2018) 515-523.

[26] Y.T. Tsai, C.R. Lin, W.S. Lee, C.Y. Huang, J.R. Yang, Mechanical behavior and microstructural evolution of nanostructured bainite under high-strain rate deformation by Hopkinson bar, Scripta Materialia 115 (2016) 46-51.

[27] W. Wang, M. Li, C. He, X. Wei, D. Wang, H. Du, Experimental study on high strain rate behavior of high strength 600-1000MPa dual phase steels and 1200MPa fully martensitic steels, Mater Design 47 (2013) 510-521.

[28] H.D. Yu, Y.J. Guo, X.M. Lai, Rate-dependent behavior and constitutive model of DP600 steel at strain rate from 10(-4) to 10(3) s(-1), Mater Design 30(7) (2009) 2501-2505.

[29] S. Oliver, T.B. Jones, G. Fourlaris, Microstructure and dynamic material performance of high strength and ultra high strength strip steels, Mater Sci Tech-Lond 23(1) (2007) 55-62.

[30] T. Rahmaan, A. Bardelcik, J. Imbert, C. Butcher, M.J. Worswick, Effect of strain rate on flow stress and anisotropy of DP600, TRIP780, and AA5182-O sheet metal alloys, International Journal of Impact Engineering 88 (2016) 72-90.

[31] O. Leon-Garcia, Micromechanisms of Failure under Static Loading in Sheet Metals for Automotive Applications, Technische Universiteit Delft, Delft, 2013.

[32] C. Zener, Fracturing of metals, 3 ed., ASM, Metals park, Ohio, 1948.

[33] V.A. Lubarda, M.S. Schneider, D.H. Kalantar, B.A. Remington, M.A. Meyers, Void growth by dislocation emission, *Acta Mater* 52(6) (2004) 1397-1408.

[34] S. Traiviratana, E.M. Bringa, D.J. Benson, M.A. Meyers, Void growth in metals: Atomistic calculations, *Acta Mater* 56(15) (2008) 3874-3886.

[35] T.R. Bieler, P. Eisenlohr, F. Roters, D. Kumar, D.E. Mason, M.A. Crimp, D. Raabe, The role of heterogeneous deformation on damage nucleation at grain boundaries in single phase metals, *Int J Plasticity* 25(9) (2009) 1655-1683.

[36] C.C. Tasan, M. Diehl, D. Yan, C. Zambaldi, P. Shanbhag, F. Roters, D. Raabe, Integrated experimental-simulation analysis of stress and strain partitioning in multiphase alloys, *Acta Mater* 81 (2014) 386-400.

[37] C.C. Tasan, J.P.M. Hoefnagels, M. Diehl, D. Yan, F. Roters, D. Raabe, Strain localization and damage in dual phase steels investigated by coupled in-situ deformation experiments and crystal plasticity simulations, *Int J Plasticity* 63 (2014) 198-210.

[38] C.C. Tasan, J.P.M. Hoefnagels, M.G.D. Geers, Identification of the continuum damage parameter: An experimental challenge in modeling damage evolution, *Acta Mater* 60(8) (2012) 3581-3589.

[39] D.S. Yan, C.C. Tasan, D. Raabe, High resolution in situ mapping of microstrain and microstructure evolution reveals damage resistance criteria in dual phase steels, *Acta Mater* 96 (2015) 399-409.

[40] Q. Lai, O. Bouaziz, M. Goune, L. Brassart, M. Verdier, G. Parry, A. Perlade, Y. Brechet, T. Pardoen, Damage and fracture of dual-phase steels: Influence of martensite volume fraction, *Mat Sci Eng a-Struct* 646 (2015) 322-331.

[41] E. Ahmad, T. Manzoor, K.L. Ali, J.I. Akhter, Effect of microvoid formation on the tensile properties of dual-phase steel, *J Mater Eng Perform* 9(3) (2000) 306-310.

[42] F. Archie, X.L. Li, S. Zaeferrer, Micro-damage initiation in ferrite-martensite DP microstructures: A statistical characterization of crystallographic and chemical parameters, *Mat Sci Eng a-Struct* 701 (2017) 302-313.

[43] M. Kuzmina, D. Ponge, D. Raabe, Grain boundary segregation engineering and austenite reversion turn embrittlement into toughness: Example of a 9 wt.% medium Mn steel, *Acta Mater* 86 (2015) 182-192.

[44] F. Nikbakht, M. Nasim, C. Davies, E.A. Wilson, H. Adrian, Isothermal embrittlement of Fe-8Mn alloys at 450 degrees C, *Mater Sci Tech-Lond* 26(5) (2010) 552-558.

[45] N.H. Heo, J.W. Nam, Y.U. Heo, S.J. Kim, Grain boundary embrittlement by Mn and eutectoid reaction in binary Fe-12Mn steel, *Acta Mater* 61(11) (2013) 4022-4034.

[46] R. Yang, D.L. Zhao, Y.M. Wang, S.Q. Wang, H.Q. Ye, C.Y. Wang, Effects of Cr, Mn on the cohesion of the  $\gamma$ -iron grain boundary, *Acta Mater* 49(6) (2001) 1079-1085.

[47] P. Lejček, M. Šob, An analysis of segregation-induced changes in grain boundary cohesion in bcc iron, *J Mater Sci* 49(6) (2014) 2477-2482.

[48] F.A. Wu R, Olson GB., Effects of carbon on Fe-grain-boundary cohesion: First-principles determination., *Phys Rev B Condens Matter*. (1996 ) 7504-7509.

[49] R.J. Asaro, A. Needleman, Overview .42. Texture Development and Strain-Hardening in Rate Dependent Polycrystals, *Acta Metall Mater* 33(6) (1985) 923-953.

[50] T.W.J. de Geus, F. Maresca, R.H.J. Peerlings, M.G.D. Geers, Microscopic plasticity and damage in two-phase steels: On the competing role of crystallography and phase contrast, *Mech Mater* 101 (2016) 147-159.

[51] N. Jia, R.L. Peng, Y.D. Wang, G.C. Chai, S. Johansson, G. Wang, P.K. Liaw, Interactions between the phase stress and the grain-orientation-dependent stress in duplex stainless steel during deformation, *Acta Mater* 54(15) (2006) 3907-3916.

[52] N. Jia, R. Lin Peng, D.W. Brown, B. Clausen, Y.D. Wang, Tensile Deformation Behavior of Duplex Stainless Steel Studied by In-Situ Time-of-Flight Neutron Diffraction, *Metallurgical and Materials Transactions A* 39(13) (2008) 3134.

[53] A. Needleman, V. Tvergaard, Comparison of Crystal Plasticity and Isotropic Hardening Predictions for Metal-Matrix Composites, *J Appl Mech-T Asme* 60(1) (1993) 70-76.

[54] E.E. Nugent, R.B. Calhoun, A. Mortensen, Experimental investigation of stress and strain fields in a ductile matrix surrounding an elastic inclusion, *Acta Mater* 48(7) (2000) 1451-1467.

[55] K. Kwak, T. Mayama, Y. Mine, K. Takashima, Micro-tensile Behaviour of Low-alloy Steel with Bainite/martensite Microstructure, *Isij Int* 56(12) (2016) 2313-2319.

## Chapter 3 Materials and methodology

**Abstract.** In the current chapter the studied materials is introduced first, followed by a comprehensive description of experimental tools used to perform mechanical tests and to characterize the microstructures. Two grades of bainitic multiphase steels with low and high silicon content are considered in this study (section 3.1.1 and 3.1.2). A general overview with regard to the materials production history, dilatometry and annealing cycles are presented in sections 3.1.3, 3.1.4 and 3.1.5, respectively. Details of mechanical tests, including quasi-static and dynamic tensile tests, to study micro-mechanisms of damage initiation and the high strain rate mechanical response of the produced bainitic steels are reported in section 3.2. Section 3.3 illustrates the Digital Image Correlation (DIC) technique employed for high strain rate tests. Characterization techniques such as EBSD and X-ray diffraction before and after mechanical tests are introduced in section 3.4. In addition, section 3.5 particularly explains the crystal orientation mapping technique, whereas section 3.6 mentions the image based technique used for damage quantification. Along with experimental techniques, modelling tools are employed in order to predict plastic deformation behavior and orientations susceptible to damage initiation (see section 3.7). First, the constitutive hardening model of Johnson-Cook for the prediction of strain rate sensitivity is introduced in section 3.7.1. Second, the Visco-Plastic Self-Consistent (VPSC) crystal plasticity model is introduced, and additionally a particular formulation associated to VPSC90 is given. A new strain rate sensitivity approach is used in VPSC90 in order to simulate high strain rate deformations of the materials under consideration. Moreover, a physical hardening model is implemented in the crystal plasticity framework in order to consider the individual influence of microstructural variables such as phase fraction, lath size and dislocation density on the quasi-static and dynamic mechanical responses of bainitic multiphase steels under consideration in this study.

### 3.1 Materials

Bainitic multiphase steels (martensite and retained austenite) are considered to be promising candidates for automotive applications [1, 2]. Bainitic is characterized as a finer structure with higher dislocation density compared to polygonal ferrite, which intrinsically results in high yield and tensile strength [3]. The presence of second phase constituents such as martensite and retained austenite can modify the mechanical properties of bainitic steels. Retained austenite helps to improve the ductility while martensite increases the strength. Therefore, finding an optimum combination of the second phase constituents results in enhanced properties. The individual micro-mechanical response of the second phase constituents can be varied by many factors such as composition (e.g. carbon, silicon and manganese content), morphology (i.e. size, shape and distribution), transformation temperature and crystallographic orientation [4-6].

In the current study, two grades of bainitic steels were produced on a pilot line. These grades are investigated in order to understand their potential application for car-body structure. The first grade is produced with low silicon content while the second grade has high silicon content. The detailed composition and thermodynamic characteristics of these grades will be introduced in sections 3.2.1 and 3.2.2.

#### 3.1.1 High silicon grade

The chemical composition of bainitic steels is crucial, as it can affect the final microstructure and the associated mechanical properties. Carbon, manganese and silicon are the main alloying elements, although additions of chromium and aluminium may also be incorporated [7]. Carbon is of a crucial importance for the final mechanical properties due to the fact that this element controls the fraction and properties of the second phase constituents. The effect of carbon on morphological and micro-mechanical behaviour of martensite and retained austenite phases is inevitable [4]. Also, the weldability of the steel is strongly dependent on the carbon content, such that it may have a detrimental effect when larger than 0.2 wt% [8]. The chemical composition of the high silicon (HiSi) grade is shown in table 3-1. The design of the alloy is aimed to make cold rolled and annealed laboratory substrates with strength levels comparable to those of advanced or ultra-high strength steels ( $> 950\text{ MPa}$ ).

Table 3-1 Chemical composition of the HiSi grade.

Elements	C%	Mn%	Si%	Cr%	Al%	P%	S%	N%
<b>Ingot</b>	0.215	1.99	1.30	<0.005	0.027	0.007	0.0026	0.005

### 3.1.2 Low silicon grade

It was decided to design the second grade in such a way that the low silicon (LoSi) grade delivers comparable strength levels as the HiSi grade for similar processing conditions. This is possible if the difference in silicon content is counter-balanced by varying other alloying elements, e.g. Mn or Cr. The chemical composition of the LoSi grade is depicted in table 3-2.

Table 3-2. Chemical composition of the LoSi grade.

Elements	C%	Mn%	Si%	Cr%	Al%	P%	S%	N%
<b>Ingot</b>	0.215	1.97	0.10	0.61	0.020	0.007	0.0027	0.005

The levels of P, S and N are representative for the conventional steels in industry. The role of alloying elements such as manganese, silicon, chromium and aluminium in solid solution strengthening is widely known. The solubility of silicon in cementite is extremely low and due to the para-equilibrium transformation, the driving force for precipitation is considerably reduced. As a result of this, silicon prevents the formation of cementite at either the interface of bainitic ferrite and martensite or within the bainite laths [9]. This leads to enrichment of carbon in the untransformed remaining austenite phase during isothermal bainite transformation. Eventually, austenite becomes stable at room temperature [10]. In contrast to Si and Al, which promote the formation of ferrite by increasing the  $Ar_1$  temperature and ease the formation of bainite during cooling [7, 8], Mn is an austenite stabilizer and thus decreases the  $Ar_1$  temperature [11]. Consequently, this alloying element results in the formation of martensite at lower cooling rates. Nevertheless, Mn has the disadvantage that in combination with S, it creates MnS inclusions, which may have detrimental effect on the formability of final products [12].

### 3.1.3 Laboratory setup and for hot and cold rolling

Figure 3.1 shows a schematic drawing of the hot rolling pilot line at Tata Steel R&D in IJmuiden. The temperature of the block/slab is monitored with pyrometers at various locations: entry and exit of the single stand mill, and entry and exit of the Run-Out-Table (ROT). The 30 kg ingots are reheated to a furnace temperature of 1250 °C for half an hour and thereafter they get a roughing mill step down to 40 mm thickness followed by cooling to room temperature.

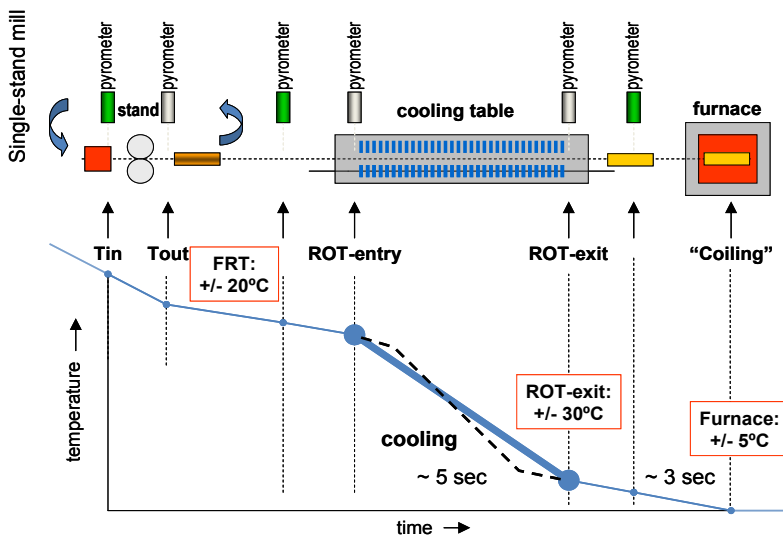


Figure 3-1 Schematic of the laboratory set-up for hot rolling at Tata Steel in IJmuiden.

Then, each roughed ingot is cut into blocks with lengths of 80-120 mm. After reheating of the blocks to 1230°C for half an hour, the hot rolling with the single stand mill starts at about 1150 °C. The blocks are hot rolled in several passes to their aimed final thickness with a finish rolling temperature (FRT) of approximately 880 °C. Then the hot rolled slabs are transported to the Run-Out-Table (ROT) simulator, in which slabs are cooled with a cooling rate (CR) in the range of 20-25 °C/s to arrive at a coiling temperature (CT) of about 630 °C. Thereafter, the slabs are put in the furnace and a standard coiling simulation programme is applied.

For producing cold rolled feedstock, the blocks are hot rolled in 6 steps from 40 to 4 mm thickness. The hot rolled slabs are pickled and thereafter, are cold rolled to a final thickness of 1 mm.

### 3.1.4 Dilatometry

For determination of the general transformation behaviour, Continuous Cooling Transformation (CCT) and Time Temperature Transformation (TTT) diagrams (shown in Appendix A) dilatometer tests are conducted by Tata Steel R&D in IJmuiden using a Bähr dilatometer type DIL 805 in accordance with the procedures described in SEP 1680. Dilatometer samples of LoSi and HiSi are used to determine  $A_{c1}$  and  $A_{c3}$ , the bainite start temperature ( $B_s$ ) and the martensite-start temperature ( $M_s$ ).

Table 3-3. Measured and calculated values of  $A_{c1}$ ,  $A_{c3}$ ,  $B_s$  and  $M_s$  for LoSi and HiSi (°C).

Designation	Measured (Dilatometer)			Calculated (Thermo-calc)		Calculated (empirical eq.)		Calculated (empirical eq.)	
	$A_{c1}$	$A_{c3}$	$M_s$	$A_{e1}$	$A_{e3}$	$A_{e1}$	$A_{e3}$	$B_s$	$M_s$
<b>LoSi</b>	718	805	365	675	779	715	804	556	388
<b>HiSi</b>	715	881	370	682	820	739	853	569	378

Table 3-3 compiles the derived transformation temperatures and, for comparison, the associated equilibrium transformation temperatures computed with Thermo-Calc 4.1 using the TCFE6-Database [13]. As for the dilatometer measurements, a finite heating rate is used, the measured transformation temperatures  $A_{c1}$  and  $A_{c3}$  differ from those expected for equilibrium conditions. Empirical equations [14, 15] for the equilibrium transformation temperatures result in values which are closer to the measured temperatures. Although these empirical equations have been obtained by fitting to equilibrium data taken from literature, they seem to correspond better to measurement conditions applying a very slow heating as in the present measurements.

The measurements were repeated, showing an excellent agreement with the previously determined  $A_c$ -temperatures. Thus, it could be confirmed that the difference between measured and simulated temperatures is due to the influence of the experimental procedure applying slow heating in comparison with the thermodynamic simulation based on the thermodynamic equilibrium state.

Next to the  $A_e$ -temperatures the Bainite and Martensite start temperatures  $B_s$  and  $M_s$  are computed on the basis of the empirical models suggested by van Bohemen [16]. The measured  $M_s$  and calculated  $M_s$  temperatures of the LoSi and HiSi grades are in good agreement.

### 3.1.5 Vatron annealing simulator

The annealing of the cold rolled material (cold reduction of 75%) is performed on a Vatron Annealing Simulator at ThyssenKrupp Steel Europe AG. Compared to the above described dilatometer test, the equipment makes possible to conduct annealing cycles on larger flat samples (110-115mm · 450mm) by conductive heating. High cooling rates ( $CR>70K/s$ ) are achieved by cooled copper sheets, in which the samples are clamped during cooling, in order to assure a constant and fast cooling rate to the whole sample. A high cooling rate is essential in order to avoid the formation of ferrite and/or pearlite constituents during cooling from austenization temperatures to bainite transformation temperature.

The nature of annealing cycles is as follows: first, an austenization process, in which the two temperatures of 820 and 920°C for the LoSi grade, and 860 and 920°C for the HiSi grade are employed. The holding time at the austenization temperatures is 120 s. Second, following the austenization process, samples are quenched at 100 K/s to the bainite holding temperatures of 390 and 450°C for 14 and 120 s. Eventually, samples are quenched from the bainite holding temperatures to room temperature with cooling rate of 20 K/s.

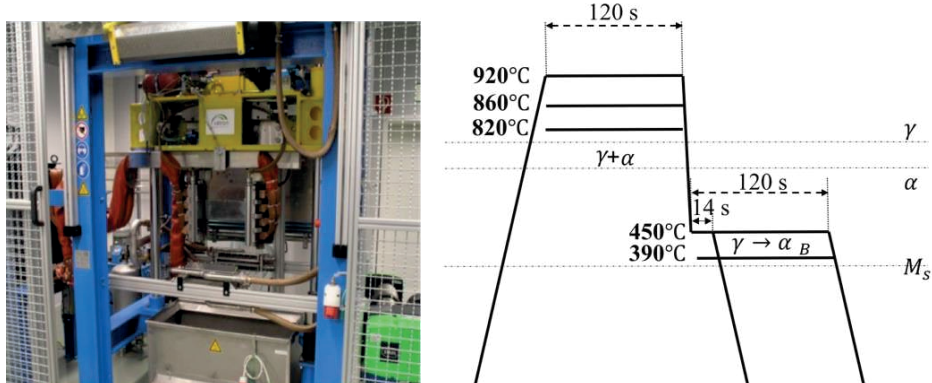


Figure 3-2 Vatron annealing simulator at TKSE Duisburg and the corresponding schematic illustration of annealing cycles.

Table 3-4. Samples nomenclature and associated annealing cycles.

Steel	Sample	$T_y$ (°C)	$t_s$ (s)	$T_B$ (°C)	$t_B$ (s)
LoSi	<b>HT (High Temperature)</b>	920	120	450	120
	<b>LT (Low Temperature)</b>	820	120	450	120
	<b>LB (Low Bainite temperature)</b>	920	120	390	120
HiSi	<b>HT (High Temperature)</b>	920	120	450	120
	<b>LT (Low Temperature)</b>	860	120	450	120
	<b>SB (Short Bainite holding time)</b>	920	120	450	14

## 3.2 Mechanical test

In the current study, three mechanical tests are performed which are micro-hardness, tensile test and Split Hopkinson Tensile Bar (SHTB).

### 3.2.1 Micro-hardness test

Vickers micro-hardness measurements are conducted in order to study the effect of martensite bands topology, as meso-scale heterogeneities, on the micro-mechanical behavior of banded microstructures. To this purpose, measurements are performed along RD and normal direction (ND) on 2% Nital etched HT and LT samples from the LoSi grade. In order to have enough data, 30 indents along RD are performed separately at two particular regions: the bainitic matrix and martensitic bands. These regions are indented with a load of 5 gf, which allows for a more local response of the aimed regions. In addition, two profiles of 20 indents along ND are conducted with a load of 10 gf to study the meso-scale heterogeneities and the corresponding scatter of each sample.

### 3.2.2 Tensile test

Quasi-static uniaxial tensile tests are conducted at room temperature with strain rates of  $2 \cdot 10^{-5}$  and  $8 \cdot 10^{-3}$  s<sup>-1</sup> in the elastic and plastic regions of the flow curve, respectively, in order to assess the mechanical response of the samples to uni-axial tensile loading. Tensile tests are performed according to the DIN EN 6892-1 standard using a Zwick Z100® tensile machine. Dog-bone specimens with width of 6.25 mm and gauge length of 25 mm, are loaded along the rolling direction (RD) and transversal direction (TD). Figure 3-3 shows the schematic illustration of the tensile specimen geometry. Two tests per

sample are conducted, whereby strains are measured by the extensometer. The quasi-static mechanical response of the studied materials is shown in chapter 4.

Tensile tests are also used to study micro-mechanisms of damage initiation. In order to assess damage evolution, interrupted tensile tests are carried out in uniform and non-uniform regions of the tensile curves. The outcome of this investigation is reported in chapter 5.

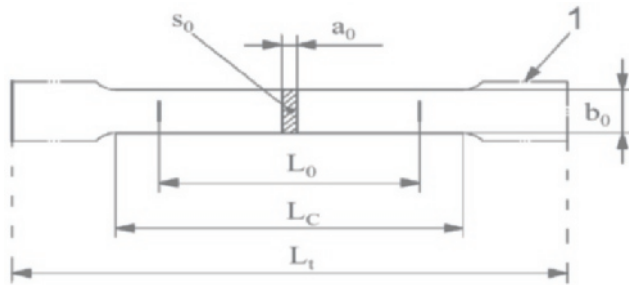


Figure 3-3 Schematic illustration of the tensile specimen geometry.  $L_t=83\text{mm}$ ,  $L_c=37.5\text{mm}$ ,  $L_0=25\text{mm}$ ,  $b_0=6.25\text{mm}$ .

Tensile properties are calculated from experiments using standard equations [17]. The engineering stress is calculated by the expression below:

$$S = \frac{P}{A_0} \quad [1]$$

where  $P$  is the force and  $A_0$  is the initial cross section of the tensile specimen gauge. The engineering strain is calculated as follows:

$$e = \frac{l - l_0}{l_0} \quad [2]$$

where  $l$  and  $l_0$  are the length at the corresponding force and initial gauge length of the tensile specimen, respectively. In addition, in order to calculate the true stress and strain curve from the engineering curve the following equations are employed:

$$\sigma = S(1 + e) \quad [3]$$

$$\varepsilon = \ln(1 + e) \quad [4]$$

True curves can be plotted using the above equations until the point of Ultimate Tensile Strength (UTS:  $\sigma(\varepsilon_u) = d\sigma/d\varepsilon(\varepsilon_u)$ ) where the maximum force during a tensile test is reached. The strain at the UTS point is the maximum uniform strain. In addition, it is possible to calculate merely the plastic region of the true curve, once the yield stress point is determined e.g. following the 0.002 offset method. Thus, it is possible to subtract the elastic strain from the total strain ( $e_p = e - s/E$ ), where  $E$  is the elastic modulus of the tensile curve. Additionally, in order to calculate the fracture strain, the area of the fracture surface is measured by optical microscopic images. The fracture strain is calculated by the following equation:

$$\varepsilon_f = \ln \frac{A_0}{A_f} \quad [5]$$

where  $A_0$  and  $A_f$  are the initial cross-sectional and fracture surface area, respectively.

### 3.2.3 Split Hopkinson Tensile Bar

High strain rate tensile tests are performed with the Split Hopkinson Tensile Bar (SHTB) setup at Ghent University [18]. The results of this work are presented in chapter 4. The SHTB setup is shown in figure 3-4b. The setup consists of two long aluminium bars: an input bar of 6 m and an output bar of 3.15 m, both with a diameter of 25 mm. A dog-bone flat specimen (cf. fig. 3-4a) is located between the input and output bars using a pin and hole clamping configuration. A tube shape impactor is covering the input bar and is accelerated towards an anvil at the outer end of the bar by the impact of a fork. This

generates an incident wave as shown in figure 3-5. The incident wave travels through the input bar and interact with the specimen and generates reflected and transmitted waves, which are captured by the strain gauges in the input and the output bars (cf. fig. 3-6).

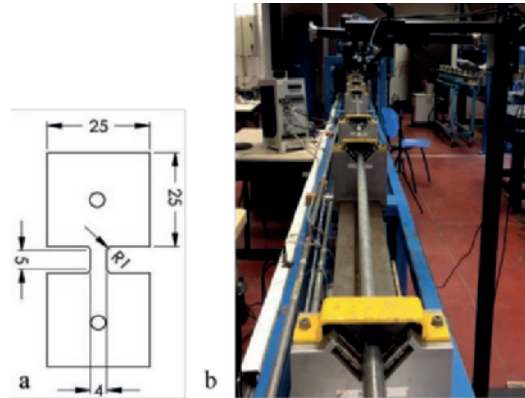


Figure 3-4 Split Hopkinson Tensile Bar (SHTB) setup at Ghent University: (a) SHTB specimen geometry and (b) SHTB setup.

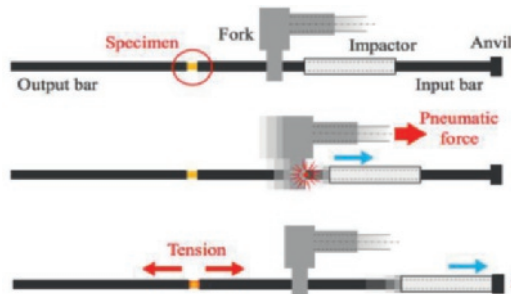


Figure 3-5 Schematic demonstration of SHTB setup: a pneumatic force impulses the fork, which hits the impactor. The impactor is then accelerated towards anvil of the input bar, generating an incident wave directed to the specimen [19].

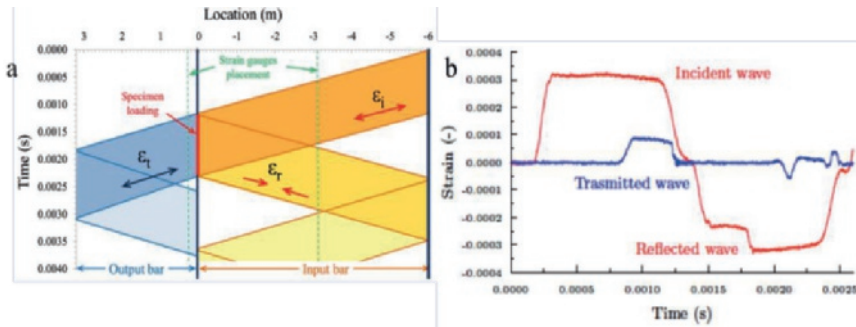


Figure 3-6 SHTB waves generation in the input and output bar: (a) LaGrange diagram of a SHTB experiment, where the length of the input and output bars are 6 m and 3.2 m, respectively. The arrows indicate whether the wave is in tension or compression. The vertical green lines indicate the placement of the strain gauges, in the regions of the bar where only one wave is present at a time. (b) Real signals measured by strain gauges [19].

The waves captured by strain gauges are translated to strain rate, strain and stress using the equations given by Kolsky [20]. The specific geometry of the SHTB specimen ensures an acceptable homogeneity of strain along the gauge length, as discussed in [21, 22]. Therefore, by assuming homogeneous deformation in the gauge length of the specimen, the mean stress is calculated from the stresses at the bar-specimen interface, whereas the strain rate is derived from the corresponding velocities:

$$S_m(t) = \frac{S_{in}(t) + S_{out}(t)}{2} = \frac{A_b E_b}{2 A_s} [e_t(t) + e_r(t) + e_i(t)] \quad [6]$$

$$\dot{e}_m(t) = \frac{v_{out}(t) + v_{in}(t)}{L} = \frac{C_b}{L} [e_i(t) - e_t(t) - e_r(t)] \quad [7]$$

where  $E_b$  and  $A_b$  are the Young modulus and the cross-sectional area of the bar, respectively.  $A_s$  is the cross-sectional area of the specimen at its gauge and  $L$  is the gauge length.  $S$  and  $e$  are engineering stress and strain, and sub-indices  $i$ ,  $t$  and  $r$  refer to incident, transmitted and reflected waves.

Using the equations above, it is possible to obtain the mean strain by the integral of strain rate with respect to time:

$$e_m(t) = \frac{C_b}{L} \int_0^t [e_i(t) - e_t(t) - e_r(t)] dt \quad [8]$$

where  $C_b$  is the wave propagation speed (the speed of sound) in the bars.

The small length of the specimen provides a quasi-static equilibrium condition from the early stages of loading, thus:

$$e_t(t) = e_r(t) + e_i(t) \quad [9]$$

which results in the final equations for the specimen as follows:

$$S(t) = S_m(t) = \frac{A_b E_b}{A_s} e_t(t) \quad [10]$$

$$e_t(t) = -2 \frac{C_b}{L} \int_0^t e_r(t) dt \quad [11]$$

$$\dot{e}(t) = -2 \frac{C_b}{L} e_r(t) \quad [12]$$

The above engineering tensile parameters can be converted into true curves using equations (3) and (4).

### 3.3 Digital Image Correlation (DIC)

Digital image correlation is employed as an extra method for strain calculations during high strain rate experiments. This method is based on the image processing algorithms. This technique is based on the local displacement of patterns, which are tracked during a deformation to obtain strain values. To this purpose, prior to testing, a random black speckle pattern is applied on the white painted specimens. During the dynamic tests, the deformation of the speckle pattern is captured by a Photron AX200® high speed camera at a framerate of 30,000 fps. The size of the images is 256x640 pixels. The recorded images are post-processed using the MatchID® software with a step size of 6 pixels and a subset size of either 17 or 19 pixels depending on the speckles size. Figure 3-7 depicts the geometry of the GL5 specimen and the strain component in the tensile direction, at a moment after necking, obtained by DIC analysis.

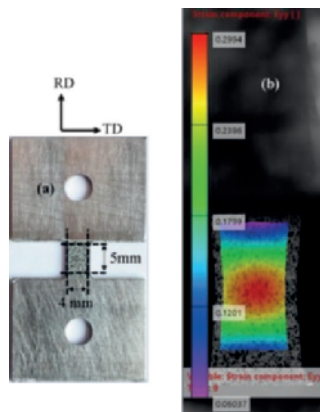


Figure 3-7 DIC analysis; (a) GL5 specimen with the speckle pattern at the gauge and (b) effective plastic strain calculation.

### 3.4 Microstructure characterization

Prior to characterizing the microstructures of the developed bainitic steels, conventional metallography procedures are performed such as grinding and polishing. The polishing procedures applied for all 6 samples at the annealed state consisted of polishing from 9 up to 1  $\mu\text{m}$  using diamond suspension products. The last step of polishing is usually conducted with OPS (Oxide Polishing Suspension) in order to remove the deformation layer induced from the previous mechanical polishing steps. OPS consists of silicon dioxide ( $\text{SiO}_2$ ) particles with an average size of 0.05  $\mu\text{m}$  suspended in an aqueous liquid with a pH of 9.8. The alkaline medium together with small particles of the suspension produces a chemo-mechanical action during this final polishing step, which in combination with long polishing times and reduced contact force is an effective method to remove the deformation layer from the previous polishing steps [23].

For microstructure characterization, various techniques are employed, including Light Optical Microscopy (LOM), Scanning Electron Microscopy (SEM), Electron Probe Micro-analysis (EMPA) using Wavelength Dispersive Spectroscopy (WDS) and Energy Dispersive X-ray Spectroscopy (EDS) detectors, X-ray Diffraction and Electron Backscatter Diffraction (EBSD).

### 3.4.1 Inclusions

In the case of Light Optical Microscopy (LOM), a Keyence VHX-5000™ microscope is used for quantification of inclusions ( $\text{Al}_2\text{O}_3$  and MnS). To this purpose, an area of  $1.5 \times 1.5 \text{ cm}^2$  is studied on two different samples from each grade, by stitching approximately 360 photos with 300X magnification. These measurements are post-processed based on grey scale histogram and binarized into white (matrix) and black (inclusions). For the determination of the chemical composition of the inclusions FEI® SEM-Quanta FEG 450 equipped with an EDAX system for EDS analysis is used. The inclusions are detected at the working distance of 5 mm using an acceleration voltage of 15 kV. Figure 3-8 depicts two inclusions detected by EDS analysis.

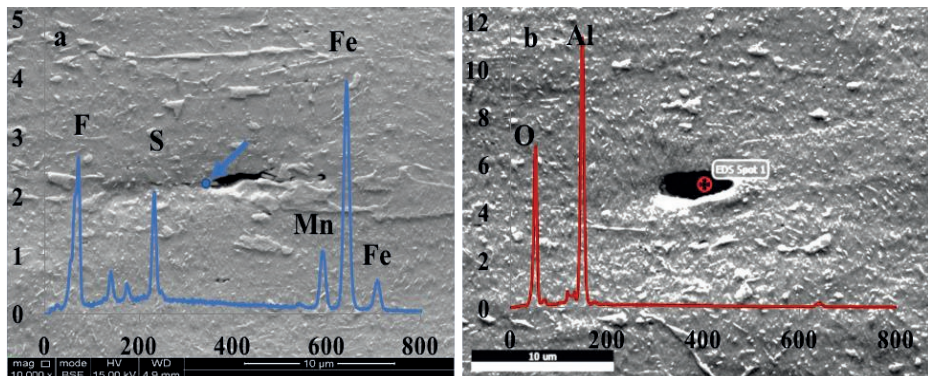


Figure 3-8 SEM micrographs of the inclusions and their corresponding chemical analysis: (a) a MnS stringer along the rolling direction (RD) and (b)  $\text{Al}_2\text{O}_3$  particle. The x-axis of the curves is along the RD and the y-axis is along the normal direction (ND).

### 3.4.2 Grain size

For the matrix grain size a scanning electron microscope of type FEI® SEM-Quanta FEG 450 equipped with electron backscatter diffraction (EBSD) detector is used. The EBSD measurements are carried out with a step size of  $0.05 \mu\text{m}$  and the EBSD results are post processed with the EDAX-OIM Analysis™ software version 7.2.1. On the EBSD scans conducted on the RD-ND section, grains are defined by a 5-degree misorientation threshold and a minimum number of 5 pixels. The grain size is measured based on the linear intercept method and by averaging lines in both vertical and horizontal directions for each phase [24].

### 3.4.3 Constituents characterization

The identification of second phase constituents such as retained austenite (RA) in the HiSi grade, martensite in both grades and carbides in the LoSi grade is made by EBSD technique and SEM micrographs. First and foremost, in order to distinguish bainite from martensite, the EBSD diffraction pattern sharpness, quantified by the Image Quality (IQ) factor, is employed. The martensite phase exhibits a crystal structure that is intrinsically distorted and exhibits a far higher dislocation density compared to bainite. Thus, individual characteristics of bainite and martensite such as grain size and volume fraction are assessed by the grain average image quality (GAIQ) parameter in order to distinguish these two phases [5, 25, 26]. In this regard, the total martensite phase is referred to as MA islands, indicating martensite blocks with a negligible fraction of inter-lath retained austenite, and Auto-Tempered Martensite that contains carbides (ATM). The ATM phase is revealed by Nital etching. However, in order to quantify the fraction of MA islands separately from the total martensite fraction, the surface of the samples is first activated with ethanol and then etched with Klemm color etchant (50 mL saturated aqueous sodium thiosulfate, 1 g potassium metabisulfite). Ten backscatter electron (BSE) images, which exhibit a better contrast between the bainite matrix and the MA islands compared to secondary electron (SE) images, are recorded for each sample and binarized into black (martensite) and white (bainite) contrast. The fraction of MA islands is then measured by image processing. The fraction of carbides in the LoSi grade is estimated using the similar method as for MA islands, which was etching and image processing.

### 3.4.4 X-ray Diffraction

The presence of silicon in the HiSi grade leads to the stabilization of the austenite phase at room temperature [10]. X-ray diffraction technique (Bruker-D8) is used to quantify the fraction of RA according to ASTM E975-13. The  $\{200\}_{\alpha}$ ,  $\{211\}_{\alpha}$ ,  $\{200\}_{\gamma}$  and  $\{220\}_{\gamma}$  diffraction peaks are taken into account.

### 3.4.5 Wavelength Dispersive Spectroscopy

A JEOL JXA 8900R® microscope is used for Electron Probe Microanalysis (EPMA) in order to detect the martensite banding phenomenon in the developed bainitic steels. This analysis is performed using an electron beam with energy of 10 keV and current of 50 nA with step size of 0.5  $\mu\text{m}$  employing Wavelength Dispersive Spectroscopy (WDS) to ensure the presence of banding phenomenon within the

microstructure. The composition at each analysis location of the sample is determined using X-ray intensities of constituent's elements after background correction relative to the corresponding intensities of reference samples. The obtained intensity ratios are processed with the matrix correction program CIRZAF®[27].

### 3.5 Crystal orientation mapping

Crystal orientation mapping is employed at two different stages: prior to the mechanical tests and after imposing deformation to materials. The material textures are analyzed by the EBSD technique. The electron backscatter diffraction (EBSD) terminology originally refers to the backscatter Kikuchi diffraction (BKD). The Kikuchi patterns form by the specific interaction of the electron beam and the crystal structure of a specimen. The Kikuchi pattern was initially observed in 1928 by Nishikawa and Kikuchi during Transmission Electron Microscopy (TEM) analysis in backscattering mode. These patterns reveal information with regard to crystal orientation of the diffracted volume [28]. Nowadays, EBSD scans are automated and local crystallographic orientations are captured. The crystallographic information is post-processed with the commercial software EDAX-OIM Analysis™. This technique provides a coupled quantitative topological and crystallographic orientation based information of most crystalline materials. Moreover, the EBSD technique can be used to investigate the local strain gradients or strain partitioning effect between bainite (soft phase) and martensite (hard phase). To this purpose, two crystal orientation based parameters are used [29]. First, the Kernel Average Misorientation (KAM), which is calculated for each pixel by averaging the misorientations between the central point of the kernel and its surrounding. Second, the Grain Reference Orientation Deviation (GROD), which indicates the misorientation of each pixel within a defined grain with respect to a reference orientation (normally, the single average orientation of the grain). While the former parameter represents short range orientation gradients, the latter reveals long range orientation gradients.

The physics of EBSD pattern formation and capabilities of the system in terms of angular and special resolutions are explained in details by Orlando Leon Garcia [23].

Figure 3-9 demonstrates the main components of a SEM microscope equipped with EBSD detector. A sample with an inclination of 70° from the horizontal is mounted inside a SEM chamber. A phosphor screen is fluoresced by electrons from the sample to form the Kikuchi patterns. In addition, there is a sensitive charge coupled device (CCD) video camera to visualize the diffraction patterns on the phosphorus screen. There is an electronic hardware that controls the SEM, including the stage, beam

position, focus and magnification. Besides, a dedicated software controls the measurement, analyzes the diffraction patterns, processes and displays the results. There can also be an optional electron detector which is mounted below the phosphorus screen for detection of the forward scattered electrons from the sample.

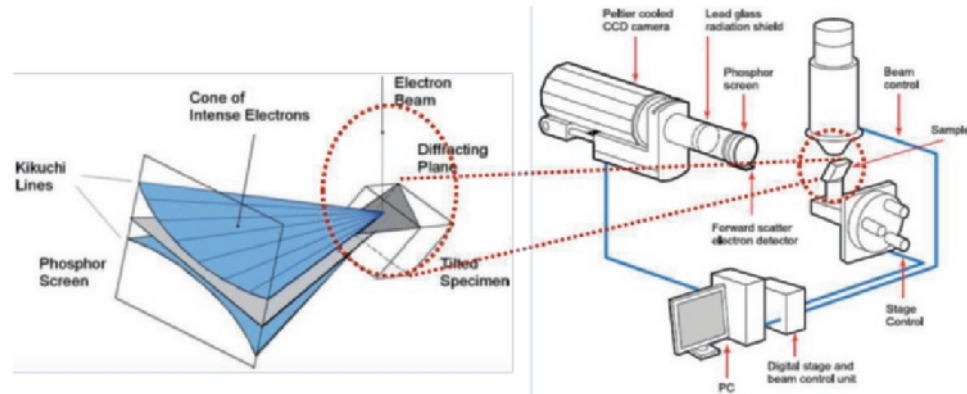


Figure 3-9 Principal components of an EBSD system.

The bulk texture of the materials is measured by EBSD analysis. In order to calculate the Orientation Distribution Function (ODF), either EDAX-OIM™ or MTEX [30] software is used. The program calculates the ODF by the series expansion method. The maximum rank of spherical harmonics used here is  $L_{\max}=22$ .

EBSD scans at the annealed state of materials are usually performed with a step size of  $0.1\mu\text{m}$  with acceleration voltage of 20 kV. However, scans performed after imposing any deformation level have a step size of either 50 or 70 nm with acceleration voltage of 15kV. It is important to mention that for metallographic characterization of the deformed samples, the last polishing step (OPS) is conducted for at least 1 hour with a very low pressure.

## 3.6 Damage quantification and image processing

According to the systematic study conducted by Tasan *et al.* [31], microscopic based (i.e. 2D SEM and 3D X-ray micro-tomography (X $\mu$ T)) compared to mechanical based techniques provides valuable information regarding the strain levels and the involved micro-mechanisms in damage initiation and evolution. However, an underestimation of damage events is expected in the 2D SEM technique where

voids are smeared-out by mechanical polishing. Lai *et al.* [32] reported the advantage of the SEM based technique due to its high resolution and its ability to detect smaller voids compared to X $\mu$ T. Nevertheless, the advantage of XR tomography over 2D SEM technique in the 3D visualization and growth characterization of individual voids has been reported by Landron *et al.* [33, 34].

In the current study, a high resolution FEG-SEM (FEI Nova 600) is used to quantify the voids evolution as a function of the true plastic strain on the RD-ND section in the middle width of the fractured tensile samples loaded along RD. Three parameters are used to quantify the evolution of damage: void number density (VD), void area fraction (VAF) and perimeter of voids. In addition, it is possible to visualize the distribution of the voids within the microstructure. True plastic strain values are calculated in equally spaced intervals from the fracture surface based on the transversal and normal strains. An area of approximately 1 mm<sup>2</sup> is scanned by running an automated image acquisition software to capture over 1000 SEM micrographs per sample. The contiguous collection of micrographs with a magnification of 4000X, with a size of 1024x884 pixels and a pixel resolution of 31 nm, could enable to detect the micro-voids within the microstructure. All images are merged and processed to quantify voids by image processing algorithms using Matlab<sup>®</sup> and ImageJ<sup>®</sup>. A void size criterion is considered in which all the voids larger than 0.1  $\mu$ m<sup>2</sup> ( $\approx$  33 pixels) are counted.

### 3.7 Plastic deformation modelling

Plastic deformation models were developed in order to predict the mechanical response of a material under various loading conditions. Modelling techniques provide the possibility to simulate mechanical processes in detail, which can help to avoid performing expensive, time consuming or, sometimes, totally infeasible experiments. Various models have been developed by the scientific and engineering community. The decision to use one or another model usually depends on a compromise between desired accuracy, computational cost and range of applications [19].

In this section, two different models that are employed in the current study are illustrated. First, the phenomenological plasticity model of Johnson-Cook is introduced, whereby the macroscopic mechanical response of a material is modelled by a few numerical parameters. This model has the capability to consider the effect of temperature and strain rate on plastic deformation of a material, cf. section 3.7.1. In section 3.7.2, the theory of the Visco-Plastic Self-Consistent (VPSC) crystal plasticity model is presented. This section describes also a more recent implementation of the VPSC model

(VPSC90) reported by Ricardo Lebensohn [35]. Later, the physical hardening model and the new strain rate sensitivity approach are described.

### 3.7.1 Johnson-Cook model

The Johnson-Cook (J-C) model is one of the empirical hardening models commonly used to predict the flow behavior of metals [36]. This model is specially preferred for the modelling of deformation processes in which temperature softening and strain rate hardening are involved, such as high strain rate and high temperature loading conditions. The J-C model is a phenomenological model, which by definition requires a few fitting parameters. Normally, in order to fit these parameters, some reference experiments are required.

The model includes three parameters A, B and n that describe the plastic flow of the material at reference values of strain rate and temperature ( $\dot{\varepsilon}_0$  and  $T_r$ ). In addition, two parameters that determine the sensitivity of the material to strain rate ( $C$ ) and temperature ( $m$ ) are required in order to predict the flow behavior at a specific loading condition. The model is expressed as:

$$\begin{aligned}\sigma(\varepsilon_p) &= \sigma_0(\varepsilon_p)k_{\dot{\varepsilon}}(\dot{\varepsilon})k_T(T) \\ &= [A + B\varepsilon_p^n] \left[ 1 + C \ln \frac{\dot{\varepsilon}}{\dot{\varepsilon}_0} \right] \left[ 1 - \left( \frac{T - T_r}{T_{melt} - T_r} \right)^m \right]\end{aligned}\quad [13]$$

The expression above consists of three factors: first, the  $\sigma_0(\varepsilon_p)$  factor, that accounts for the flow behavior of the material at the reference state and temperature. Second, the  $k_{\dot{\varepsilon}}(\dot{\varepsilon})$  factor that takes into account the strain rate sensitivity, and third the thermal softening factor,  $k_T(T)$ . It should be noted that both strain rate sensitivity and thermal softening factors are independent of strain. In a number of research works [37, 38], it has been reported that for a wide range of test conditions this multiplicative type of expression is not accurate enough. However, the J-C model has been successfully used for the simulation of many materials and processes [19, 39, 40].

### 3.7.2 Visco-Plastic Self-Consistent (VPSC) model

Crystal plasticity (CP) based models are developed to simulate the behaviour of polycrystalline materials. These models are intended to predict the macroscopic behavior of the materials based on the specific response of crystal orientations belonging to the material texture. The models are capable to implement the effect of material texture on anisotropy of mechanical response and to predict the

evolution of texture during an externally imposed deformation. This section briefly introduces the viscoplastic self-consistent (VPSC) model as one of the available CP based models. Additionally, a short explanation with regard to alternative CP models that could potentially be used are given. Later, their corresponding advantages and disadvantages are illustrated. Eventually, the formulation of the VPSC model is presented.

It is well established that the anisotropy of the global mechanical response of a polycrystalline aggregate is governed by the anisotropy of properties of its grains and its crystallographic texture. In addition, the orientation change during deformation leads to texture and grain shape changes. Consequently, precise CP models are not only able to simulate the mechanical response of a polycrystal material under a particular imposed deformation mode, but also, they are able to capture the evolution of the texture during deformation. In this regard, several CP based models have been developed.

The most basic CP based models are the static model proposed by Sachs [41] and the Full Constraint model of Taylor [42]. These two models provide a simple correlation between macroscopic mechanical magnitudes and the corresponding microscopic ones at the grain level. The assumption of the Sachs model imposes stress equilibrium, at the expense of strain compatibility, among all grains by assuming that the stress in each grain is equal to the macroscopic stress in the polycrystalline aggregate. Conversely, the Taylor model imposes a uniform strain for all grains at the cost of stress equilibrium.

Unlike the Sachs and Taylor models, self-consistent models do not directly impose stress and strain on individual grains. Instead, an individual grain is considered to act as an inclusion embedded in a homogeneous matrix with the viscoplastic properties of the polycrystal. The correlation between microscopic and macroscopic mechanical magnitudes in the VPSC model is given by the solution of the equivalent inclusion Eshelby problem in each grain and, through an iterative scheme, the polycrystal stress and strain are enforced to coincide with the volumetric averages of said quantities over the grains. VPSC is a more time-consuming formulation compared to the Sachs and Taylor models [19].

Moreover, more complex CP models such as the Finite Element Method and Fast Fourier Transform CP models provide local information at every integration point. However, due to high computational cost, normally these models are limited to smaller number of grains compared to homogenization models (e.g. (Advanced) Lamella-shaped grains (A)LAMEL, Grain Interaction (GIA)/ Generalised Relaxed Constraints (GRC) and Self Consistent (SC) models). Eventually, the choice between the available CP models depends on the nature of the problem, accuracy, computation time and availability.

### 3.7.2.1 VPSC formulation

The VPSC model, developed by Lebensohn and Tomé [35], offers a moderate complexity and a good accuracy. According to the VPSC assumption described earlier, for each grain the interaction equation is defined:

$$\dot{\varepsilon} - \dot{\varepsilon}_g = -\tilde{M}_g (\sigma - \sigma_g) \quad [14]$$

where  $\tilde{M}_g$  is the interaction tensor and uses the solution of the corresponding Eshelby problem [43].  $\sigma_g$  and  $\dot{\varepsilon}_g$  are the stress and strain rate of the grain, respectively.  $\sigma$  and  $\dot{\varepsilon}$  are the corresponding polycrystal magnitudes, that are calculated as the weighted averages of the grain magnitudes:

$$\dot{\varepsilon} = \sum_g w_g \dot{\varepsilon}_g \quad [15]$$

$$\sigma = \sum_g w_g \sigma_g \quad [16]$$

with  $w_g$  the volume fraction of each grain. The plastic strain rate  $\dot{\varepsilon}_g$  is then calculated using the strain rate approach of Assaro and Needleman [44], which approximates the Schmid law for high values of the strain rate sensitivity exponent  $n_s$ :

$$\dot{\varepsilon}_g = \sum_s m_s \dot{\gamma}_s = \dot{\gamma}_0 \sum_s m_s \left( \frac{|m_s \sigma_g|}{\tau_s^c} \right)^{n_s} \operatorname{sgn}(m_s \sigma_g) \quad [17]$$

In the equation above,  $\dot{\gamma}_s$  is the shear rate in the slip system  $s$ ,  $\dot{\gamma}_0$  a normalization factor,  $m_s$  the symmetric Schmid tensor of each slip system, and  $\tau_s^c$  is the critically resolved shear stress (CRSS) associated to the corresponding deformation mode<sup>1</sup>. VPSC90 is a newer implementation of the VPSC model proposed by Galan Lopez *et al.* [45]. In VPSC90, elasticity is introduced at the microscopic level adding an elastic strain term that is determined by the elastic stiffness  $C_{sc}$  given by the ELSC (Elastic Self-Consistent) method [35]. The addition of the elastic and plastic strain must be equal to the strain

<sup>1</sup> The term deformation mode refers here to the nomenclature used in VPSC input files to define sets of slip systems with common properties and it is not related with boundary conditions of the problem.

defined in the boundary conditions of the problem and thus the total strain during the increment,  $\Delta\varepsilon$ , is calculated by adding an elastic strain component to the permanent strain caused by the plastic strain rate  $\dot{\varepsilon}_g$ :

$$\Delta\varepsilon = \Delta\varepsilon_{el} + \Delta\varepsilon_{pl} = C_{sc}^{-1} \Delta\sigma + \dot{\varepsilon} \Delta t \quad [18]$$

Additionally, it is possible to impose that a stress component is zero, while the corresponding strain component is unknown.

The main novelty of VPSC90 is the usage of a faster algorithm, capable of finding a direct solution to grain stresses based on the Newton method such that, starting with a first approximation of grain stresses (usually assuming an elastic problem), the solution is improved using the equation:

$$\Delta\sigma_g = (M_g + \tilde{M}_g)^{-1} (X_g + (M + M_g)(C_{sc}^{-1} + \Delta t M)^{-1} X) \quad [19]$$

where  $X_g$  is the error in the interaction equation (14) of grain  $g$ , and  $X$  is the error in equation (18):

$$X_g = \dot{\varepsilon} - \dot{\varepsilon}_g + \tilde{M}_g(\sigma - \sigma_g) \quad [20]$$

$$X = \Delta\varepsilon - C_{sc}^{-1} \Delta\sigma - \dot{\varepsilon} \Delta t \quad [21]$$

Each application of (eq. 19) will reduce the errors  $X_g$  and  $X$  until the desired levels of tolerance are reached.

In the current study, the VPSC90 model has been modified with the addition of strain rate sensitivity and a physical hardening law based on the evolution of dislocations, as explained in the following sections.

### 3.7.2.2 Strain rate sensitivity

Expression (17) correlates stress and strain in the grain according to a viscoplastic behavior, such that grains subjected to lower stresses are deformed at lower speed than grains under higher loads. When the  $n_s$  value is high enough, Eq 17 approximates the Schmid law such that, when grains are deformed at rates lower than the defined  $\gamma_0$ , stresses in that grain will be negligible. When the deformation rate is

higher than  $\gamma_0$  a strain rate hardening effect will be observed. In [44], the strain rate sensitivity exponent  $n_s$  is used to account for the macroscopic strain hardening of the material. However, the exponent  $n_s$  will also affect the yielding behaviour of the material and, if it is used to account for the macroscopic effect of strain rate as in [46], the required value of  $n_s$  will make the tensile curves to exhibit a much sharper yielding than the one found in the studied materials. Therefore, a different approach is needed to include strain rate hardening in the model.

As shown in [46], strain rate sensitivity of steels is correctly captured by a multiplicative relationship as used in the Johnson-Cook (J-C) model:

$$\sigma(\dot{\varepsilon}) = \sigma_0(\dot{\varepsilon}_0) \left[ 1 + C_{JC} \ln\left(\frac{\dot{\varepsilon}}{\dot{\varepsilon}_0}\right) \right] \quad [22]$$

where  $C_{JC}$  is the strain rate sensitivity constant of the J-C model and  $\dot{\varepsilon}_0$  is a reference strain rate, for which quasi-static conditions can be assumed.

In order to use a multiplicative relationship for strain rate sensitivity as in (eq. 22), it is necessary to cancel the macroscopic effect of the strain rate sensitivity approach from Assaro and Needleman in (eq. 17), reformulated as:

$$\dot{\gamma} = \dot{\gamma}_0 \left(\frac{\tau}{\tau_c}\right)^n \Rightarrow \tau_c(\dot{\varepsilon}) = \left(\frac{\dot{\varepsilon}}{\dot{\gamma}_0}\right)^{\frac{1}{n}} \tau_c(\dot{\gamma}_0) = \left(\frac{\dot{\varepsilon}}{\dot{\varepsilon}_0}\right)^{\frac{1}{n}} \tau_c(\dot{\varepsilon}_0) \quad [23]$$

In order to cancel the Assaro and Needleman strain rate sensitivity approach; First, the calculated  $\tau_c$  will be multiplied by a factor equal to the effect of (eq. 23), and then it will be multiplied by the strain rate sensitivity factor given by (eq. 22), such that the final  $\tau_c$  value will be:

$$\tau_c(\dot{\varepsilon}) = \tau_c(\dot{\varepsilon}_0) \left[ 1 + C_{JC} \ln\left(\frac{\dot{\varepsilon}}{\dot{\varepsilon}_0}\right) \right] \left[ \frac{\dot{\varepsilon}}{\dot{\varepsilon}_0} \right]^{-1/n} \quad [24]$$

where  $\tau_c(\dot{\varepsilon}_0)$  is the CRSS at the reference strain rate  $\dot{\varepsilon}_0$ . The value of  $C_{JC}$  (eq. 13) can be approximated according to the yield stress for each phase at the reference strain rate as shown in Chapter 4 below.

### 3.7.2.3 Physical hardening model

The CRSS value in equation (17) is calculated as the addition of two terms: a static yield stress  $\tau_0$ , which is the same for all the slip systems of every grain of BCC phase, and a second term  $\tau_d^s(\rho_s)$ , which depends on dislocation density and, therefore, on the deformation history of each slip system and, by extension, of every grain.

The static yield stress term,  $\tau_0$  is also composed of several terms. It includes the hardening effect of the crystal lattice of the phase of the grain,  $\tau_l$  (which for pure iron has been measured as 77MPa [47]), the 8 elements in solid solution,  $\tau_{ss}$ , calculated on the basis of a phenomenological formula to correlate yield stress with chemical composition [47], and also the grain size, or the lath size for those phases in which the material presents a lath structure, calculated using a Hall-Petch like relationship [48].

$$\sigma_0 = \sigma_l + \sigma_{ss} + \sigma_d \quad [24]$$

with  $\sigma_l=77$  MPa

$$\sigma_{ss} = 37W_{Mn} + 678W_P + 60W_{Si} + 80W_{Cu} + 45W_{Ni} + 60W_{Cr} + 11W_{Mo} \quad [25]$$

$$\sigma_d = \begin{cases} K_{HP}/\sqrt{d} & \text{with } d \equiv \text{grain size} \\ K_{HP}M\mu b/d & \text{with } d \equiv \text{lath size} \end{cases} \quad [26]$$

where  $W_X$  is the weight percentage of the element  $X$ ,  $M$  is the Taylor factor,  $\mu$  is the elastic shear modulus (calculated as  $\sqrt{0.5 \cdot (C_{44}C_{11} - C_{12}^2)}$ , where  $C_{ij}$  is the element in row  $i$  and column  $j$  of  $C_{sc}$ ), and  $b$  is the cell size (0.287 $\mu\text{m}$  for Fe-alpha).

These phenomenological expressions have been developed to calculate the yield stress. In order to apply them to the CRSS in slip systems, it is necessary to multiply the obtained  $\sigma_y$  expression by a constant,  $C_1$ , which should be of the order of the typical Taylor factor in steels:

$$\tau_0 = \frac{(\sigma_0)}{C_1} \quad [27]$$

The hardening induced by dislocations is added to the static term given by equation (24) according to the expression of Taylor:

$$\tau_c = \tau_0 + \alpha \mu b \sqrt{\sum_{s'} a_{ss'} \rho_{s'}} \quad [28]$$

where  $\alpha$  depends on the structure of dislocations. The constants  $a_{ss'}$  account for the latent hardening effect (the hardening of system  $s'$  caused by dislocations of system  $s$ ) and are taken from [49]. The dislocation density  $\rho_s$  is calculated according to the following differential equation:

$$\frac{d\rho_s(\gamma_s)}{d\gamma_s} = \frac{1}{\bar{\lambda}b} - \frac{2y}{b} \rho_s(\gamma_s) + \frac{y\bar{\lambda}\pi}{2b^2} (C_2 + 2\sigma_{imb}^2 \gamma_s) \quad [29]$$

where each of the three summands in the right-side term account for dislocation storage, dynamic recovery, and evolution of the geometrically necessary dislocations (GNDs), respectively. In this expression,  $y$  is the annihilation distance,  $C_2$  and  $\sigma_{imb}^2$  are two constants related with the incidental necessary boundaries (INBs) and geometrically necessary boundaries (GNBs), respectively, and  $\bar{\lambda}$  is the mean free path, which is calculated according to the equation:

$$\frac{1}{\bar{\lambda}} = \frac{1}{d} + \frac{1}{\beta} \sqrt{\sum_s \rho_s} + \frac{c_p v_p}{d_p} \quad [30]$$

in which  $d$  is the maximum distance for dislocation movement (grain size or lath width),  $\beta$  depends on the structure of the dislocations (although it is different from  $\alpha$  in equation 28) and the last term accounts for the obstacles due to the presence of carbides according to Ashby [50];  $v_p$  and  $d_p$  are the volume fraction and size of the carbides, respectively, and  $c_p$  is a constant that depends on the shape of these carbides (*i.e.* being either spherical or cubic). In order to avoid different results depending on the step size, expression (29) is integrated with respect to  $\gamma$ . For simplicity, it is assumed that the mean free path  $\bar{\lambda}$  remains constant during the step. If eq. (29) is rewritten as:

$$\frac{d\rho_s(\gamma_s)}{d\gamma_s} = A + B\rho_s(\gamma_s) + C\gamma_s \quad [31]$$

then the dislocation value takes the form:

$$\rho_s(\gamma_s + \Delta\gamma_s) = \left( \rho_s(\gamma_s) + \frac{B}{A^2} + \frac{C}{A} \right) e^{A\Delta\gamma_s} - \frac{B}{A} \Delta\gamma_s - \frac{B}{A^2} - \frac{C}{A} \quad [32]$$

## References

- [1] J.G.S. David K. Matlock, Emmanuel De Moor, and Paul J. Gibbs, Recent developments in Advanced High Strength Sheet Steels for automotive applications-An Overview, JESTECH 15(1) (2012) 1-12.
- [2] O. Bouaziz, H. Zurob, M. Huang, Driving force and logic of development of advanced high strength steels for automotive applications, Steel Research International 84(10) (2013) 937-947.
- [3] C. Garcia-Mateo, F.G. Caballero, Ultra-high-strength bainitic steels, Isij Int 45(11) (2005) 1736-1740.
- [4] D. De Knijf, C. Fojer, L.A.I. Kestens, R. Petrov, Factors influencing the austenite stability during tensile testing of Quenching and Partitioning steel determined via in-situ Electron Backscatter Diffraction, Mat Sci Eng a-Struct 638 (2015) 219-227.
- [5] C.C. Tasan, J.P.M. Hoefnagels, M. Diehl, D. Yan, F. Roters, D. Raabe, Strain localization and damage in dual phase steels investigated by coupled in-situ deformation experiments and crystal plasticity simulations, Int J Plasticity 63 (2014) 198-210.
- [6] N. Fujita, N. Ishikawa, F. Roters, C.C. Tasan, D. Raabe, Experimental-numerical study on strain and stress partitioning in bainitic steels with martensite-austenite constituents, Int J Plasticity 104 (2018) 39-53.
- [7] C. Garcia-Mateo, F.G. Caballero, H.K.D.H. Bhadeshia, Acceleration of low-temperature bainite, Isij Int 43(11) (2003) 1821-1825.
- [8] W. Bleck, K. Phiu-On, Microalloying of cold-formable multi phase steel grades, Microalloying for New Steel Processes and Applications 500-501 (2005) 97-112.
- [9] H. Bhadeshia, Bainite in steels: transformation, microstructure and properties, IOM Communications Ltd, London2001.
- [10] H.K.D.H. Bhadeshia, D.V. Edmonds, Bainite in Silicon Steels - New Composition Property Approach .1., Met Sci 17(9) (1983) 411-419.
- [11] G. Krauss, Solidification, Segregation, and Banding in Carbon and Alloy Steels, Metall Mater Trans B 34(6) (2003) 781-792.
- [12] A.P.C.a.J.W.M. Y. J. Park, Effect of martensite bands and elongated manganese sulphide inclusions on the formability of dual-phase steels, 110th AIME annual meeting, Proceedings of the symposium "Fundamentals of Dual Phase steels", Chicago, IL, USA, 1981, pp. 485-497.
- [13] H.T. Andersson J.O., Höglund L., Shi P.F., and Sundman B., Thermo-Calc and DICTRA, 26 (2002) 273-312.
- [14] J.C.H.a.V.L. B. Donnay, Microstructure evolution of C-Mn steels in the hot deformation process: The STRIPCAM model, 2nd Int Conf Model Met Roll Process, 1996, pp. 23-35.
- [15] S.V. GALLEZ C, MAIER M, VAN HAAFTEN W, PARKER S, PERLADE A, et al, Online prediction of the mechanical properties of hot rolled strips. 2006).
- [16] S.M.C. van Bohemen, The nonlinear lattice expansion of iron alloys in the range 100-1600 K, Scripta Materialia 69(4) (2013) 315-318.
- [17] A.S. E6-03, Standard Terminology Relating to Methods of Mechanical Testing, ASTM international, 2003.
- [18] P. Verleysen, J. Degrieck, Measurement of the evolution of the axial strain distribution in Hopkinson specimens, J Phys Iv 110 (2003) 501-506.
- [19] J.G. Lopez, Crystal plasticity based modelling of the strain rate dependent mechanical behaviour of Ti-6Al-4V, Ingenieurswetenschappen en Architectuur, Ghent university, Ghent, 2013 - 2014.
- [20] H. Kolsky, An Investigation of the Mechanical Properties of Materials at very High Rates of Loading, Proceedings of the Physical Society. Section B 62(11) (1949) 676.
- [21] P. Verleysen, J. Degrieck, Experimental and numerical study of the response of steel sheet Hopkinson specimens, J Phys Iv 134 (2006) 541-546.
- [22] J.D. Patricia Verleysen, Tom Verstraete and Joost Van Slycken Influence of specimen geometry on split Hopkinson tensile bar tests on sheet materials, Exp Mech 48(5) (2008) 587 - 598.
- [23] O. Leon-Garcia, Micromechanisms of Failure under Static Loading in Sheet Metals for Automotive Applications, Technische Univeriteit Delft, Delft, 2013.
- [24] ASTM, Standard Test Methods for Determining Average Grain Size, ASTM E112-96(2004), ASTM International, West Conshohocken, PA, 2004.
- [25] C.C. Tasan, M. Diehl, D. Yan, C. Zambaldi, P. Shanthraj, F. Roters, D. Raabe, Integrated experimental-simulation analysis of stress and strain partitioning in multiphase alloys, Acta Mater 81 (2014) 386-400.
- [26] S.H. Choi, E.Y. Kim, W. Woo, S.H. Han, J.H. Kwak, The effect of crystallographic orientation on the micromechanical deformation and failure behaviors of DP980 steel during uniaxial tension, Int J Plasticity 45 (2013) 85-102.
- [27] J.T. Armstrong, Quantitative Elemental Analysis of Individual Microparticles with Electron-Beam Instruments, Electron Probe Quantitation (1991) 261-315.
- [28] A.J. Schwartz, M. Kumar, B.L. Adams, D.P. Field, Electron Backscatter Diffraction in Materials Science, Springer US2009.
- [29] F. Archie, X.L. Li, S. Zaeferrer, Micro-damage initiation in ferrite-martensite DP microstructures: A statistical characterization of crystallographic and chemical parameters, Mat Sci Eng a-Struct 701 (2017) 302-313.

---

- [30] R.H.a.H.S. F. Bachmann, Texture Analysis with MTEX – Free and Open Source Software Toolbox Solid State Phenomena 160 (2010) 63-68.
- [31] C.C. Tasan, J.P.M. Hoefnagels, M.G.D. Geers, Identification of the continuum damage parameter: An experimental challenge in modeling damage evolution, *Acta Mater* 60(8) (2012) 3581-3589.
- [32] Q. Lai, O. Bouaziz, M. Goune, L. Brassart, M. Verdier, G. Parry, A. Perlade, Y. Brechet, T. Pardoen, Damage and fracture of dual-phase steels: Influence of martensite volume fraction, *Mat Sci Eng a-Struct* 646 (2015) 322-331.
- [33] C. Landron, E. Maire, J. Adrien, O. Bouaziz, M. Di Michiel, P. Cloetens, H. Suhonen, Resolution effect on the study of ductile damage using synchrotron X-ray tomography, *Nucl Instrum Meth B* 284 (2012) 15-18.
- [34] C. Landron, E. Maire, O. Bouaziz, J. Adrien, L. Lecarme, A. Bareggi, Validation of void growth models using X-ray microtomography characterization of damage in dual phase steels, *Acta Mater* 59(20) (2011) 7564-7573.
- [35] R.A. Lebensohn, C.N. Tomé, A Self-Consistent Anisotropic Approach for the Simulation of Plastic-Deformation and Texture Development of Polycrystals - Application to Zirconium Alloys, *Acta Metallurgica Et Materialia* 41(9) (1993) 2611-2624.
- [36] G.R.a.C. Johnson, W.H., A Constitutive Model and Data for Metals Subjected to Large Strains, High Strain Rates, and High Temperatures., *Proceedings 7th International Symposium on Ballistics*, The Hague (1983) 541-547.
- [37] T. Rahmaan, A. Bardelcik, J. Imbert, C. Butcher, M.J. Worswick, Effect of strain rate on flow stress and anisotropy of DP600, TRIP780, and AA5182-O sheet metal alloys, *International Journal of Impact Engineering* 88 (2016) 72-90.
- [38] R.C. Picu, A. Majorell, Mechanical behavior of Ti-6Al-4V at high and moderate temperatures - Part II: constitutive modeling, *Mat Sci Eng a-Struct* 326(2) (2002) 306-316.
- [39] P. Verleysen, J. Peirs, J. Van Slycken, K. Faes, L. Duchene, Effect of strain rate on the forming behaviour of sheet metals, *Materials Processing Technology* 211(8) (2011) 1457-1464.
- [40] J. Peirs, P. Verleysen, W. Van Paepegem, J. Degrieck, Determining the stress-strain behaviour at large strains from high strain rate tensile and shear experiments, *International Journal of Impact Engineering* 38(5) (2011) 406-415.
- [41] G. Sachs, Plasticity problems in metals., *T Faraday Soc* 24 (1928) 0084-0091.
- [42] G.I. Taylor, Plastic strain in metals., *J I Met* 62 (1938) 307-324.
- [43] J.D. Eshelby, The Determination of the Elastic Field of an Ellipsoidal Inclusion, and Related Problems, *Proc R Soc Lon Ser-A* 241(1226) (1957) 376-396.
- [44] R.J. Asaro, A. Needleman, Overview .42. Texture Development and Strain-Hardening in Rate Dependent Polycrystals, *Acta Metall Mater* 33(6) (1985) 923-953.
- [45] J. Galan, P. Verleysen, R.A. Lebensohn, An improved algorithm for the polycrystal viscoplastic self-consistent model and its integration with implicit finite element schemes, *Model Simul Mater Sc* 22(5) (2014).
- [46] J. Galan-Lopez, P. Verleysen, Simulation of the plastic response of Ti-6Al-4V thin sheet under different loading conditions using the viscoplastic self-consistent model, *Mat Sci Eng a-Struct* 712 (2018) 1-11.
- [47] P. Gutierrez, Parker, Bianchi, Mesplont, Kawalla, Mechanical property models for high-strength complex microstructures.
- [48] K.Y. Zhu, O. Bouaziz, C. Oberbillig, M.X. Huang, An approach to define the effective lath size controlling yield strength of bainite, *Mat Sci Eng a-Struct* 527(24-25) (2010) 6614-6619.
- [49] P. Franciosi, Glide Mechanisms in Bcc Crystals - an Investigation of the Case of Alpha-Iron through Multislip and Latent Hardening Tests, *Acta Metall Mater* 31(9) (1983) 1331-1342.
- [50] M.F. Ashby, The deformation of plastically non-homogeneous materials, *Philos Mag* 21(170) (1970) 399-424.

# Chapter 4 Strain rate dependent dynamic mechanical response of bainitic multiphase steels

**Abstract.** This chapter evaluates the quasi-static and dynamic mechanical response of the two grades of bainitic steels introduced earlier in chapter 3 section 3.1.5. Microstructures are studied by advanced characterization techniques, including X-ray diffraction and scanning electron microscope equipped with an electron backscatter diffraction detector. Subsequently, the quasi-static and dynamic mechanical response of the steels are correlated to microstructural parameters. A positive effect of the strain rate is observed for all the examined materials: when the strain rate is increased, both the tensile stress and deformation levels increase, thus also the energy absorption capacity. However, it is shown that the higher the fraction of second phase constituents, the lower the effect of strain rate becomes. In addition, the grain size also directly correlates to the strain rate effect too. The phenomenological hardening model of Johnson-Cook is used to simulate the quasi-static and dynamic flow behaviors, allowing to quantify the strain rate sensitivity for each material. A comprehensive literature survey on the strain rate sensitivity of various steel grades reveals that steels with higher strength demonstrate a lower strain rate sensitivity factor. This trend can be approximated by a power law function which clearly is followed by the materials under consideration in this study.

**Keywords:** Advanced high strength steels; Bainite; Microstructure; Hopkinson tensile bar; Strain rate sensitivity; Constitutive modelling.

*Reproduced from:*

*Shakerifard. B, Lopez. J. G, Taboada Legaza. M. C, Verleysen. P, Kestens. L. A. I. Strain rate dependant dynamic mechanical response of bainitic multiphase steels. Materials Science and Engineering A, 2019, 745, 279-290, doi: 10.1016/j.msea.2018.12.105.*

## 4.1 Introduction

In chapter 2 section 2.2, the importance and application of the high strain rate deformation in car crash events and forming processes were discussed in details. Figure 4-1 shows a literature survey on strain rate sensitivity factors of various conventional and AHS steel grades versus initial yield stress, denoted as A. The strain rate sensitivity factor in figure 4-1 is the one used in the Johnson-Cook hardening model [1]. The plotted values are either found in literature or calculated based on dynamic flow curves [2-4, 5-8, 9-13]. It appears that steels with higher yield stresses demonstrate lower strain rate sensitivity factors.

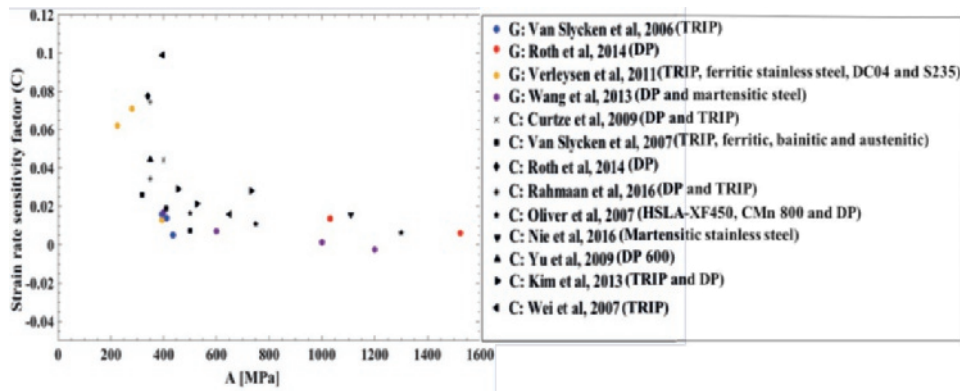


Figure 4-1. Strain rate sensitivity factor as a function of initial yield stress, i.e. A parameter of J-C model. C and G in the legend indicate whether the strain rate sensitivity was calculated or given respectively.

Despite a large number of reports on the dynamic response of the first generation of AHSSs, only few studies have been conducted on the strain rate response of bainitic multiphase steel grades [14], known as the third generation of AHSSs. Moreover, studying the strain rate sensitivity of bainitic steel grades can confirm whether or not the trend observed in figure 4-1 is valid for these steels. In the current study, high strain rate uniaxial tension tests are conducted on two different grades of bainitic steels (section 4.2.2). Aiming at different fractions of second phase constituents, three different thermal treatments were imposed on each grade. Therefore, in total 6 different bainitic microstructures are considered (see section 3.1.5). The microstructures of the bainitic steels are investigated in section 4.2.1 by advanced characterization techniques, i.e. by X-ray Diffraction (XRD) and Scanning Electron Microscope (SEM) equipped with an Electron Backscatter Diffraction (EBSD) detector in order to record orientation contrast images of the bainitic microstructures annealed under various conditions. Additionally, the

correlation between microstructures and the dynamic mechanical properties are studied. Static and dynamic flow curves are used in order to model the strain rate and temperature dependent constitutive behavior of the investigated steel alloys. The phenomenological model of Johnson-Cook (J-C) is used to this purpose [1]. The J-C model offers the advantage that the flow behavior of a wide range of materials can be predicted with very few material parameters [2, 12, 15].

## 4.2 Results

### 4.2.1 Microstructure characterization

The microstructures of the LoSi samples are shown in figure 4-2. The HT and LT samples reveal a bainitic matrix in which small carbides are observed. Isolated MA islands are also observed within the bainitic matrix in figure 4-2(a and b). In the LB, almost no second phase constituents were detected except carbides and thus the microstructure shows a fully bainitic microstructure, see fig 4-2(c and c2). The Image Quality (IQ) overlaid with the phase map of the LB sample shown in Figure 4-2(c2) also reveals an acicular grain shape, while the HT and LT samples have more equi-axed grains, see fig4-2(a2 and b2). EBSD analysis does not reveal any RA phase in the microstructure of any of the LoSi samples, cf. figure 4-2(a2, b2 and c2). XRD analysis also shows a negligible fraction of RA in LoSi grade (<0.5%). Therefore, the MA islands in the LoSi grade are assumed to be fully martensitic regions.

The microstructures of the high Si grade samples are shown in figure 4-3. The SEM micrographs of all samples reveal a similar bainitic matrix with MA islands, retained austenite and no carbides in the microstructures, due to the presence of silicon [16]. Thin films of retained austenite are observed in the HT and SB samples, cf. fig 4-3a and c. The corresponding IQ maps overlaid with phase maps of the samples, cf. fig. 4-3a2, b2 and c2, show the presence of RA and martensite phase in all samples. Qualitatively, it is seen that the SB sample has the higher martensite fraction, compared to the HT and LT samples. Moreover, the SB sample exhibits more lath like and/or acicular matrix compared to the HT and LT samples with equi-axed grains. Tables 4-1 and 4-2 quantitatively illustrate the microstructural variations of all samples in both high and low Si grades.

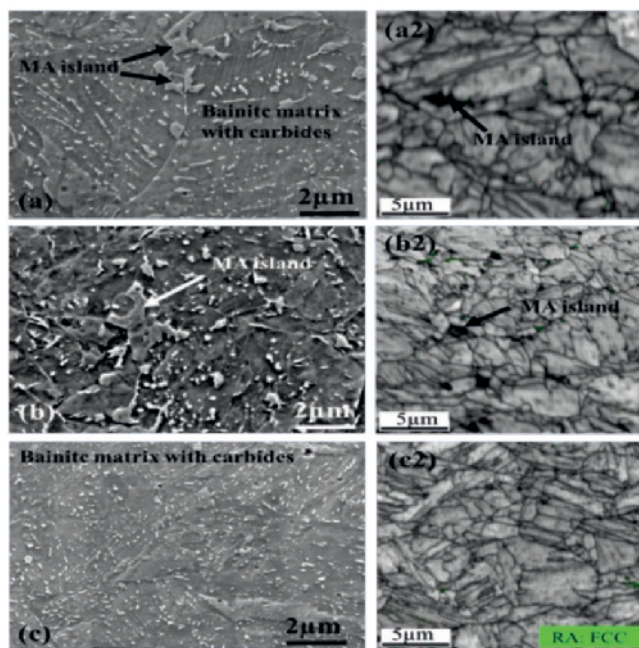


Figure 4-2. SEM micrographs (left) and IQ+phase maps (right) of the microstructures of the LoSi grade: (a and a2) HT sample, (b and b2) LT sample and (c and c2) LB sample. Dark regions, i.e. low IQ regions, of EBSD maps correspond to martensitic regions.

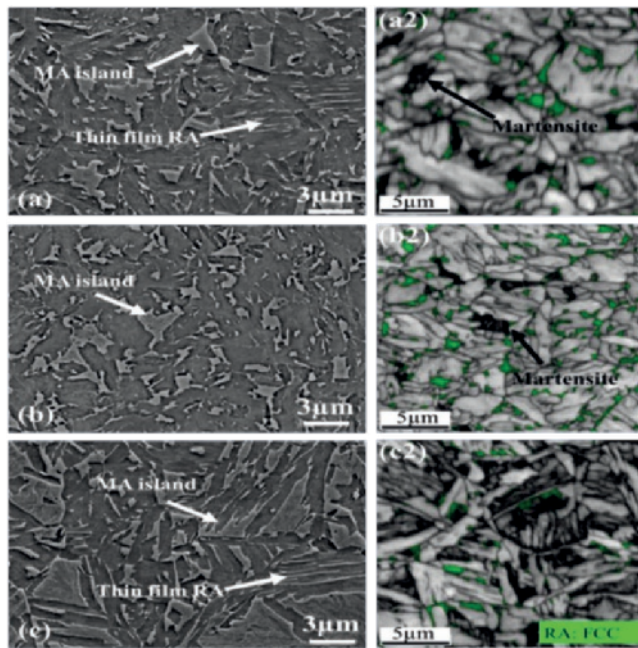


Figure 4-3. SEM micrographs (left) and IQ+phase maps (right) of the microstructures of the HiSi grade; (a and a2) HT sample, (b and b2) LT sample and (c and c2) SB sample. Dark regions of EBSD maps correspond to martensitic regions.

The grain size listed in table 4-1 shows that the HT sample has the coarsest microstructure due to the higher austenization temperature, which results in a coarser prior austenite grain size. This leads to lower kinetics and/or nucleation rate during the bainite transformation, producing a coarser final microstructure in the HT sample. Nevertheless, in the LB sample, with the decreased bainite holding temperature of 390°C with respect to the HT and LT sample, the driving force for nucleation is higher. Therefore, the final microstructure is the finest among the LoSi samples. The total fraction of martensite in the HT and LT sample is approximately equal, while the LB sample only contains carbides as second phase constituents.

A similar effect of austenization temperature is observed in the HiSi grade on the differentiation of the bainite grain size among the HT and LT samples, as shown in table 4-2. In the SB sample, the short bainite holding time of 14 s resulted in a finer bainite due to the limited time for the growth process. In addition, the highest fraction of second phase constituents is seen in this sample due to the incomplete bainite transformation. The variation of RA measured by XRD reveals that the LT sample has the highest RA fraction at room temperature, cf. table 4-2.

Table 4-1. Microstructural variables of LoSi samples.

Sample	Phase	Grain size (μm)	Fraction (%)	Block size (μm)	Cementite size (μm)
HT	Bainite	1.44±0.01	Bal	-	-
	MA	-	3.4±1.7	0.7±0.35	-
	Cementite	-	3.6 ± 1.0	-	0.07 ± 0.04
	ATM <sup>2</sup>	0.5 ± 0.1	4.8 ± 1.8	-	-
LT	Bainite	1.17 ± 0.03	Bal	-	-
	MA	-	2.4 ± 0.7	0.6±0.24	-
	Cementite	-	3.1 ± 0.7	-	0.07 ± 0.04
	ATM	0.47 ± 0.2	6.2 ± 2.3	-	-
LB	Bainite	1.08 ± 0.02	Bal	-	-
	MA	-	0	-	-
	Cementite	-	4.5 ± 0.4	-	0.06 ± 0.03
	ATM	-	0	-	-

Table 4-2. Microstructural variables of HiSi samples.

Sample	Phase	grain size (μm)	Fraction (%)	Block size (μm)
HT	Bainite	1.43±0.08	Bal	-
	Martensite	-	8.5± 1.5	0.5±0.8
	RA	-	12.2	0.42
	ATM	-	0	-
LT	Bainite	1.34 ± 0.2	Bal	-
	Martensite	-	5.4 ± 2.3	0.4±0.8
	RA	-	14.5	0.37
	ATM	-	0	-
SB	Bainite	0.95 ± 0.15	Bal	-
	Martensite	-	13.4 ± 2.5	0.6 ± 0.2
	RA	-	5.8	0.22
	ATM	-	19.0 ± 2.7	1.7 ± 0.2

#### 4.2.2 Mechanical response

The quasi-static and dynamic mechanical response of all samples is shown in figure 4-4. For each test condition a representative curve is chosen. When the quasi-static tests are compared with the high strain rate tests, a positive effect of the strain rate is clear for all the

<sup>2</sup> ATM phase was exposed by Nital etchant and quantified by the subtraction of whole martensitic region measured by EBSD from MA regions.

steels. However, no clear effect of strain rate is observed within the high strain rate regime. The work hardening of all materials under high strain rate deformations differs from the quasi-static behavior. Related to this, the dynamic curves reveal a delayed necking phenomenon compared to the corresponding quasi-static curves, i.e. they exhibit an increased uniform elongation.

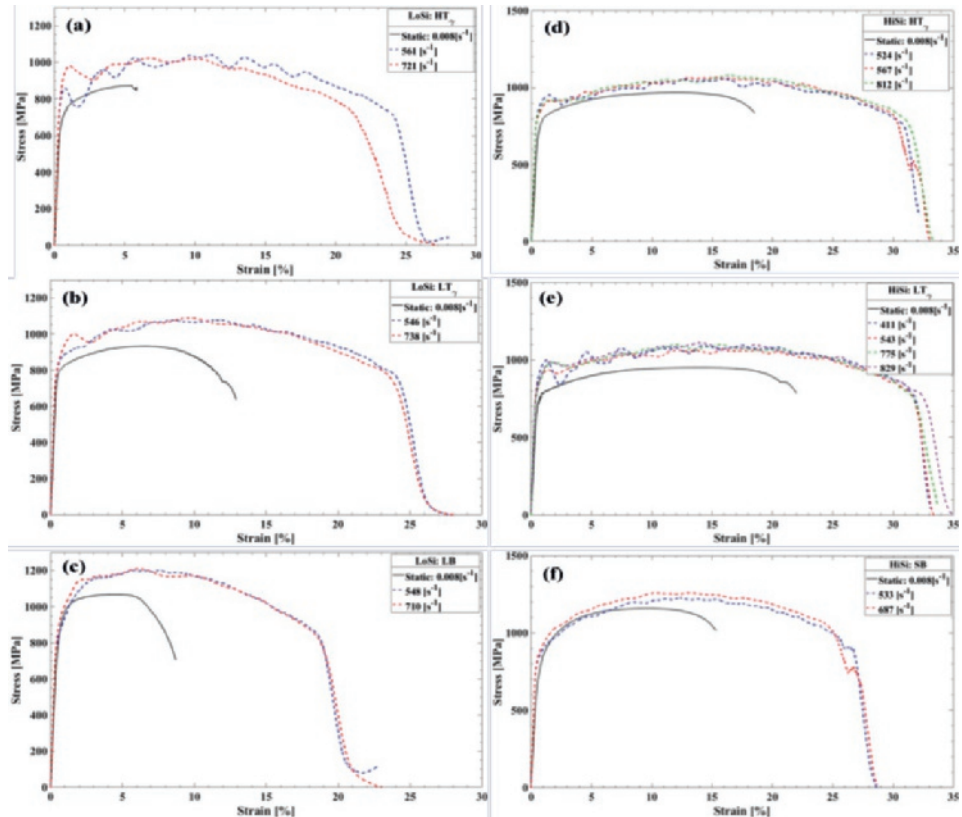


Figure 4-4. Engineering flow curves of all sample from both grades: (a, b and c) the flow curves of the HT, LT and LB samples from LoSi grade and (d, e and f) the flow curves of the HT, LT and SB samples from HiSi grade. The dashed curves are the high strain rate tests.

Figure 4-5 shows the effect of strain rate on the ultimate tensile strength (UTS) in both grades. In the LoSi grade, the strengthening phenomenon is seen from the quasi-static to the dynamic loading regime. However, increasing the strain rate under dynamic loading conditions does not result in higher tensile strength values, see fig. 4-5a. In the HiSi grade, besides a significantly improved tensile strength when

changing from quasi-static to dynamic loading, increasing the strain rate under dynamic loading from  $\sim 500 \text{ s}^{-1}$  to more than  $\sim 700 \text{ s}^{-1}$  only results in a slight increase of the UTS.

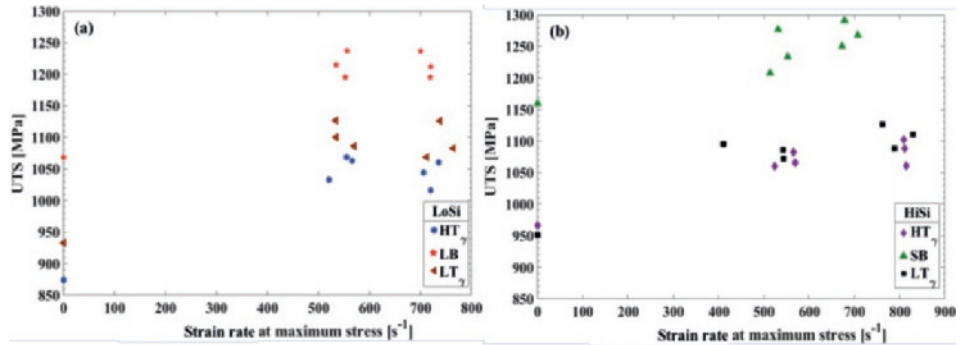


Figure 4-5. Ultimate tensile strength as a function of strain rates; (a) LoSi samples and (b) HiSi samples.

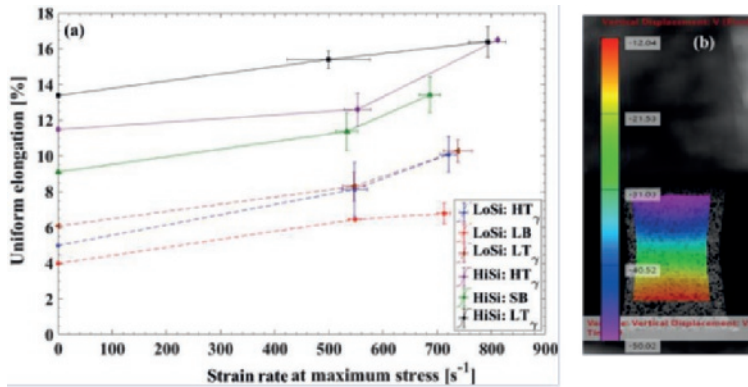


Figure 4-6. DIC analysis; (a) uniform elongation as a function of strain rates and (b) displacement used as a virtual extensometer for the calculation of engineering strain.

The uniform elongation of the samples at various strain rates is calculated and plotted in figure 4-6. For the SHTB tests, the uniform strain is obtained by combining the DIC local strain analysis and the average strains obtained using the split Hopkinson bar equation. All samples reveal an improvement of the uniform elongation at high strain rates. It is seen that the HiSi samples demonstrate higher uniform elongations compared to the LoSi samples.

Figures 4-7a and b depict the energy absorption of both grades at a tensile strain of 5% and at UTS, calculated by integration of the stress-strain curves (figure 4-4). It is observed that at 5% of deformation,

the absorbed energy increases from the static to the dynamic tests for all materials. However, this increase is not pronounced, as it is restricted to a narrow range between from  $38$  to  $48 \cdot 10^6 \text{ Jm}^{-3}$  under static loading conditions and from  $40$  to  $53 \cdot 10^6 \text{ Jm}^{-3}$  under dynamic loading conditions. Figure 4-7b shows the energy absorption at the UTS point. As opposed to the small difference of the energy absorption at 5% of deformation between the static and dynamic loading conditions, the difference at the UTS point is significant. The HiSi grade shows a higher energy absorption potential compared to the LoSi grade, cf. Figure 4-7b. In the LoSi grade, it is observed that the energy absorption of both the HT and LT samples increases with 130 and 73%, respectively, when the strain rate increases from  $0.008$  to more than  $700 \text{ s}^{-1}$ , whereas the energy absorption of the LB sample increases with 62%. Besides, it is seen that with increasing the strain rate from  $550$  to  $700 \text{ s}^{-1}$ , the LB sample does not show a substantial difference in energy absorption. In the HiSi grade, the HT, LT and SB samples exhibit higher energy absorptions of 54, 35 and 40%, respectively, when the strain rate is increased from  $0.008$  to around  $700 \text{ s}^{-1}$  and above.

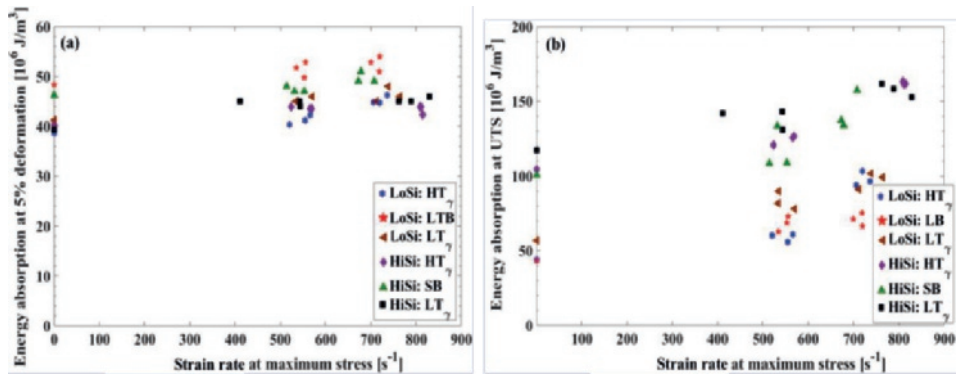


Figure 4-7. Energy absorption of both HiSi and LoSi grades (a) at 5% of deformation and (b) at the UTS point.

### 4.2.3 Flow behavior modelling

The experimental flow curves in section 4.2.2 are used in order to model the materials hardening behavior and to predict their strain rate sensitivity. To this purpose, the Johnson-Cook hardening model [1] is used. The J-C expression was shown in equation (13) of chapter 3.

Due to the high speed of deformation during SHTB tests, the heat developed in the sample during plastic deformation is not dissipated to the environment. The deformation process is adiabatic and the temperature rise can be calculated by the following equation:

$$\Delta T = \frac{\beta}{\rho c} \int \sigma d\varepsilon_P$$

where  $\rho$  is the mass density,  $c$  is the specific heat [J/kgK] and  $\beta$  is the Taylor-Quinney coefficient indicating the amount of plastic work converted to heat. For steel, the  $\beta$  value is often assumed to have a value between 0.9 and 1 [17]. In this study, for the LoSi samples, a  $\beta$  value of 0.9 is assumed. To account for the additional heat generated by the exothermal austenite to martensite transformation, the  $\beta$  value for the HiSi samples, comprising RA, is considered to be 0.95 [18]. Using eq. (1), the maximum adiabatic temperature rise is estimated to be 103°C at failure in the test carried out at a strain rate of 829 s<sup>-1</sup> with the LT sample of the HiSi grade, with the highest fraction of RA. The temperature increase in the dynamic tests at UTS varies from a minimum value of 38°C for the LoSi HT sample to a maximum of 60°C for the HiSi HT samples. Since, it has been shown by Bouquerel *et al.* [18] that the influence of temperature on flow behavior of steels below 100°C is negligible, the temperature softening term in the Johnson-Cook hardening models is ignored.

In table 4-3, the material parameters best fitting the Johnson-Cook model ( $A$ ,  $B$ ,  $n$ ,  $C$ ) are listed. The  $A$ ,  $B$  and  $n$  parameters are calculated from static curves, while  $C$  is calculated based on the high strain rate tensile tests. The parameters are calculated by the least square method and the R-square values in table 4-3 correspond to the dynamic curves. Figure 4-8 shows the experimental and simulated true stress curves of all the materials for both high and low silicon grades.

Table 4-3. Materials parameters used for the Johnson-Cook model.

Grade	Material	A [MPa]	B [MPa]	$n$	$C$	$R^2$	T (°C) <sup>3</sup>
LoSi	HT	743	2750	0.87	0.014	0.751	45
	LT	817	2023	0.83	0.009	0.926	44
	LB	950	1818	0.71	0.007	0.819	38
HiSi	HT	782	1397	0.67	0.006	0.976	60
	LT	786	1560	0.76	0.012	0.932	60
	SB	817	2118	0.59	0.003	0.963	58

<sup>3</sup> Maximum temperature obtained at UTS for the test carried out at the highest strain rate calculated from the equation 2.

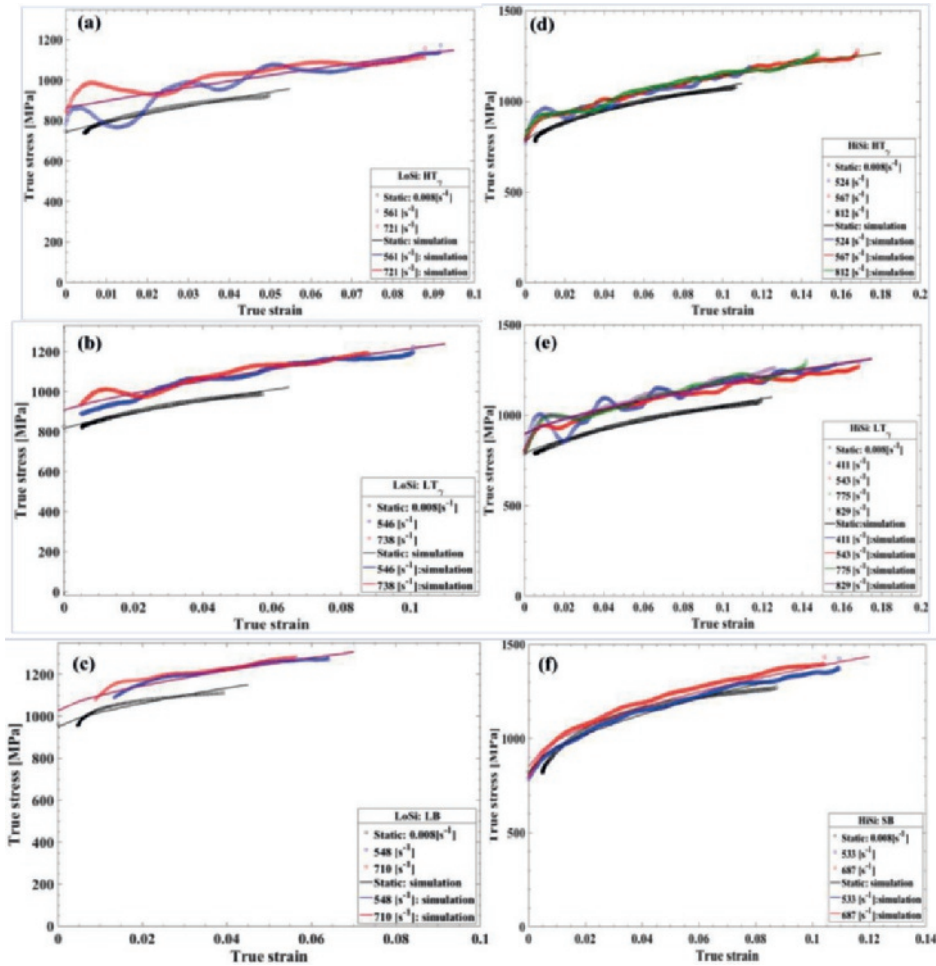


Figure 4-8. Experimental and simulated static and dynamic tensile curves for all the materials: (a, b and c) flow curves of the LoSi grade and (d, e and f) flow curves of the HiSi grade.

## 4.3 Discussion

Figure 4-9 demonstrates the correlation of the  $A$  and  $C$  parameters of the J-C model depicted earlier in figure 1. All data points in figure 4-9 are identical as in figure 4-1 except for the green points, which are the  $C$  factors from the current study, see Table 4-3. The steels studied in the current work completely follow the empirically observed correlation between yield strength and strain rate sensitivity

demonstrated in figure 4-1. It is shown that bainitic multiphase steels (green data points), as a 3<sup>rd</sup> generation of AHSSs, fill the strength gap between either conventional steels or 1<sup>st</sup> generation AHSSs, and fully martensitic steels or other steel grades with a strength higher than ~1000 MPa. It is apparent that steels with a higher strength reveal lower strain rate sensitivity, whereby the trend can be fitted with a power law. Although, the trend is just a rough approximation, it demonstrates that microstructural strengthening mechanisms can potentially decrease the strain rate sensitivity of steels. The data points of figure 4-9 show considerable scatter, particularly in the low-strength domain. This may be attributed to the fact that the steels in this region show large differences in microstructure and complexity. The diversity in steel grades in terms of composition and microstructural variables (i.e. grain size, dislocation density, phases and their corresponding topology) may have a different impact on the reduction of the strain rate sensitivity.

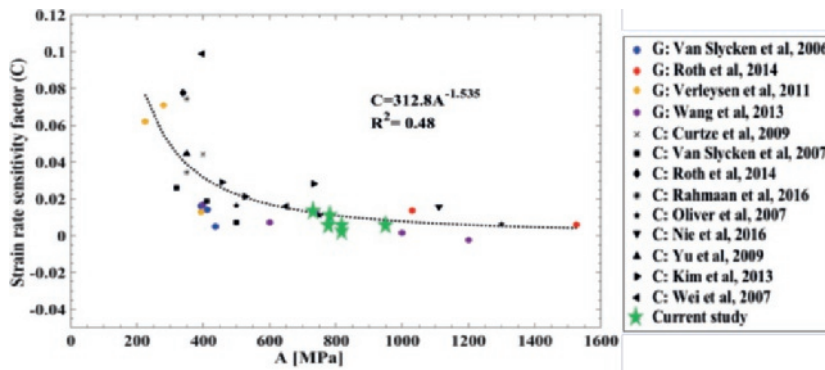


Figure 4-9. Strain rate sensitivity factor as a function of initial yield stress, i.e. A. A parameter of J-C model. C and G in the legend indicate whether the strain rate sensitivity was calculated or given, respectively. The green points are the C factors of the current studied materials.

The quasi-static mechanical response of the LoSi grade materials demonstrates a different flow behaviors (fig. 4-4). In the LB sample an enhanced strengthening mechanical response is observed compared to the HT and LT samples. This is due to the acicular finer microstructure and possibly a higher dislocation density in this particular steel due to a lower isothermal bainite transformation temperature (390°C) compared to the more equiaxed and coarser bainitic grains of the HT and LT samples (fig. 4-13a). This phenomenon has been reported by Garcia-Mateo *et al*, who also observed a continuous yielding in their bainitic steels due to the presence of mobile dislocations [19, 20]. However, this higher strength comes at the expense of the ductility in the LB sample, as shown in figure 4-6. The LT sample reveals improved strengthening compared to the HT sample while its uniform elongation is

also higher. The finer microstructure and a more dispersed distribution of the second phase MA islands result in improved strength and ductility properties. The micro-mechanical behavior of these two particular materials is discussed in detail elsewhere by Shakerifard *et al.* [21]. Tasan *et al.* also investigated the effect of the second phase topology, i.e. size, shape and distribution, on the improvement of strain distribution homogeneity on the micro-scale, which can potentially enhance the ductility of multiphase steels [22].

In the HiSi grade steels, the SB sample shows a different quasi-static flow response in which a more continuous yielding, and higher yield and tensile stresses are observed compared to the HT and LT samples (fig. 4-4). However, the SB sample has the lowest uniform elongation among the HiSi grade samples (fig. 4-6). The microstructure characterization of the SB sample explains the observed mechanical response. Indeed, the SB steel has the finest microstructure, the highest fraction of martensite and the lowest fraction of RA, thus, these all lead to an increase of strength in this sample. Comparing the HT and LT samples reveals that the higher RA in the LT sample results in a higher uniform elongation (see fig. 4-6), while its lower fraction of martensite has led to a slight decrease in UTS, as depicted in figure 4-5(b). The overall influence of martensite and retained austenite on strength and ductility of the HT, LT and SB samples of the HiSi grade is shown in figure 4-10.

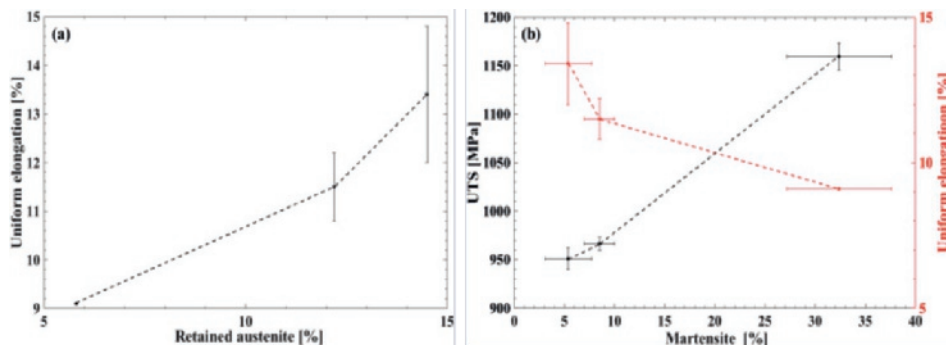


Figure 4-10. The effect of retained austenite and martensite (M blocks+ATM) on UTS and uniform elongation of the HiSi grade samples: (a) influence of retained austenite on the uniform elongation and (b) influence of martensite on UTS and uniform elongation.

The work hardening of all samples from quasi-static to dynamic loading conditions demonstrates a different trend. At high strain rates, the strain hardening continues until relatively higher strain levels compared to the corresponding quasi-static curves. The high strain rate mechanical response of all the samples from both grades reveals enhanced tensile properties in which tensile strength and uniform elongations have improved (see fig. 4-5 and 4-6). The increased flow stress at high strain rates may be

attributed to the reduced time for dislocations to overcome short-range dislocation barriers [23, 24]. In the LoSi grade, samples with a higher tensile strength at a quasi-static strain rate of  $0.008\text{ s}^{-1}$  reveal also a higher tensile strength at high strain rates (see fig. 4-5a). However, this trend is not observed for all steel samples in the HiSi grade (see fig. 4-5b). It is observed that at high strain rates the HT sample, with a higher fraction of martensite compared to the LT sample, shows a slightly lower tensile strength. Martensite softening due to the adiabatic temperature rise, which can cause a tempering and/or recovery process in the hard phase, may be at the origin of this observation. This mechanism has been addressed by Gronostajski *et al.* [25]. Therefore, the HT sample with the higher fraction of the martensite phase, while having less RA compared to the LT sample, can potentially experience more softening.

The uniform elongation under high strain rate deformations increases, as shown in figure 4-6. The delay of strain-induced austenite to martensite phase transformation at high strain rates can be an explanation for the observed trend in the HiSi grade samples. This event can be caused by various mechanisms such as strain induced twinning [14] and stabilization of retained austenite at higher temperatures due to the adiabatic heating, as reported by Choi *et al.* [26]. Therefore, the delay of the TRIP effect can enhance the plasticity accommodated by the microstructure through the stabilization of RA at relatively higher strain levels. Nevertheless, the softening process due to the adiabatic temperature rise within martensite is another parallel mechanism, which can enhance the ductility. It is observed that among the samples in the HiSi grade, the SB and HT samples with the higher fraction of M compared to the LT sample show a sudden increase in their uniform elongation from strain rates of approximately  $530$  and  $550\text{ s}^{-1}$  to higher strain rates. This can be related to the softening of the M phase at higher strain rates, owing to the temperature increase induced by adiabatic heating. A similar behavior is observed in the LoSi grade in the HT and LT samples compared to the LB sample with fully bainitic microstructure.

The energy absorption demonstrated in figure 4-7 shows a higher capacity in the HiSi grade compared to the LoSi grade. At 5% of deformation under high strain rates, see fig. 4-7a, the energy absorption is approximately similar within the range of  $40$  to  $50\cdot10^6\text{ J m}^{-3}$  in both grades and does not remarkably change from quasi-static to dynamic loading condition. Obviously, the LB sample, which has the highest flow stress, also reveals the highest energy absorption at 5% of deformation. The energy absorption at the UTS point shows the effect of the RA on the enhancement of energy absorption in the HiSi grade by accommodating higher uniform elongation compared to the LoSi grade. Although the HiSi-SB sample reaches the highest UTS value (fig. 4-5b), it has the lowest energy absorption among the HiSi grade samples. This is due to the fact that the LT and HT samples in the HiSi grade have a higher uniform elongation (fig. 4-6) because of the higher fraction of RA compared to the SB sample.

Figure 4-8 shows J-C simulated true stress-strain curves. For each material one set of parameters (see table 4-3) is able to describe their behavior at both low and high strain rates. Indeed, the simulated curves under both quasi-static and dynamic loading conditions are in good agreement with experimental curves.

Figure 4-11 shows the ratio of the true stresses in the high strain rate tests to the quasi-static true stress as a function of the normalized natural logarithmic strain rate for the different materials. The linear fit of these points indicates the strain rate sensitivity factor of the J-C model, which varies from the lowest value of 0.003 in the HiSi grade to the highest value of 0.013 in the LoSi grade. Strain rate sensitivity factors obtained from the J-C model fitting, see table 4-3, are in good agreement with the slope values in figure 4-11.

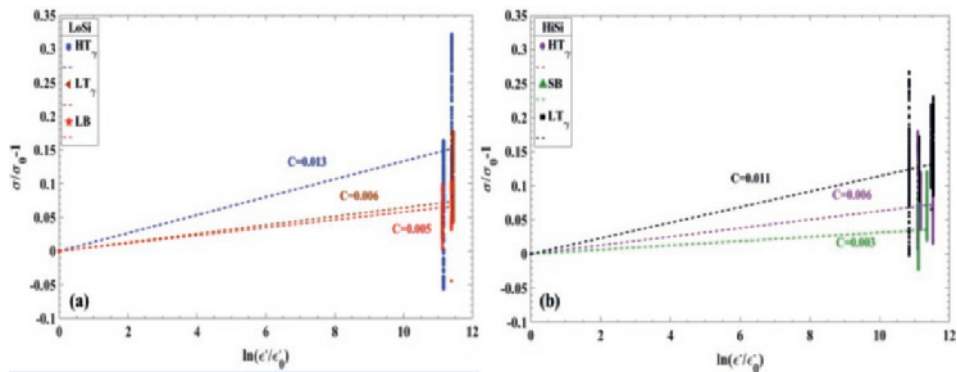


Figure 4-11. The dynamic to static true stress ratio as a function of the logarithmic dynamic to static strain rate for (a) LoSi samples and (b) HiSi samples. The slope indicates the strain rate sensitivity factor.

In figure 4-12a the strain rate sensitivity factor is plotted as a function of second phase constituents. It is seen that the higher the fraction of the 2<sup>nd</sup> phase constituents in the microstructure, the lower is the strain rate sensitivity factor. The separate effect of the RA phase in the HiSi grade on the strain rate sensitivity could not be detected due to the simultaneous change in the fraction of martensite phase. This is clearly illustrated in figure 4-12b, revealing that the higher RA fractions are accompanied with lower fractions of martensite phase in the HiSi grade. Nevertheless, the role of the martensite phase on decreasing the strain rate sensitivity has also been observed elsewhere [5-7]. Although the LB sample does not have any second phase constituents, as indicated by its grain size in figure 4-12a, it has a relatively low strain rate sensitivity factor. This can be explained by the fact that the LB sample shows a high yield stress attributed to its fine microstructure resulting from the low bainite transformation temperature of 390°C. Wei and Jia *et al.* [27, 28] reported the influence of grain size on the strain rate

sensitivity and showed that the strain rate sensitivity of BCC metals is inversely correlated to the multiplication of the activation volume ( $v^*$ ), defined as derivative of activation enthalpy with respect to stress, and flow stress ( $\tau$ ). However, in BCC metals,  $v^*$  is quickly leveled off by  $\tau$ . Thus, the strain rate sensitivity is scaled inversely with  $\tau$ . In addition,  $\tau$  follows the Hall-Petch relation for the influence of grain size. Therefore, strain rate sensitivity is reduced by the grain size. The correlation of grain size, initial yield stress, or  $A$  parameter, and strain rate sensitivity factor of all samples is shown in figure 4-13. Nevertheless, in the HiSi grade, see fig. 4-11b, the HT sample reveals a lower strain rate sensitivity compared to the LT sample, although it has a slightly larger grain size. This can be attributed to the approximately 3% higher volume fraction of martensite phase in the HT sample, compared to the LT sample.

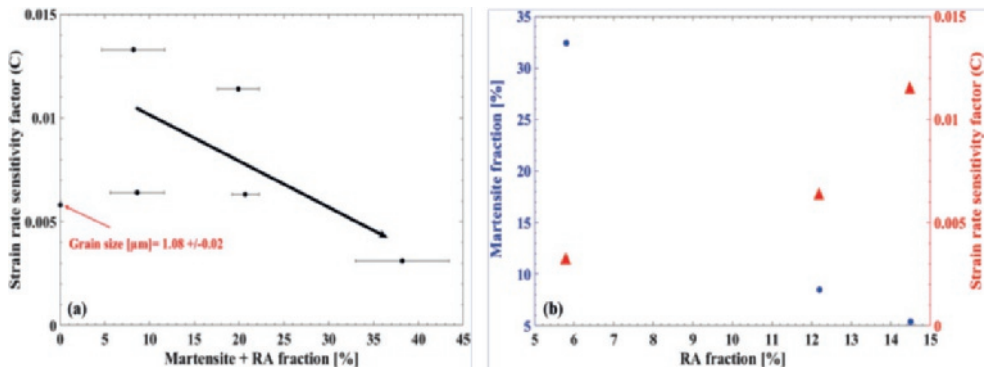


Figure 4-12. Strain rate sensitivity factor as a function of second phase constituents: (a) total fraction of martensite and RA and (b) total martensite fraction (M+ATM) versus RA fraction and strain rate sensitivity factor as a function of RA in the HiSi grade.

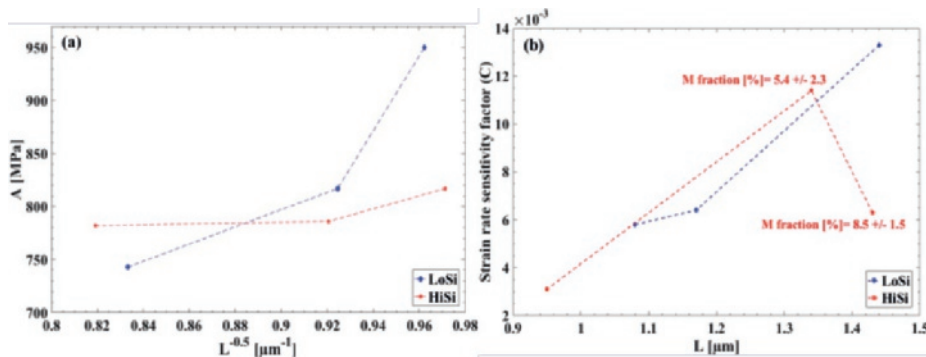


Figure 4-13. Correlation between grain size and mechanical properties: (a) initial yield stress  $A$  as a function of inverse square root of grain size and (b) strain rate sensitivity factor  $C$  as a function of grain size.

## 4.4 Conclusion

The effect of strain rate on the dynamic mechanical response of high and low silicon grades of bainitic multiphase steels is studied. A comprehensive characterization of the six considered multiphase steels by SEM-EBSD allowed to correlate the microstructural features with the quasi-static and dynamic mechanical responses. The individual role of retained austenite, martensite and grain size on ductility and strengthening is addressed. It is observed that both uniform elongation and strength under high strain rate deformation conditions are improved. Consequently, also the energy absorbed at high strain rates is enhanced, which is an important advantage for car crash events. For each steel, the static and dynamic tensile test results are used to fit the parameters of the phenomenological Johnson-Cook hardening model, including the important strain rate sensitivity factor. It is observed that the higher the fraction of second phase constituents, the lower the strain rate sensitivity becomes. However, the individual role of the RA phase on the strain rate sensitivity could not be addressed due to the simultaneous change of both M and RA phases in the HiSi grade. It is shown that the grain size as a microstructural parameter has a direct influence on the strain rate sensitivity, particularly, when other microstructural parameters such as second phase constituents do not change substantially. Additionally, a comprehensive literature survey revealed that the strain rate sensitivity of steels is strongly related with the yield stress and/or strength of the steels. Higher strength steels demonstrate a lower strain rate sensitivity. The strength-strain rate sensitivity relation can be approximated by a power law which is also followed by the bainitic steels considered in this study. The power law can provide a first, straightforward approximation of the strain rate sensitivity of steels.

## References

- [1] G.R.a.C. Johnson, W.H., A Constitutive Model and Data for Metals Subjected to Large Strains, High Strain Rates, and High Temperatures., Proceedings 7th International Symposium on Ballistics, The Hague (1983) 541-547.
- [2] P. Verleysen, J. Peirs, J. Van Slycken, K. Faes, L. Duchene, Effect of strain rate on the forming behaviour of sheet metals, Materials Processing Technology 211(8) (2011) 1457-1464.
- [3] J. Van Slycken, P. Verleysen, J. Degrieck, J. Bouquerel, B.C. De Cooman, Dynamic response of aluminium containing TRIP steel and its constituent phases, Mat Sci Eng a-Struct 460-461 (2007) 516-524.
- [4] X.C. Wei, R.Y. Fu, L. Li, Tensile deformation behavior of cold-rolled TRIP-aided steels over large range of strain rates, Mat Sci Eng a-Struct 465(1-2) (2007) 260-266.
- [5] W. Wang, M. Li, C. He, X. Wei, D. Wang, H. Du, Experimental study on high strain rate behavior of high strength 600-1000MPa dual phase steels and 1200MPa fully martensitic steels, Mater Design 47 (2013) 510-521.
- [6] H.D. Yu, Y.J. Guo, X.M. Lai, Rate-dependent behavior and constitutive model of DP600 steel at strain rate from 10(-4) to 10(3) s(-1), Mater Design 30(7) (2009) 2501-2505.
- [7] S. Oliver, T.B. Jones, G. Fourlaris, Microstructure and dynamic material performance of high strength and ultra high strength strip steels, Mater Sci Tech-Lond 23(1) (2007) 55-62.
- [8] T. Rahmaan, A. Bardelcik, J. Imbert, C. Butcher, M.J. Worswick, Effect of strain rate on flow stress and anisotropy of DP600, TRIP780, and AA5182-O sheet metal alloys, International Journal of Impact Engineering 88 (2016) 72-90.
- [9] S. Curtze, V.T. Kuokkala, M. Hokka, P. Peura, Deformation behavior of TRIP and DP steels in tension at different temperatures over a wide range of strain rates, Mat Sci Eng a-Struct 507(1) (2009) 124-131.
- [10] J.H. Kim, D. Kim, H.N. Han, F. Barlat, M.G. Lee, Strain rate dependent tensile behavior of advanced high strength steels: Experiment and constitutive modeling, Mat Sci Eng a-Struct 559 (2013) 222-231.
- [11] Z. Nie, G. Wang, J. Yu, D. Liu, Y. Rong, Phase-based constitutive modeling and experimental study for dynamic mechanical behavior of martensitic stainless steel under high strain rate in a thermal cycle, Mech Mater 101 (2016) 160-169.
- [12] C.C. Roth, D. Mohr, Effect of strain rate on ductile fracture initiation in advanced high strength steel sheets: Experiments and modeling, Int J Plasticity 56 (2014) 19-44.
- [13] J. Van Slycken, P. Verleysen, J. Degrieck, J. Bouquerel, Constitutive equations for multiphase TRIP steels at high rates of strain, J Phys Iv 134 (2006) 69-74.
- [14] Y.T. Tsai, C.R. Lin, W.S. Lee, C.Y. Huang, J.R. Yang, Mechanical behavior and microstructural evolution of nanostructured bainite under high-strain rate deformation by Hopkinson bar, Scripta Materialia 115 (2016) 46-51.
- [15] R.Q. Liang, A.S. Khan, A critical review of experimental results and constitutive models for BCC and FCC metals over a wide range of strain rates and temperatures, Int J Plasticity 15(9) (1999) 963-980.
- [16] H. Bhadeshia, Bainite in steels: transformation, microstructure and properties, IOM Communications Ltd, London2001.
- [17] R. Kapoor, S. Nemat-Nasser, Determination of temperature rise during high strain rate deformation, Mech Mater 27(1) (1998) 1-12.
- [18] J. Bouquerel, Y.p. Houbaert, P.p. Verleysen, Modelling and characterisation of multiphase TRIP steel under static and dynamic loading, Ghent university 2008.
- [19] C. Garcia-Mateo, F.G. Caballero, Ultra-high-strength bainitic steels, Isij Int 45(11) (2005) 1736-1740.
- [20] C. Garcia-Mateo, F.G. Caballero, C. Capdevila, C.G. de Andres, Estimation of dislocation density in bainitic microstructures using high-resolution dilatometry, Scripta Materialia 61(9) (2009) 855-858.
- [21] B. Shakerifard, J. Galan Lopez, F. Hisker, L.A.I. Kestens, Effect of banding on micro-mechanisms of damage initiation in bainitic/martensitic steels, Mat Sci Eng a-Struct 735 (2018) 324-335.
- [22] C.C. Tasan, J.P.M. Hoefnagels, M. Diehl, D. Yan, F. Roters, D. Raabe, Strain localization and damage in dual phase steels investigated by coupled in-situ deformation experiments and crystal plasticity simulations, Int J Plasticity 63 (2014) 198-210.
- [23] S. Curtze, V.T. Kuokkala, Dependence of tensile deformation behavior of TWIP steels on stacking fault energy, temperature and strain rate, Acta Mater 58(15) (2010) 5129-5141.
- [24] J.T. Benzing, W.A. Poling, D.T. Pierce, J. Bentley, K.O. Findley, D. Raabe, J.E. Wittig, Effects of strain rate on mechanical properties and deformation behavior of an austenitic Fe-25Mn-3Al-3Si TWIP-TRIP steel, Mat Sci Eng a-Struct 711 (2018) 78-92.
- [25] Z. Gronostajski, A. Niechajowicz, R. Kuziak, J. Krawczyk, S. Polak, The effect of the strain rate on the stress- strain curve and microstructure of AHSS, Materials Processing Technology 242 (2017) 246-259.
- [26] J.Y. Choi, J. Lee, K. Lee, J.Y. Koh, J.H. Cho, H.N. Han, K.T. Park, Effects of the strain rate on the tensile properties of a TRIP-aided duplex stainless steel, Mat Sci Eng a-Struct 666 (2016) 280-287.
- [27] Q. Wei, S. Cheng, K.T. Ramesh, E. Ma, Effect of nanocrystalline and ultrafine grain sizes on the strain rate sensitivity and activation volume: fcc versus bcc metals, Mat Sci Eng a-Struct 381(1-2) (2004) 71-79.
- [28] D. Jia, K.T. Ramesh, E. Ma, Effects of nanocrystalline and ultrafine grain sizes on constitutive behavior and shear bands in iron, Acta Mater 51(12) (2003) 3495-3509.

# Chapter 5 Effecting of banding on micro-mechanisms of damage initiation in bainitic/martensitic steels

**Abstract.** Understanding the micro-mechanisms of damage initiation during plastic deformation is a key to further mechanical properties enhancement. This chapter investigates, the topological effect of martensite as a second phase constituents on local damage nucleation activity. This effect is studied in two different martensite banded microstructures produced by two various annealing cycles discussed earlier in section 3.1.5. The post-mortem damage analysis by a scanning electron microscope on uniaxial loaded samples, reveals more damage nucleation along the dispersed and fragmented martensite phase within martensite banded regions. More pronounced strain partitioning is observed in coarse bainitic grains between adjacent martensite blocks. It is shown that the fracture strain is not controlled by local damage activities, implying that earlier damage initiation or an increased volume fraction of voids does not give rise to a reduced ductility.

**Keywords:** Bainite; Steel; Damage initiation; Topology; Banding; EBSD.

*Reproduced from:*

*Shakerifard. B, Lopez. J. G, Hisker. F, Kestens. L. A. I. Effect of banding on micro-mechanisms of damage initiation in bainitic/martensitic steels. Materials Science and Engineering A, 2018, 735, 324-335, doi: 10.1016/j.msea.2018.08.049.*

## 5.1 Introduction

In chapter 4, a comprehensive study on microstructure and quasi-static and dynamic mechanical response of the developed bainitic steels was conducted. The correlation between microstructures and their corresponding quasi-static and dynamic mechanical responses was shown. In addition, the influence of microstructural variables on the strain rate sensitivity was addressed. Nevertheless, understanding the micro-mechanical behavior and failure micro-mechanisms of such multi-phase steels is of crucial importance for designing a bainitic microstructure with enhanced properties. A thorough literature survey in chapter 2 with regard to various damage micro-mechanisms involved in multiphase steels was illustrated. Although micro-mechanisms of damage initiation in DP steels or/and in general the 1<sup>st</sup> generation of AHSSs have been studied in detail by many researchers, bainitic steels have not been addressed in the literature as to the same extent as the first generation. Multiphase bainitic steels with less mechanical phase contrast compared to DP steels are expected to have a delayed damage initiation behavior with lower fraction of damage sites [1].

The current chapter investigates the role of martensite bands as meso-scale heterogeneities on micro-mechanisms of damage initiation and macroscopic mechanical response under uniaxial tensile loading. This chapter is structured into six sections as follows: section 5.2.1 presents a comprehensive chemical, mechanical and morphological study on martensite bands of the annealed microstructures of the HT and LT samples from the LoSi grade. Micro-chemical segregation of alloying elements and their role on formation of martensitic bands is investigated by Electron Probe Microanalysis (EPMA). Morphological aspect of MA islands along the martensite bands are addressed by Scanning Electron Microscope (SEM) equipped with Electron Backscatter Diffraction (EBSD). Nevertheless, in order to further understand the topology of the bands and their associating mechanical contrast with respect to the matrix,  $\mu$ -hardness tests are conducted. The global quasi-static mechanical response of the HT and LT samples is assessed in section 5.2.2. Section 5.2.3 demonstrates the micro-mechanisms of damage initiation in the bainitic/martensitic samples, and the effect of bands topology on local damage nucleation. To this purpose, quantitative and statistical damage analysis is performed by SEM imaging and image processing. This allows deriving a criterion for the initiation of the damage within the microstructure. In addition, EBSD technique is employed in order to address the strain partitioning phenomenon among soft (bainite) and hard (martensite) phase due to the imposed macroscopic deformation. Eventually, the results in earlier sections will be discussed and concluded in sections 5.3 and 5.4.

## 5.2 Results

### 5.2.1 Microstructure characterization

Comprehensive SEM imaging through the thickness along the ND direction showed the presence of martensite bands parallel to the RD direction in the bainitic matrix of both LT and HT samples [2]. Figure 5-1(a and c) shows two SEM micrographs of the HT and LT samples, respectively. Bands are shown by arrows. The EPMA analysis (see figure 5-1(e)) perpendicular to the bands, as depicted in figure 5-1(a), illustrates the micro-segregation of Mn in these bands. It is observed that in the HT sample, the number of visible bands through the thickness is higher compared to the LT sample. Besides, the prior austenite grain sizes of the HT and LT samples are measured by EBSD analysis, which are  $4.9 \pm 0.3$  and  $4.2 \pm 0.3$   $\mu\text{m}$ , respectively. This difference is due to a higher austenization temperature in the HT sample. Thermodynamically, the coarser prior austenite grain size leads to a lower nucleation rate and/or slower kinetics of bainite transformation, particularly in the banded regions [3]. The HT sample reveals a coarser topology with larger distance between MA blocks while the bands in the LT sample are more fragmented due to a more complete bainite transformation in these regions. EBSD analysis also confirms the topological differences of the bands between both samples, in which the HT sample exhibits coarser networks of martensite bands along RD. Figure 5-1(b) and (d) show their corresponding image quality overlaid with phase maps, whereby dark bands with low IQ value are more apparent in the HT sample. The schematic illustration of the band topologies of the HT and LT samples is shown in figure 5-1(f and g). The fraction of retained austenite in both samples is less than 0.5%, due to the low silicon content in this bainitic steel [4].

Table 5-1 summarises the results of the microstructure characterization in both samples. The high temperature sample has the larger bainite grain size and the larger MA fraction compared to the LT sample. However, the fraction of cementite in both samples is approximately identical.

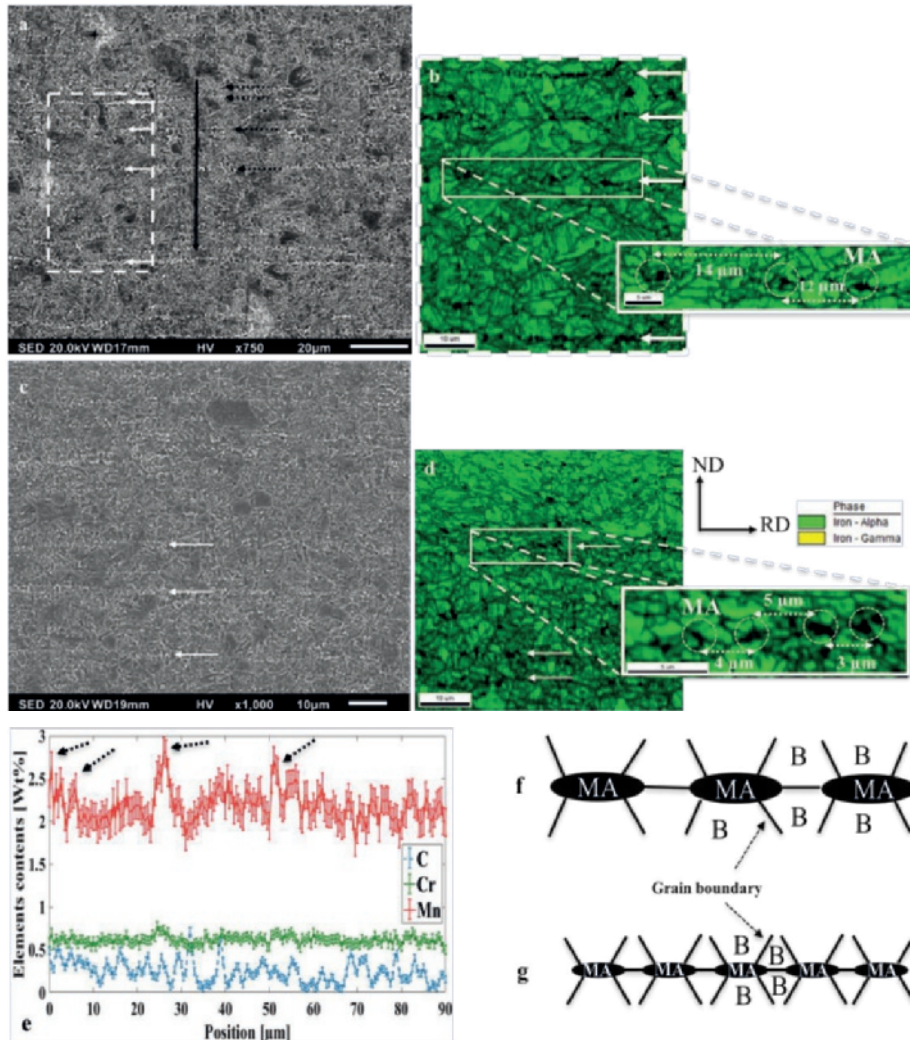


Figure 5-1. Microstructure characterization of both samples. The HT sample: (a) SEM micrograph where the dashed rectangle indicates the location of the EBSD analysis. The solid arrow is the position of the EPMA line analysis, (b) overlaid IQ and phase maps (solid white arrows show dark bands with low IQ value). The LT sample: (c) SEM micrograph, (d) overlaid IQ and phase maps. (e) EPMA chemical analysis with four arrows corresponding to the bands in the HT sample showed in (a) and (f and g) schematic illustration of the bands topology of the HT and LT samples, respectively.

Table 5-1. Microstructural variables of the high and low temperature samples.

Sample	Phase	Grain size (μm)	Second phase fraction (%)	Block size (μm)	Cementite size (μm)
HT	Bainite	$1.44 \pm 0.01$	-	-	-
	MA	-	$3.4 \pm 1.7$	$0.7 \pm 0.36$	-
	Cementite	-	$3.6 \pm 1.0$	-	$0.07 \pm 0.01$
LT	ATM	$0.5 \pm 0.1$	$4.8 \pm 1.8$	-	-
	Bainite	$1.17 \pm 0.03$	-	-	-
	MA	-	$2.4 \pm 0.7$	$0.6 \pm 0.25$	-
	Cementite	-	$3.1 \pm 0.7$	-	$0.07 \pm 0.01$
	ATM	$0.47 \pm 0.2$	$6.2 \pm 2.3$	-	-

## 5.2.2 Micro-hardness

Micro-hardness measurements along ND and RD are represented in figure 5-2(a and b), respectively. Figure 5-2(a) includes the schematic illustration of micro indentation through the thickness (along ND) in both samples. The dark regions represent the MA bands along RD and the background white medium represents the bainitic matrix including ATM. Comparing the Vickers micro-hardness profile of the HT and LT samples in figure 5-2(a), it is observed that HT sample shows more spread in micro-hardness values compared to the LT sample. This is observed by subtracting the first and third quartile of the box plots, interquartile rang (IQR), which in the case of the HT sample is 61 HV and it is approximately 2.3 times higher than IQR of the LT sample. The red line within the box plot is the median value. This value is lower in the HT sample compared to the LT sample due to its coarser microstructure. The whiskers of the micro-hardness profile represent the maximum and minimum values of the measurement points, while the outliers are the data points of which the values exceed  $1.5 \cdot \text{IQR}$  from the first and third quartiles of the box plot. In figure 5-2(b), the micro-hardness results along RD are shown on two locations within the microstructure corresponding to a matrix and a martensitic band. The box plots corresponding to the matrix of both samples demonstrate identical median values of 438 HV. However, the spread of the data is higher in the HT sample, while relatively lower hardness values are observed compared to the LT sample. Considering the bands in both samples, it is clearly observed that the HT sample exhibits higher Vickers hardness values and simultaneously higher spread. The median

difference of the bands hardness between two samples is 58 HV. The mechanical contrast of these two regions, bands and matrix, is compared by their median difference in both samples, whereby it is 27 and 85 HV in the LT and HT samples, respectively. Figure 5-2(a and b) shows a higher mechanical contrast between martensitic bands and matrix in the HT sample compared to the LT sample, which will be addressed in detail in the discussion section.

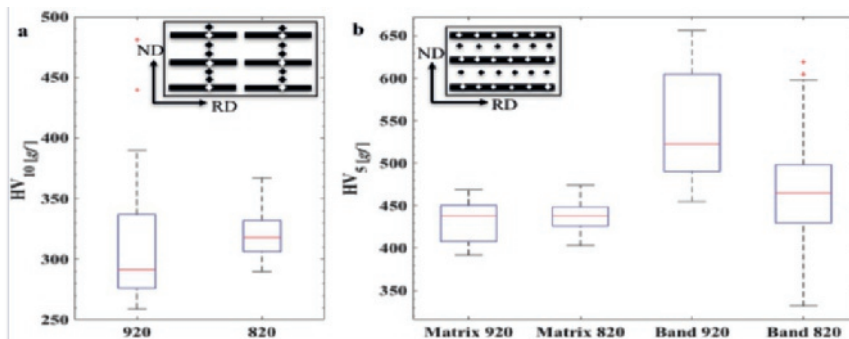


Figure 5-2. Box plot of micro-hardness measurements of low and high temperature samples: (a) Vertical micro-hardness profile of the LT and HT samples austenitized at 820 and 920°C performed with 10 gf load (Indentation is conducted every 50  $\mu\text{m}$ ), and (b) Horizontal micro-hardness measurements on the martensitic bands and the matrix of both samples loaded with 5 gf.

### 5.2.3 Tensile properties

The tensile diagram of the LT and HT samples along RD is shown in figure 5-3. It is observed that the HT sample, exhibits a small non-uniform elongation region after reaching the ultimate tensile strength point. Compared to the LT sample, the sample could not accommodate considerable elongation in the post necking stage. Table 5-2 lists the tensile properties of both samples loaded along the RD.

The tensile properties summarized in table 5-2 reveal higher yield and tensile stresses in the LT sample compared to the HT sample. This may be the result of a finer microstructure and higher ATM fraction in the LT sample. However, it has been shown earlier in section 5.2.1 that the LT sample has approximately 1% less MA fraction. Comparing the uniform elongation parameter between two

samples, the conventional inverse trend between the elongation and the strength is not observed. Both strength and ductility are increased in the LT sample.

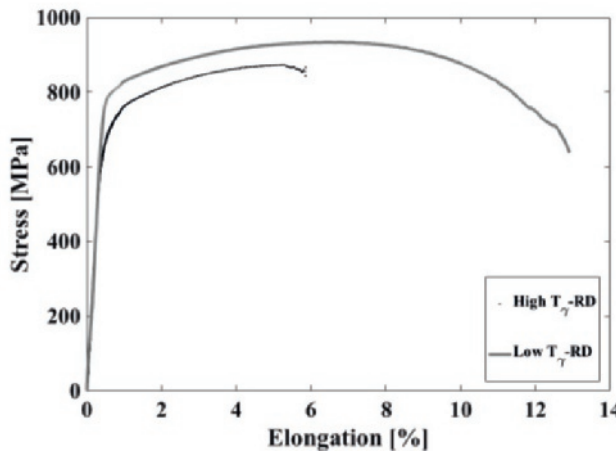


Figure 5-3. Engineering uni-axial tensile curve of the low and high temperature samples loaded along the RD.

Table 5-2. Tensile properties of the high and low temperature samples along the RD.

Sample	Yield stress [MPa]	Tensile strength [MPa]	Uniform elongation (%)	Total elongation (%)	Fracture strain (%)
HT	$743 \pm 9$	$874 \pm 9$	$5.0 \pm 0.14$	$5.35 \pm 0.07$	$112 \pm 5$
LT	$817 \pm 2$	$933 \pm 14$	$6.1 \pm 0.14$	$12.20 \pm 0.56$	$118 \pm 9$

### 5.2.4 Damage analysis

Post-mortem SEM microstructure observations of the tensile sample loaded along RD in the LT material interrupted at the elongation of 9.5%, showed few voids formation in the necked region. A similar interrupted test, at the elongation of 5% in the HT sample, showed no voids within the microstructure. Similarly, no voids were observed in the uniform regions of fractured tensile samples. These observations on the interrupted and fractured tensile samples of both materials confirmed the fact that voids are only initiated in the necked region at the terminal stages of deformation prior to final failure. However, in some dual phase (DP) steels, it has been reported that voids initiated prior to necking [5, 6]. Figure 5-4(a and b), shows SEM micrographs of void locations in the LT interrupted

sample etched by Nital. Most of the voids were initiated at the interface of bainite and martensite (B/M) along martensitic bands. However, a few voids by MA tearing is observed and no voids at the ATM phase either by the tearing or interface decohesion are observed. Figure 5-4(c and d) are SEM micrographs close to the fracture surface where martensite bands are deformed through shearing. The Klemm etchant used in figure 5-4(c and d) does not reveal the ATM phase, but it provides a clear difference between the MA phase and the surrounding bainitic matrix including ATM phase. A few tiny voids are also observed at the carbides within the microstructure close to fracture surface where either the carbides are fragmented or delaminated from the matrix. Due to their considerable smaller size compared to martensite related voids, it is assumed that their role on the integrity of the material is negligible.

Figure 5-5(a and b) depict the SEM micrographs of the fractured HT sample close to fracture surface where the alignment of martensite band along RD clearly reveals the occurrence of severe shearing. Voids are observed either at the B/M interface or by martensite tearing. Figure 5-5(c and d) show the voids at the B/M interface. Inverse pole figure (IPF) maps (figure 5-6(a) and (b)) exhibit two EBSD analyses on the interrupted LT material at the localized region of the tensile sample. Two locations are captured where voids are mainly observed; first, along martensite bands as shown in figure 5-4 and 5(b) and second, between two adjacent parallel bands where a shear bands is also triggered as shown in figure 5-6(a). Figure 5-7, similarly shows an EBSD analysis on the interrupted HT sample at the martensite banded region. The kernel average misorientation (KAM) map (Figure 5-7(c)) demonstrates the high local misorientation ( $>7^\circ$ ) and simultaneously low confidence index ( $CI<0.1$ ) in MA islands close to their interface with the bainitic matrix. This may be due to the shearing of the B/M interface, which in a later stage extends the deformation to the martensite [7]. In addition, the intrinsic high dislocation density of the martensite phase can lead to high KAM values locally. Besides, it is observed that traces with lower KAM values (around  $2.5^\circ$ ) are triggered between the MA islands within the bainitic matrix which indicates a local strain gradient due to local dislocation glide. In figure 5-7(a1, a2 and a3), three subsets from local MA regions and their surrounding bainitic matrix are shown. In figure 5-7(a1), a notched MA island is observed where a high GROD value of  $12^\circ$  has accumulated at the notch while at the sides of the notch almost no rotation is observed. Nevertheless, the coarse bainite grains at the top and bottom of the notched MA islands exhibit high GROD values close to the B/M interface, which also coincides with high angle grain boundaries (HAGBs). The high GROD values indicate the local crystal rotation and the strain partitioning effect in coarse bainitic grains compared to MA regions where low GROD values are observed. It is expected that the MA region as a hard phase

is more resistant to straining. This phenomenon is also observed in the microstructures of figure 5-7(a1 and a2), where high GROD values are observed in the coarse bainite grains at the vicinity of the B/M interfaces. However, in fine grains this long-range orientation gradient is not observed. Despite coarse grains, which are more prone to plastic deformation, fine bainitic grains often show low GROD values. This is either as a result of their resistance to deformation due to their size effect compared to coarser grains or because of grain fragmentation close to MA islands that can lead to grain refinement. However, the latter mechanism is less likely due to the low level of macroscopic imposed strain. In GROD maps the local white regions at the interface of B/M are associated with poorly indexed pixels, indicated by the low C.I (<0.05) values. This is due to the local severe crystal distortion. These regions are also located closely to regions with high local lattice rotations which can be potentially damage nucleation sites as reported by Archie and Humphreys et al. [8, 9].

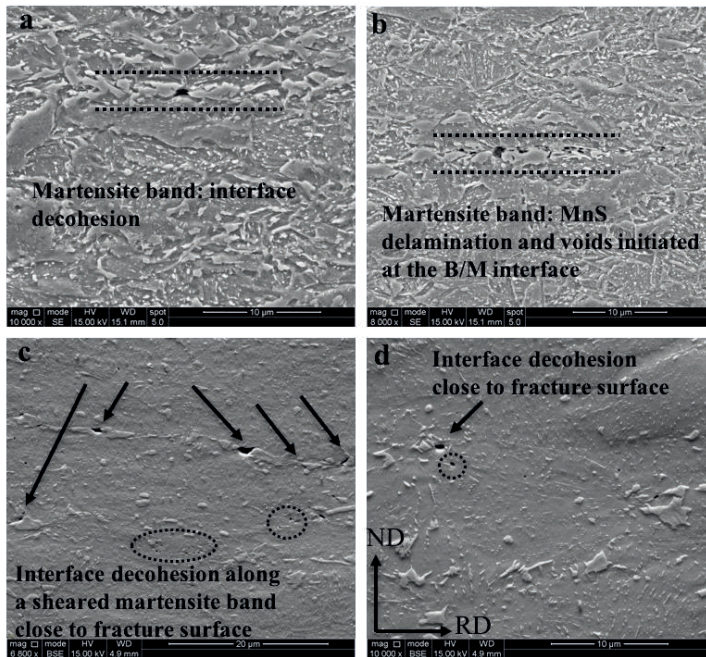


Figure 5-4. SEM micrographs of the LT sample: (a and b) micrographs of the interrupted sample at 9.5% elongation RD parallel to loading direction (RD//LD) etched by Nital and (c and d) micrographs of the fractured sample (RD//LD) etched by Klemm. Dashed circles depict the carbide related voids.

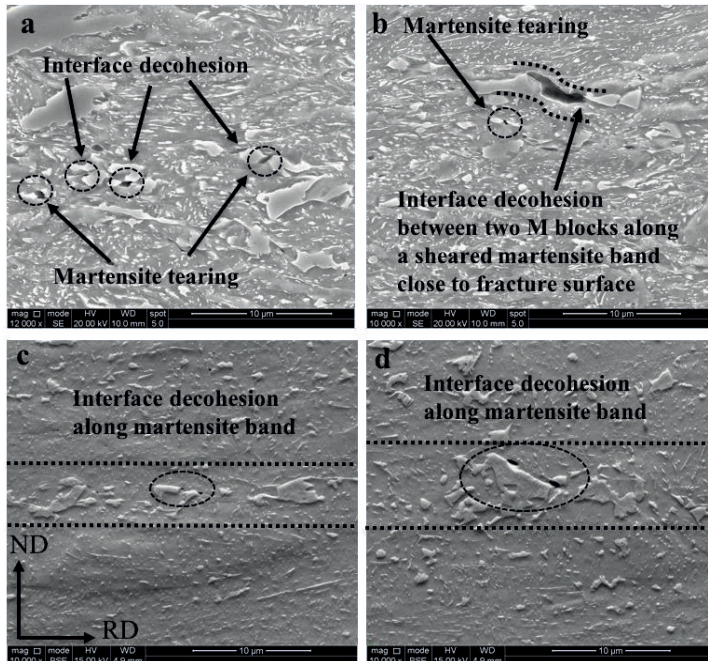


Figure 5-5. SEM micrographs of the HT sample: (a and b) micrographs of the fractured sample (RD // LD) etched by Nital close to the fracture surface and (c and d) micrographs of the fractured sample (RD// LD) etched by Klemm.

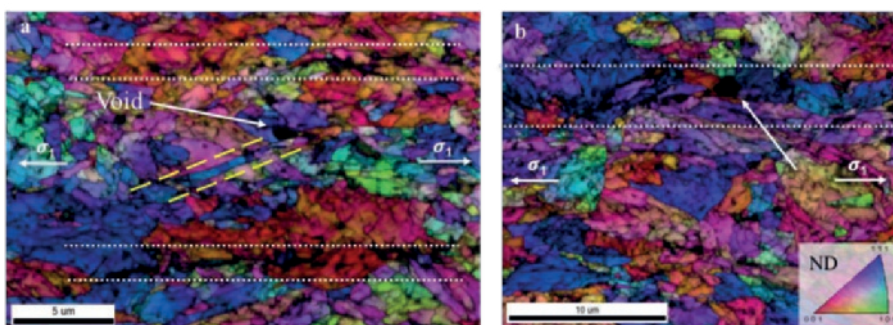


Figure 5-6. Two EBSD analysis on the interrupted LT sample at the strain level of 9.5%. The Banded region is indicated by the two dashed lines and voids are indicated by white arrows: (a) Inverse pole figure (IPF) overlaid by image quality (IQ) map reveals a void initiated between two martensitic band along the shear band shown by yellow dashed lines and (b) a IPF+IQ map of another void initiated along a martensite band.

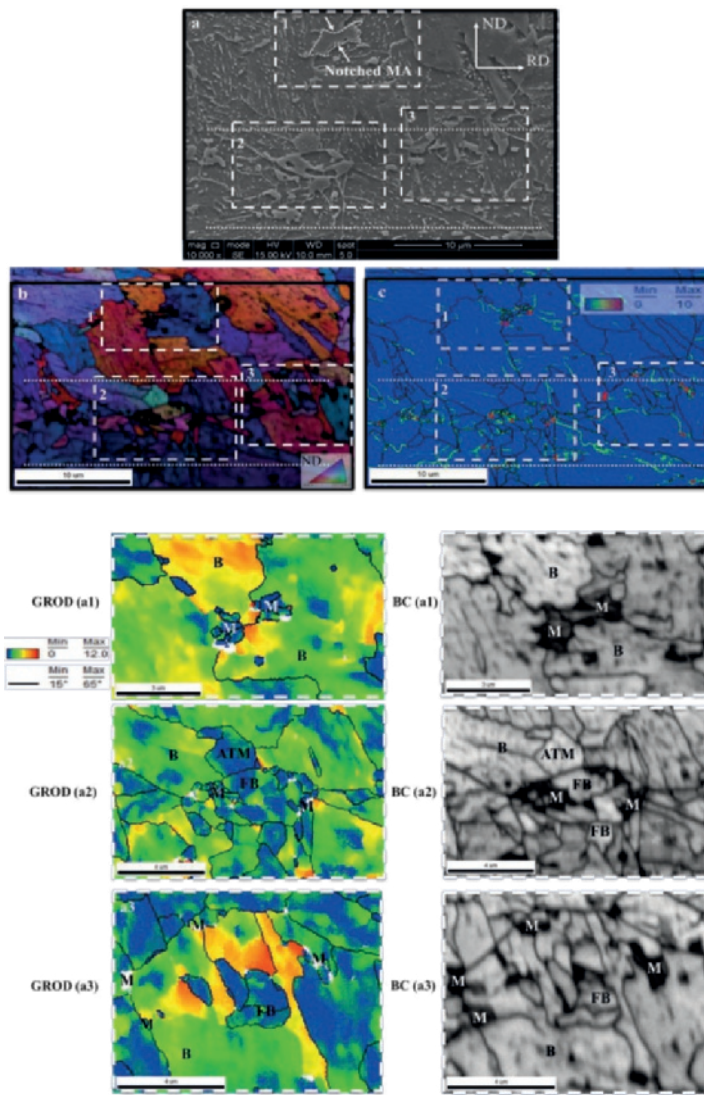


Figure 5-7. EBSD analysis on the interrupted HT sample at the strain level of 5%. The Banded region is indicated by the two dashed lines. (a) SEM micrographs, (b) IPF+IQ map, (c) KAM map and (a1, a2, and a3) the corresponding GROD and BC maps of regions indicated by dashed rectangle in the SEM micrograph 7(a). B, FB, ATM and M corresponds to bainite, fine bainite, tempered martensite and MA island, respectively. High angle grain boundaries ( $>15^\circ$ ) are indicated by the black line in GROD maps. White regions within GROD maps are pixels with low CI value.

The distribution of voids in both LT and HT samples are depicted in figure 5-8 on a 2D section of the macro-structure. Since voids are extremely small, voids are magnified 50X with respect to background matrix in the enhanced visualization of Fig. 5-8. Comparing figure 5-8(a) and (b), it is clearly observed that a higher quantity of voids is present in the LT sample. The accumulation of voids is observed close to the fracture surface, where a high level of local plastic deformation exists. Upon necking, the triaxiality of stress mode is changed. In the vicinity of the fracture surface it reaches its maximum due to the thickness and width reduction. This also leads to more void incidents. In figure 5-8(b), in the vicinity of the fracture surface, where a high quantity of voids is accumulated, it can be observed that voids are initiated along lines extending towards the fracture surface. However, this trend is less pronounced in the HT sample compared to the LT sample (compare figure 5-8a and b). The dashed circles are regions where MnS stringers within the segregation martensitic bands are delaminated from the matrix as shown in figure 5-4(b) thus acting as local stress concentrators for the M/B interface decohesion. The area fraction of MnS and  $\text{Al}_2\text{O}_3$  inclusions were quantified by 360 optical micrographs (300X magnification) per sample and an area fraction was found of  $0.0025 \pm 0.0005\%$ . This fraction is low enough, so that it is not expected to have an impact on the global fracture process [10].

Voids density (VD) and area fraction (VAF) of both LT and HT samples as a function of true plastic strain are shown in figure 5-9(a) and (b), respectively. VD reveals the nucleation rate of void incidence, while VAF may include three events: nucleation, growth and /or void coalescence. The LT sample exhibits the higher VD and VAF compared to the HT sample. Besides, it shows oscillations in VD and VAF between strain levels of 0.38 and 0.59, which is a result of local variations in MnS delamination toward the fracture surface, cf. figure 5-6(b). It is observed that around 0.6 and 0.75 of plastic strain VD and VAF start to increase in low and high temperature samples, respectively.

Figure 5-10(a) shows the box plot of voids perimeter in both samples corresponding to each strain level. It is clearly shown that the void perimeter does not show any trend with strain level. In figure 5-10(b), the true plastic strain of both samples is plotted as a function of distance from the fracture surface. It is shown that the LT sample has a higher strain gradient in its neck region compared to the HT sample. This indicates a relatively higher stress triaxiality in the LT sample within its necked region.

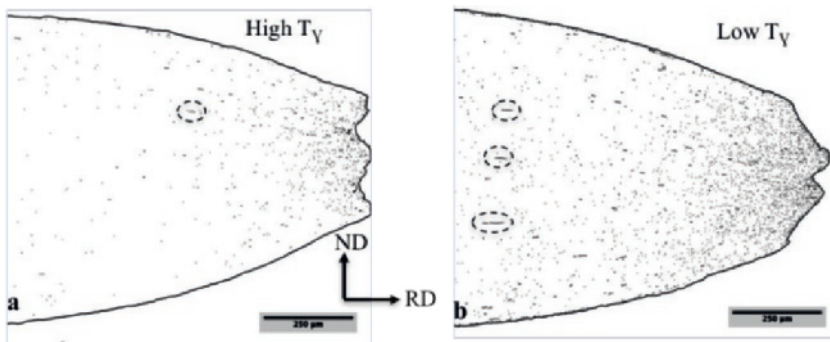


Figure 5-8. Approximately 1000 contiguous high resolution SEM micrographs (each  $\approx 27 \times 32 \mu\text{m}^2$ ): (a) high temperature and (b) low temperature samples. Dashed circle lines are examples of MnS fracture and delamination from the matrix.

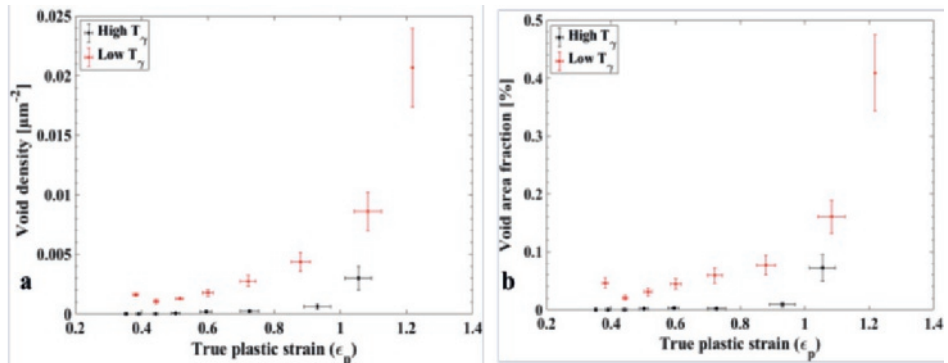


Figure 5-9. Void quantification: (a) void density vs. local true plastic strain and (b) void area fraction vs. local true plastic strain.

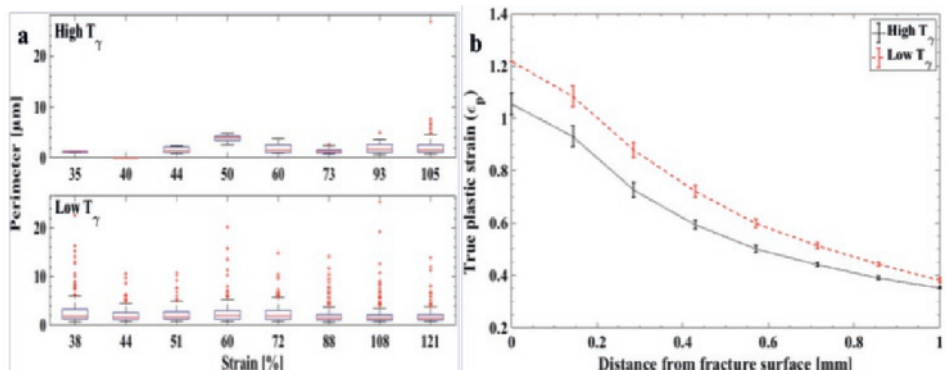


Figure 5-10. (a) Box plot of voids perimeter and (b) true plastic strain vs. distance from the fracture surface.

### 5.2.5 Fractography

Figure 5-11 and 12 show the fractographs of the LT and HT samples, respectively. The primary fracture surface observations of both LT and HT samples show that the LT sample has a rougher fracture surface with more surface perturbations compared to the HT sample. This is also apparent by observing the RD-ND cross sections of both samples in figure 5-8. In both samples, two main zones are observed. At the centre of the fracture surface along the ND direction, a fibrous zone is located, while at the two extreme edges, above and below the fibrous zone, the cleavage zone exists. It is observed that the LT sample has a larger population of small dimples with more heterogeneity in size, while in the HT sample, dimples are more homogenous in size. Particularly, the internal walls of large dimples reveal serpentine glide features [11], surrounded by small dimples (figure 5-11 and 12a). More continuous networks of cleavage facets are observed in the HT sample compared to the LT sample (figure 5-11 and 12c). Nevertheless, these facets are also observed in the LT sample in the fibrous zone, in a more discontinuous manner (figure 5-11c).

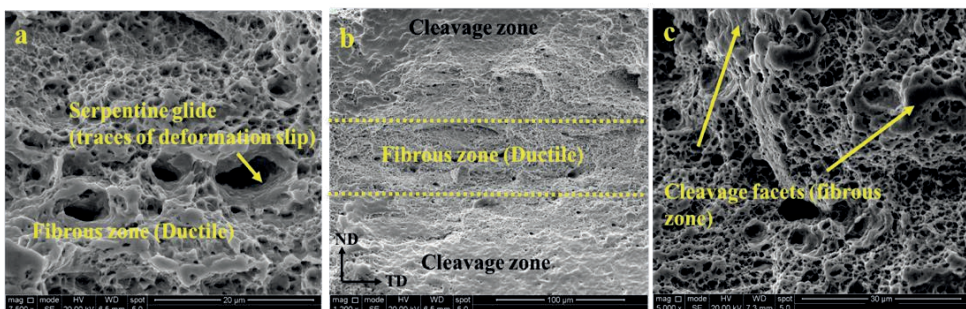


Figure 5-11. SEM fractographs of the LT sample revealing features of both ductile and brittle fracture: (a) Fibrous (ductile)zone with traces of stair-like deformation slip called serpentine glide, (b) two regions of fracture including ductile and cleavage fracture and (c) Small traces of cleavage facets in the fibrous zone.

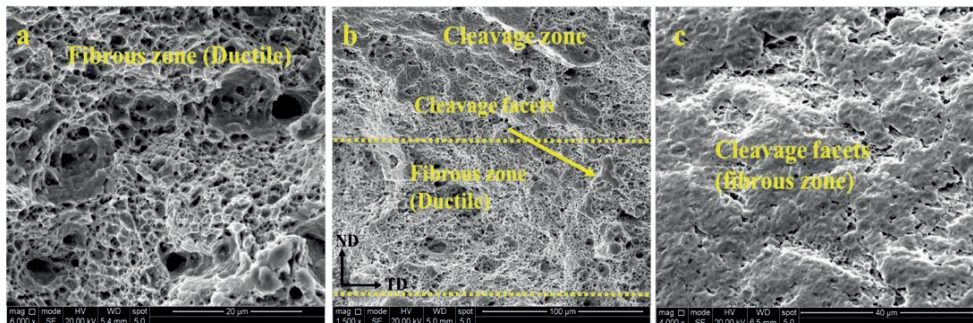


Figure 5-12. SEM fractographs of the HT sample revealing features of both ductile and brittle fracture: (a) Fibrous (ductile) zone with traces of stair-like deformation slip called serpentine glide, (b) two regions of fracture including ductile and cleavage fracture and (c) large traces of cleavage facets in the fibrous zone.

## 5.3 Discussion

Microstructural observations by SEM-EBSD revealed the presence of martensite bands in both LT and HT samples. The character and topological difference of the bands in both samples were analysed by SEM and micro hardness. SEM micrographs revealed the more fragmented and finer martensite bands in the LT sample. Besides, two different micro-hardness tests along ND and RD showed quantitatively the different mechanical behaviour of bands in both samples due to their topological differences. The LT sample showed less contrast between bands and the matrix caused by the fragmentation and finer topology of the bands (see figure 5-2). The interaction of the finer MA phase interrupted by the adjacent soft matrix with the indenter leads to a relatively lower hardness values of bands in the LT sample, compared to the HT sample. The bands in HT sample revealed higher scatter in the hardness value compared to the bands in LT sample. This is due to the fact that the indentation along the band occasionally are located either in the soft matrix between two separated coarse MA blocks or in a coarse MA block (see figure 5-1b and f).

The macroscopic tensile properties of both samples reflect the effect of grain size and volume fraction of micro constituents. The finer microstructure of the LT sample and relatively higher fraction of ATM resulted in strengthening, while the topological difference and the relatively lower volume fraction of MA phase lead to approximately 1 and 6% higher uniform elongation and fracture strain, respectively. Particularly, the LT sample showed relatively considerable post necking deformation compared to the HT sample. This can be explained by the particular microstructure of the LT sample, i.e. the interrupted and more dispersed networks of MA bands within the soft matrix accommodates more homogeneously

the plastic deformation compared to the HT sample. However, the microstructure of HT sample shows coarser bands and the distance between adjacent MA blocks along the band is also larger. This resulted in the earlier deformation localization and macroscopic fracture in the HT sample compared to the LT sample. This is in line with the study of Tasan *et al.* and de Guess *et al.* [12, 13] in which a homogeneous distribution of fine martensite phase within a soft ferrite matrix resulted in a higher strain hardening capacity and a better dispersed strain accommodation by surrounding ferrite grains.

Voids initiation was mainly observed at the interface of B/M along martensite bands. However, void nucleation by martensite tearing was more observed close to the fracture surface of the HT sample, in which the MA islands were coarser and can potentially accommodate more plastic deformation (see figure 5-5a and b). Figure 5-7(a1) shows an MA island with a notch, where it can cause local stress concentration. The corresponding GROD map reveals a high strain gradient at the notch, where a potential damage initiation spot may be located through martensite tearing, as similarly reported by Yan *et al.* and Archie *et al.* [9, 14]. A few voids at the carbides, either by delamination or carbide fragmentation were also observed. However, due to the low fraction and small size of the carbides, these voids did not play a significant role in the overall damage evolution and global failure of the material. In these bainitic steels, voids initiated at the terminal stages of deformation prior to the final failure in the necked region of the tensile samples. This is due to the lesser phase contrast present in these steels compared to DP steels where damage initiates prior to the strain localization point [5, 6]. The topological aspect of the bands in both samples also played a significant role in damage initiation. The discontinuity and narrow channel distance between two MA blocks along the martensitic band provided more potential damage sites as so called “hot-spots” for the void initiation in the LT sample [12, 14, 15]. This configuration was clearly shown by the SEM micrographs in figure 5-4(a and b). The EBSD analysis on the interrupted HT sample shown in figure 5-7(c), clearly unravels the effect of this configuration on the local short-range misorientations (KAM). The local misorientations observed between M blocks, interrupted by the soft matrix, are inclined with respect to the loading direction, possibly along the maximum resolved shear stress direction. This indicates the presence of a strain gradient in the bainite grains between two M blocks. Moreover, the strain partitioning effect was observed by assessing the long-range orientation gradient as shown in figure 5-7(a1, a2 and a3), where specifically coarse bainitic grains show locally higher GROD values compared to fine bainitic grains

---

close to phase interfaces. This implies that coarse bainitic grains are more prone to plastic deformation compared to fine bainitic grains and martensite (ATM and MA) phase.

Considering the band's meso-scale configurations in both samples with their corresponding topological differences along with their damage activities in figure 5-9, it is observed that the LT sample showed higher damage incidents (VD and/or VAF) compared to the high temperature sample at the same strain levels. The shorter distance between MA blocks in the fragmented bands of LT sample results in a higher local strain gradient within the soft matrix between two adjacent MA islands. Therefore, as reported by Yan *et al.* [14], the critical local strain in which a void initiate is lower and this leads to more damage incidents. This is also reflected in an earlier increase in void quantities (VD and VAF), at the strain level of 0.6 in the LT sample compared to 0.75 in the HT sample. Higher damage incidents lead to more local stress relaxation and depending on the microstructural features of grains surrounding a void such as size, orientation and the meso-scale arrangements of the hard phase, the initiated void can be arrested by the local strain hardening.

A meso-scale microstructural arrangement surrounding a void was shown in figure 5-6(a), where a nucleated void along a shear band between two adjacent martensite bands was observed. Micro-mechanically, this arrangement would favour shear band formation within the region between two close parallel bands and thus having a damage site within such a shear band can potentially enhance localization of deformation and eventually macroscopic failure. De Geus *et al.* in a systematic study by using an isotropic model reported the importance of deformation localization and the relative arrangement of voids on global failure through the linking of damage sites along  $45^\circ$  with respect to the loading direction [1, 13]. The fracture surface perturbations showed by black contours in both samples (see figure 5-8) depicts the  $45^\circ$  angle with respect to loading direction where can imply the linkage of damage sites just before the global failure.

Eventually, the higher quantity of the voids within the microstructure and earlier damage initiation cannot essentially lead to earlier macroscopic failure but rather the meso-scale arrangement of the hard phase causes either earlier localization of the deformation followed by the macroscopic failure or delaying the deformation instability. The quantitative analysis on void size distribution against plastic deformation in figure 5-10(a) demonstrates no clear correlation between plastic deformation and void growth. However, this observation is based on the RD-ND cross section. Avramovic-Cingara *et al.* [5] have observed the void growth along transversal direction on the ND-TD section close to the fracture surface. This observation is consistent with the dimples shape at the fracture surface of both samples (see figure 5-11 and 12), which are elongated along TD. Therefore, it is expected that voids grow along the TD direction at the vicinity of fracture surfaces. By comparing the voids sizes of both samples, it is

seen that the LT sample has relatively larger voids size compared to the HT sample. This is as a result of the higher stress triaxiality in the LT sample with respect to the HT sample. The fracture surface of both samples illustrates typical cup-cone fracture behaviour. Nevertheless, at the edge of the fracture surface in both sample, the traces of cleavage fracture were also observed. The LT sample presents more ductile fracture behaviour due to the presence of denser small and large dimples compared to the HT sample, where more extended and continuous facets are seen, even in its fibrous zone.

## 5.4 Conclusion

The micro-mechanisms of damage initiation in a low silicon bainitic steel have been addressed in this paper. The less contrast in mechanical properties between bainite and martensite delays damage initiation to the latest stages of the plastic deformation prior to final failure. The topology of martensite bands significantly affects void nucleation and macroscopic plastic deformation. The dispersion and fragmentation of martensite bands with a short distance between MA blocks, separated by the relatively softer bainitic matrix resulted in an improvement of ductility. However, this topological character locally resulted in a higher frequency of damage nucleation events. It was observed that small grains are more resistance to plasticity compared to coarse grains, and are able to prevent voids to coalesce.

Bands are meso-scale microstructural heterogeneities with a specific topology and with a certain mechanical contrast with respect to the surrounding matrix. The specific topology, which consists of parallel banded patterns that are fragmented at certain distances, favour shear banding in bainitic microstructure. The strain localization, particularly when occurring early on, leads to failure at lower strain levels. Eventually, it was observed that the macroscopic response of the material is controlled by the length-scale of heterogeneities within the microstructure, rather than by local damage activities. Normally, microstructure homogenization may not be industrially feasible due to the time and temperature limitations. Therefore, lowering the austenization temperature can help to fragment martensitic bands through the accelerated kinetics of bainite transformation.

## References

- [1] T.W.J. de Geus, R.H.J. Peerlings, M.G.D. Geers, Microstructural topology effects on the onset of ductile failure in multi-phase materials - A systematic computational approach, *Int J Solids Struct* 67-68 (2015) 326-339.
- [2] G. Krauss, Solidification, segregation, and banding in carbon and alloy steels, *Metall Mater Trans B* 34(6) (2003) 781-792.
- [3] S.E. Offerman, N.H. van Dijk, M.T. Rekvedt, J. Sietsma, S. van der Zwaag, Ferrite/pearlite band formation in hot rolled medium carbon steel, *Mater Sci Tech-Lond* 18(3) (2002) 297-303.
- [4] H.K.D.H. Bhadeshia, D.V. Edmonds, Bainite in Silicon Steels - New Composition Property Approach .1., *Met Sci* 17(9) (1983) 411-419.
- [5] G. Avramovic-Cingara, Y. Ososkov, M.K. Jain, D.S. Wilkinson, Effect of martensite distribution on damage behaviour in DP600 dual phase steels, *Mat Sci Eng a-Struct* 516(1-2) (2009) 7-16.
- [6] D.L. Steinbrunner, D.K. Matlock, G. Krauss, Void Formation during Tensile Testing of Dual Phase Steels, *Metall Trans A* 19(3) (1988) 579-589.
- [7] H.P. Shen, T.C. Lei, J.Z. Liu, Microscopic Deformation-Behavior of Martensitic Ferritic Dual-Phase Steels, *Mater Sci Tech-Lond* 2(1) (1986) 28-33.
- [8] F.J. Humphreys, Local Lattice Rotations at 2nd Phase Particles in Deformed Metals, *Acta Metall Mater* 27(12) (1979) 1801-1814.
- [9] F. Archie, X.L. Li, S. Zaefferer, Micro-damage initiation in ferrite-martensite DP microstructures: A statistical characterization of crystallographic and chemical parameters, *Mat Sci Eng a-Struct* 701 (2017) 302-313.
- [10] G. Krauss, Deformation and fracture in martensitic carbon steels tempered at low temperatures, *Metall Mater Trans A* 32(4) (2001) 861-877.
- [11] C.R. Brooks, A. Choudhury, *Failure Analysis of Engineering Materials*, McGraw-Hill Education2002.
- [12] C.C. Tasan, J.P.M. Hoefnagels, M. Diehl, D. Yan, F. Roters, D. Raabe, Strain localization and damage in dual phase steels investigated by coupled in-situ deformation experiments and crystal plasticity simulations, *Int J Plasticity* 63 (2014) 198-210.
- [13] T.W.J. de Geus, R.H.J. Peerlings, M.G.D. Geers, Fracture in multi-phase materials: Why some microstructures are more critical than others, *Engineering Fracture Mechanics* 169 (2017) 354-370.
- [14] D.S. Yan, C.C. Tasan, D. Raabe, High resolution in situ mapping of microstrain and microstructure evolution reveals damage resistance criteria in dual phase steels, *Acta Mater* 96 (2015) 399-409.
- [15] H. Kumar, C.L. Briant, W.A. Curtin, Using microstructure reconstruction to model mechanical behavior in complex microstructures, *Mech Mater* 38(8) (2006) 818-832.



# Chapter 6 Crystallographically resolved damage initiation in advanced high strength steels

**Abstract.** The improvement of macroscopic mechanical performance is not feasible without a deep understanding of the micromechanical behavior and failure micro-mechanisms involved during its response under various loading conditions. In this chapter, a new method is examined to study the micro-mechanisms of plastic work dissipation after the void initiation. In addition, this method is examined to address the correlation between crystallographic orientation and damage initiation. It is shown that upon damage initiation, stress relaxation is rather controlled by the void growth rather than local plasticity around the initiated voids. In addition, a post-mortem electron backscatter diffraction analysis performed around the 33 voids could enable us to calculate the Void-Orientation Distribution Function (VODF). Later, in chapter 7, these orientations are evaluated by the Visco-Plastic Self-Consistent (VPSC) model in order to investigate their role in damage initiation based on the stress/strain partitioning.

**Keywords:** bainite; crystallography; ductile-failure; micro-mechanisms; EBSD; ODF.

*Reproduced from:*

*Shakerifard. B, Lopez. J. G, Hisker. F, Kestens. L. A. I. Crystallographically resolved damage initiation in advanced high strength steel. Iop Conf Ser-Mat Sci, 18th International Conference on Textures of Materials (Icotom-18), doi: Unsp 01202210.1088/1757-899x/375/1/012022.*

## 6.1 Introduction

In multiphase steels, it has been well studied that microstructural heterogeneities such as different phases with various mechanical properties, play a significant role in the partitioning of stress and/or strain during plastic deformation [1-4]. Hence, at the microstructure level, these local deformation incompatibilities may induce void formation in order to dissipate the plastic work.

As explained earlier in chapter 2, section 2.3.1, the morphological effect (size, shape and distribution) of the second phase in dual phase steels (*i.e.* martensite) on ductile damage initiation, including nucleation, growth and coalescence of voids has been extensively studied by advanced experiments and crystal plasticity models [5-8]. In addition, the role of crystallographic orientation in stress (and/or strain) partitioning is another factor that needs to be considered as discussed earlier in section 2.3.2. Jia *et al.* [9] have shown in a duplex stainless steel that at high macroscopic stresses, when all grains in both constituent phases deform plastically, the role of the crystallographic orientation anisotropy on stress-strain partitioning is more significant than the mechanical contrast between phases (see section 2.3.1). The role of crystallographic orientation on damage initiation at relatively high levels of plastic deformations was also observed on metal-matrix [10] and rigid fiber composites [11] or alternatively in an austenitic stainless steel under the cyclic loading condition [12]. Eventually, the competing and multiplicative effect of phase contrast, with various topologies, and crystallographic orientations on damage initiation is a frequent topic of investigation [6, 12, 13]. In chapter 5, the role of heterogeneities and their corresponding topological effect was investigated. In the current chapter, the crystallographic orientation aspect of damage initiation is studied in order to understand the correlation between crystallographic orientation and damage. Therefore, an electron backscatter diffraction (EBSD) based analysis is used to characterize the orientations around the voids. Afterwards, textures are calculated and compared in order to understand the mechanisms of plastic work dissipation on damage initiation.

The bainitic steel used in this chapter is the high temperature (HT) sample from the low silicon bainitic steel (LoSi) grade introduced earlier in Chapter 3. The chemical composition and the corresponding annealing cycle of the HT sample are shown in table 3-2 and 3-4. The microstructure is composed of a predominant bainite matrix and a small fraction of martensite with MA blocks with negligible fraction of retained austenite (<0.5%) as depicted in chapter 4 (cf. tab. 4-1). Two uniaxial tensile tests were conducted at room temperature, which is illustrated in section 6.2.1. Two interrupted tensile tests were performed in the uniform and non-uniform regions of the plastic domain in order to monitor the

evolution of the voids within the microstructure as discussed in chapter 5, section 5.2.4. The detailed description of the EBSD analysis was illustrated earlier in chapter 3, section 3.5.

## 6.2 Results and discussion

### 6.2.1 Mechanical response

The mechanical response of the material is shown in figure 6-1. Considering the engineering flow curve of the material, a small non-uniform region is observed. Therefore, the material could not accommodate considerable plastic deformation right after the uniform region of the flow curve. The small localized necking behaviour of the material also confirms the small post-necking region of the flow curve.

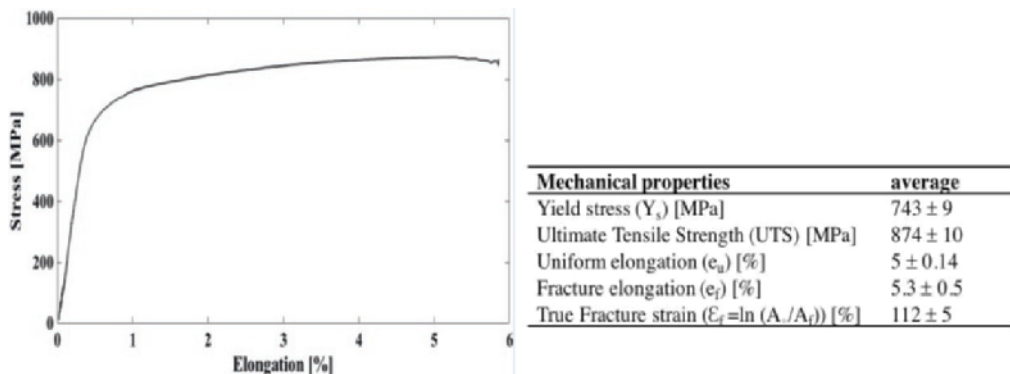


Figure 6-1. Engineering flow curve of the material under quasi-static loading condition. Mechanical properties calculated from the tensile curve.

### 6.2.2 Void mapping

This section summarises the damage activity of the HT sample from the LoSi grade as it was discussed in details in chapter 5. The void map shown in figure 6-2a, reveals the distribution of voids adjacent to the fracture surface. Voids are only initiated beyond uniform plastic deformation toward the finishing stage of necking, prior to final failure of the material. Indeed, the interrupted tensile sample at

the elongation of 5% confirmed the absence of void formation within the microstructure prior to necking.

As it was illustrated earlier in chapter 5, voids were quantified by two parameters: the void number density and the void area fraction. The void number density is related to void nucleation within the microstructure during deformation. The void area fraction reveals information with regard to subsequent steps of the micro-mechanisms of ductile damage initiation, growth and coalescence (see figure 6-2b). True plastic strain values are calculated in equally distanced intervals from the fracture surface based on the transverse and normal strains. The strain gradient, as function of distance from the fracture surface, is remarkably high close to the fracture surface as depicted in figure 5-10 section 5.2.4. It is observed that both factors increase with plastic deformation. These two parameters are relatively low until almost 73% of plastic deformation. However, upon reaching this strain level, a pronounced increase in the damage incidents is observed. The localization of the deformation (localized necking) close to fracture surface leads to higher triaxiality of the stress mode and, consequently, damage is accumulated in this region.

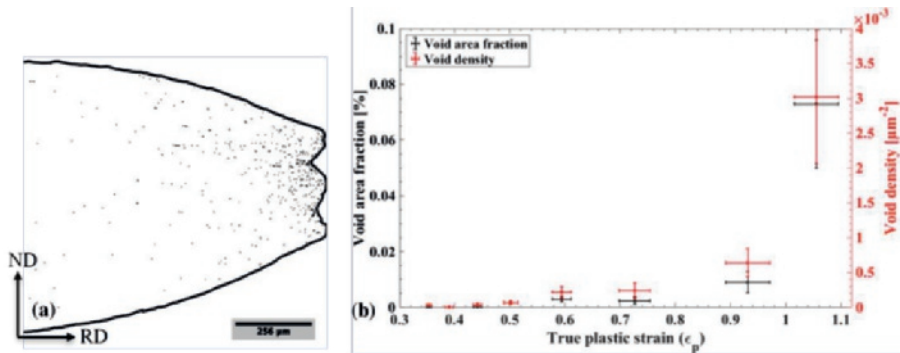


Figure 6-2. Void mapping analysis: (a) distribution of voids within the microstructure (in order to enhance the visual contrast between voids and the background matrix, voids are enlarged approximately 100x) and (b) void area fraction and void density as a function of true plastic strain.

### 6.2.3 Correlation between crystallographic orientation and damage

Scanning electron micrographs of the etched microstructure showed that damage has occurred at the interface of bainite and martensite (B/M) as discussed in section 5.2.4. This reveals the presence of mechanical phase contrast between B and M, which causes stress (and/or strain) partitioning. This incompatibility at some critical moment when the imposed loads cannot be relaxed anymore by plastic glide, leads to interface tearing or void initiation. In addition, the role of crystallographic orientation on strain (and/or stress) partitioning is inevitable. In this respect, 33 voids have been studied locally by EBSD in order to capture the local surrounding orientations. The selection procedure is schematically represented in figure 6-3. As it is shown in figure 6-3b, an area with sides of approximately 3 times the void diameter was considered as the local environment surrounding a specific void.

Due to severe plastic deformation and distortion in the crystal lattices in the vicinity of the voids, a poor pattern quality was observed. Only orientations with confidence index above 0.1 were retained. Afterwards, the ODF was derived from approximately 131,000 void neighbouring pixels.

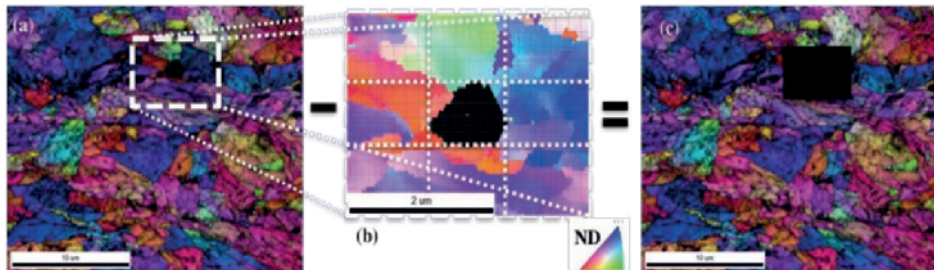


Figure 6-3. Schematic illustration of orientation selection on an overlaid image quality and inverse pole figure map; (a) complete area of analysis, (b) area selected around the void with faces approximately equal to 3 times of a void diameter and (c) remaining area.

The 3D-ODF of voids derived are shown in figure 6-4 and denominated as the Void-ODF (VODF) using the Euler space. Figure 6-4 shows three sections of  $\varphi_2 = 15^\circ$ ,  $45^\circ$  and  $75^\circ$ , which exhibit the dominant components of VODF. On the level of individual voids sample symmetry has to be ignored and thus the Euler space limits are set to  $0 < \varphi_1 < 360^\circ$  and  $0 < \varphi_2 < 90^\circ$  and  $\Phi < 90^\circ$ . Similarly, the texture of the regions without voids, which produces the No-Void-ODF (NVODF), is shown in figure 6-5c. It is expected that regions with no voids have more dispersed orientations compared to regions selected around the voids. Therefore, after merging all of these orientations away from the voids, the No-Void ODF (NVODF) plot reveals smoother distribution.

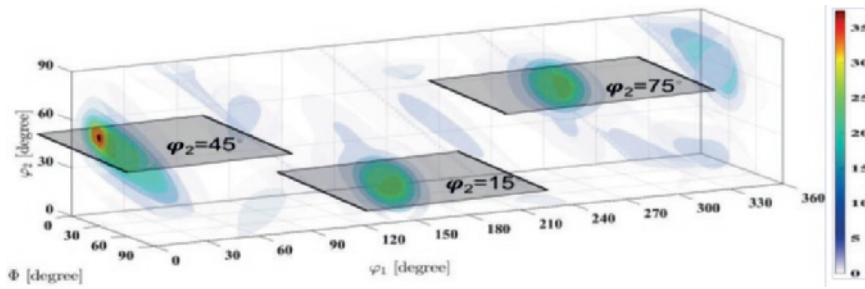


Figure 6-4. 3D void ODF (3D-VODF). Three  $\varphi_2$  sections ( $\varphi_2=15, 45$  and  $75^\circ$ ) consist of the dominant components with regard to voids orientations.

As it was mentioned earlier in section 6.3.2.1, during uniform plastic deformation no microstructural damage has appeared, thus, the deformation texture of the material at the UTS point, cf. Figure 6-5a, can be considered as a reference texture from which voids will be initiated. The uniform texture (UODF) has been derived from the uniform region of the fractured tensile sample. By merging the textures from the void neighbouring grains and the grains away from the voids, the entire texture of the necked region is obtained, i.e. the Neck-ODF, cf. Figure 6-5d. This study is a post-mortem analysis, which implies that all orientations regarding VODF and NVODF were captured after final failure. Moreover, it is not clear which interface was the origin of the damage initiation spot. Consequently, the rectangular region (figure 6-3b) of interest around the voids includes all possible orientations from which the voids might have initiated.

Figure 6-5 shows merely the textures in the  $\varphi_2=45^\circ$  section of the material at two different strain levels, uniform and post uniform, respectively. By visually comparing the VODF and NVODF with respect to the Neck-ODF it is observed that the NVODF closer resembles the texture observed in the necked region (Neck-ODF). Conversely, by visually comparing VODF and NVODF with the uniform texture, it appears that the VODF better resembles the uniform ODF (UODF). In order to further investigate the closeness of the VODF and UODF textures, the contour maps of VODF are overlaid with UODF at the three sections of  $\varphi_2=15, 45$  and  $75^\circ$  which is depicted in figure 6-6. The contour maps overlapped on gradient map of figure 6-6 correspond to VODF while the backgrounds are UODF at identical;  $\varphi_2$  sections. The black arrows are the indications of main components of the VODF.

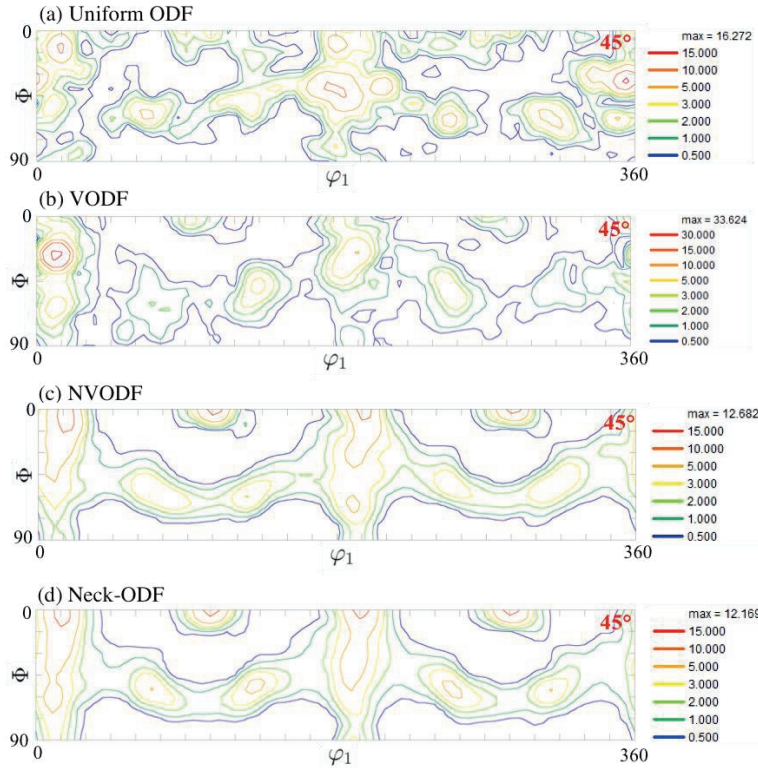


Figure 6-5.  $\varphi_2=45^\circ$  section of ODFs of the material at two different deformation levels; (a) Uniform deformation UODF (calculated from 796000 data points), (b) post uniform VODF (131000 data points), (c) post uniform NVODF (460000 data points) and (d) Necking or post uniform ODF consist of the merged ODFs in b and c.

Figure 6-6 reveals further that at two other sections of  $\varphi_2=15$  and  $75^\circ$ , the VODF resembles closely the UODF as it was shown earlier for  $\varphi_2=45^\circ$ , cf. Figure 6-5a and b. This can be explained by the fact that the local stress relaxation process at a certain moment is occurring by the void initiation rather than by plastic deformation accommodated by dislocation glide. Upon further macroscopic deformation, two micro-mechanisms can dissipate the local stress concentration produced by the presence of a void, i.e. void growth and/or local further plasticity surrounding the initiated void. The results from the comparison between UODF, VODF (see figure 6-6) and Neck-ODF (see figure 6-5) demonstrate that after voids were formed, the local stress dissipation process around voids is rather governed by void growth than local plasticity as the Void-ODF clearly resembles the uniform ODF. However, it is observed that the individual components of VODF and UODF do not exactly correspond one to one

and there are some deviations. Eventually, a void is nothing but a free surface within the microstructure, which may relax the local constraint of the surrounding grains and thus can potentially facilitate the local plastic deformation. However, the competing role of the locally hardening and free surface lead to the final contribution of plasticity and/or void growth on the stress relaxation.

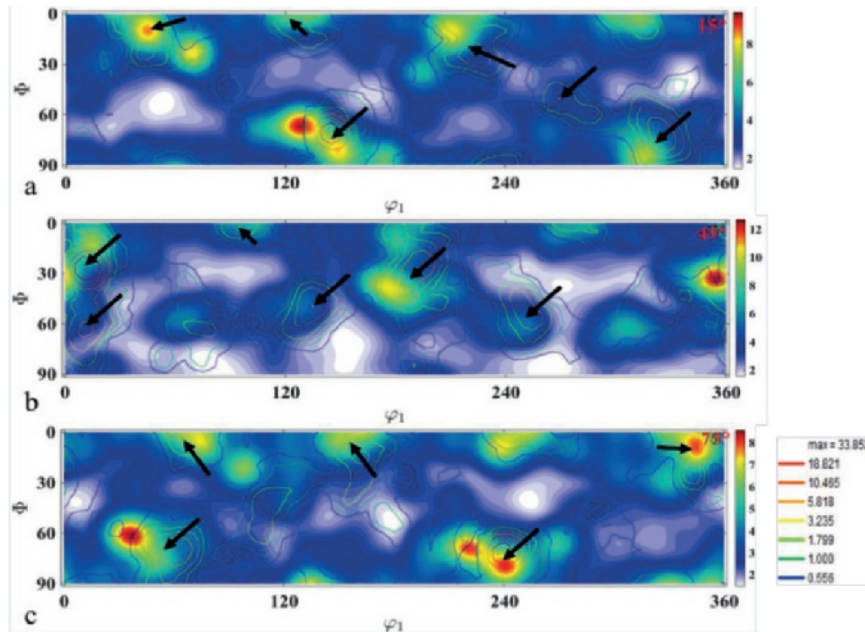


Figure 6-6. The overlapped VODF and UODF of the material at two different deformation levels; (a)  $\varphi_2=15$ , (b)  $\varphi_2=45$ , (c)  $\varphi_2=75^\circ$ .

The three sections of figure 6-4 ( $\varphi_2=15, 45$  and  $75^\circ$ ) consist of dominant orientations where voids are more observed. These components can be considered as susceptible orientations for damage initiation, although this method is a post-mortem analysis. This is due to the fact that VODF resembles UODF, and thus, this implies that upon void initiation, void growth is a prominent mechanism of local stress relaxation compared to further plasticity at surrounding grains. Consequently, the increased macroscopic deformation until failure does not lead to considerable orientation change in VODF components.

## 6.3 Conclusion

A new methodology was examined to address the role of crystallographic orientation on damage initiation. In the necked region of the sample, the microstructure was divided in two parts: (i) the crystallographic orientations of the grains surrounding 33 voids were selected and represented by the Void-ODF, (ii) whereas the regions away from the voids represented the No-Void-ODF (NVODF). It was observed that the VODF more resembles the texture of the uniformly deformed region, outside the necked region. The post mortem crystallographic orientation analysis around voids revealed that after void initiation, the local stress relaxation process is rather controlled by void growth than by further local plastic deformation. In other words, it can be concluded that upon void initiation, orientations around voids may not go through significant rotations. This is due to the fact that the local plastic work is rather dissipated by void growth than rotation of local grains. This can be explained by the hardening saturation process of grains at certain macroscopic strain level due to plasticity prior to damage initiation.

Although, this method is a post-mortem analysis of capturing crystallographic orientations of grains around voids, it can be used as a validation tool for crystal plasticity based models to predict susceptible damage initiation spots in an orientation space.

## References

- [1] E. Ahmad, T. Manzoor, K.L. Ali, J.I. Akhter, Effect of microvoid formation on the tensile properties of dual-phase steel, *J Mater Eng Perform* 9(3) (2000) 306-310.
- [2] G. Avramovic-Cingara, Y. Ososkov, M.K. Jain, D.S. Wilkinson, Effect of martensite distribution on damage behaviour in DP600 dual phase steels, *Mat Sci Eng a-Struct* 516(1-2) (2009) 7-16.
- [3] X.J. He, N. Terao, A. Berghezan, Influence of Martensite Morphology and Its Dispersion on Mechanical-Properties and Fracture Mechanisms of Fe-Mn-C Dual Phase Steels, *Met Sci* 18(7) (1984) 367-373.
- [4] D.L. Steinbrunner, D.K. Matlock, G. Krauss, Void Formation during Tensile Testing of Dual Phase Steels, *Metall Trans A* 19(3) (1988) 579-589.
- [5] C.C. Tasan, M. Diehl, D. Yan, C. Zambaldi, P. Shanthraj, F. Roters, D. Raabe, Integrated experimental-simulation analysis of stress and strain partitioning in multiphase alloys, *Acta Mater* 81 (2014) 386-400.
- [6] C.C. Tasan, J.P.M. Hoefnagels, M. Diehl, D. Yan, F. Roters, D. Raabe, Strain localization and damage in dual phase steels investigated by coupled in-situ deformation experiments and crystal plasticity simulations, *Int J Plasticity* 63 (2014) 198-210.
- [7] C.C. Tasan, J.P.M. Hoefnagels, M.G.D. Geers, Identification of the continuum damage parameter: An experimental challenge in modeling damage evolution, *Acta Mater* 60(8) (2012) 3581-3589.
- [8] D.S. Yan, C.C. Tasan, D. Raabe, High resolution in situ mapping of microstrain and microstructure evolution reveals damage resistance criteria in dual phase steels, *Acta Mater* 96 (2015) 399-409.
- [9] N. Jia, R.L. Peng, Y.D. Wang, G.C. Chai, S. Johansson, G. Wang, P.K. Liaw, Interactions between the phase stress and the grain-orientation-dependent stress in duplex stainless steel during deformation, *Acta Mater* 54(15) (2006) 3907-3916.
- [10] A. Needleman, V. Tvergaard, Comparison of Crystal Plasticity and Isotropic Hardening Predictions for Metal-Matrix Composites, *J Appl Mech-T Asme* 60(1) (1993) 70-76.
- [11] E.E. Nugent, R.B. Calhoun, A. Mortensen, Experimental investigation of stress and strain fields in a ductile matrix surrounding an elastic inclusion, *Acta Mater* 48(7) (2000) 1451-1467.
- [12] R.G. Li, Q.G. Xie, Y.D. Wang, W.J. Liu, M.G. Wang, G.L. Wu, X.W. Li, M.H. Zhang, Z.P. Lu, C. Geng, T. Zhu, Unraveling submicron-scale mechanical heterogeneity by three-dimensional X-ray microdiffraction, *P Natl Acad Sci USA* 115(3) (2018) 483-488.
- [13] T.W.J. de Geus, F. Maresca, R.H.J. Peerlings, M.G.D. Geers, Microscopic plasticity and damage in two-phase steels: On the competing role of crystallography and phase contrast, *Mech Mater* 101 (2016) 147-159.

# Chapter 7 Crystal plasticity based modelling of bainitic/martensitic steels

**Abstract.** In chapter 7, the crystal plasticity based model, ViscoPlastic Self-Consistent (VPSC), is employed for two main purposes. First, to simulate the anisotropic quasi-static and dynamic mechanical responses of the low silicon grade bainitic multiphase steels. To this aim, a physical hardening model is integrated in the frame work of the VPSC model. Microstructural parameters needed for the VPSC simulation such as micro-constituents and their corresponding features (i.e. texture, dislocation density, grain size and aspect ratio) are quantified and given as inputs to the model in order to simulate the flow behaviour of the materials under consideration. The VPSC model with the implemented physical hardening model is shown to be capable to simulate well the flow behavior of the materials under various strain rates and loading directions. Second, the model is employed in order to predict the stress/strain partitioning among the simulated crystallographic orientations (grains), which can enable us to detect damage initiation spots in the Euler space. This new approach, in which it predicts damage initiation locations in the Euler orientation space, is validated by the results derived in chapter 6. Accordingly, this method is developed and can be used further to reveal the importance of crystallographic orientation on damage initiation. In the current study on multiphase bainitic steels, the damage initiation hot spots predicted by VPSC demonstrate that the arised incompatibilities of a particular strain component coincide well with orientations captured around the voids. Therefore, in such a multiphase steel, correlation between crystallographic orientation and damage nucleation is observed.

**Keywords:** crystal plasticity; physical hardening; damage; stress/strain; incompatibility; ODF.

## 7.1 Introduction

In chapter 5 and 6, the topological and crystallographic aspects of damage initiation micro-mechanisms were addressed, respectively. In addition, the impact of microstructural damage on global mechanical response and failure was also addressed specifically in chapter 5.

Generally crystal plasticity models are classified in two main types: (i) homogenization models that calculate the average state for a given crystallographic orientation, as for example the models based on the Taylor-Bishop-Hill theory [1] or the Visco-Plastic Self-Consistent (VPSC) model [2] and (ii) full-field methods, such as CPFEM and CPFFT [3], which provide a solution for every material point, taking into account across the topology of the microstructure.

The capability of crystal plasticity finite element modeling (CPFEM) on local microscale grain-to-grain or phase-to-phase interactions resulted in accurate simulations on the microstructure level in order to understand the micro-mechanical behavior of heterogeneities and their corresponding topological effect during plastic deformation [4, 5]. In a more simplified quasi-3D CPFEM, based on a real 2D microstructure analysis from SEM-EBSD, the significance of the real microstructure and texture on damage and shear banding localization was observed by Kadkhodapour *et al.* [6] and Delannay *et al.* [7]. For dual phase and duplex stainless steels (DSS), CPFEM modeling has been used in a complete 3D simulation from a real microstructure mapping using either through the thickness sectioning EBSD or ion-beam surface milling [8, 9]. In the earlier work on a DP steel, the influence of initial texture on damage initiation, using two different damage criteria, were also observed by comparing isotropic elasto-plastic and crystal plasticity FEM. In the later work, the kinematic stability of the initial microstructure orientation of a DSS was assessed by two parameters: lattice rotation rate and rotation field divergence. The results showed that regions susceptible to ductile failure are strongly dependent on the initial and neighboring orientations. Moreover, it is always a trade-off between 2D and 3D CPFEM simulations from the perspective of computational cost and accuracy of the simulations on grain-scale level interactions and thus comprehensive understanding of micro-mechanisms engaged on initiation of damage. Constructing a 3D finite element mesh to represent the real microstructure heterogeneities (e.g. grain size, phase topology and texture) is a persistent challenge experimentally and computationally. Often, 3D CPFEM constructed from a real mapped microstructure, demands extensive advanced experimental and numerical work, which causes limitations in the number of grains considered for the simulations. It is worth noting that the macroscopic mechanical response of the polycrystalline aggregates is governed by its intrinsic statistical nature. However, understanding the

---

local effects on damage initiation requires local experimental and computationally expensive approaches with the risk of poor statistics. Therefore, the compromise between homogenization and local interaction (full-field) methods leads to different choice in numerical models.

Moreover, initiation of micro-voids is a very local phenomenon, thus, it may seem counterintuitive to use a homogenization model to study damage initiation. However, although the damage process starts in a very small region of the material, the average effect is what will determine material behavior from a macroscopic point of view. If a full-field model was used to study void initiation, the information obtained would only be applicable to a small region of the material with the same topology as the studied Representative Volume Element (RVE). In order to characterize the material, it would be necessary to repeat the simulations with a large number of different RVEs, and later calculate some sort of average with all the obtained results. Eventually, this solution would correspond with the one given by a homogenization model.

In the current chapter, the VPSC model is combined with experimental works reported in previous chapters for two main purposes. First, to predict the flow behavior of the material at quasi-static and dynamic loading conditions and to simulate the anisotropy of the mechanical response. Second, due to the capability of the VPSC model in calculating the stress/strain values at every time step of the simulation, this model is used to find the orientations (grains) with maximum and minimum stress/strain values, which will be referred to as stress/strain incompatibilities. This enables to investigate the role of the crystallographic orientation on micro-mechanical behavior and ductile damage initiation in the bainitic steels containing martensite and carbides as second phase constituents. A new approach is examined to depict these incompatibilities in the crystallographic orientation space. In order to validate the results derived from VPSC, the orientation distribution functions of voids calculated in chapter 6 is employed. Besides, a physically based hardening model [10] is implemented in the visco-plastic self-consistent (VPSC) model in order to evaluate the micro-mechanical response of individual constituents according to their physical microstructural parameters such as composition, crystal orientation, dislocation density, grain size thus stress/strain partitioning between bainite and martensite.

Figure 7-1 shows a diagram of the VPSC model with the most important equations of the model as illustrated earlier in chapter 3.

This chapter is structured as follows: in section 7.2, a general description of material definition and input parameters needed for the VPSC simulation is given. Section 7.3 illustrates the fitting parameters and applied procedures. Results and discussion from the simulations are shown in section 7.4.

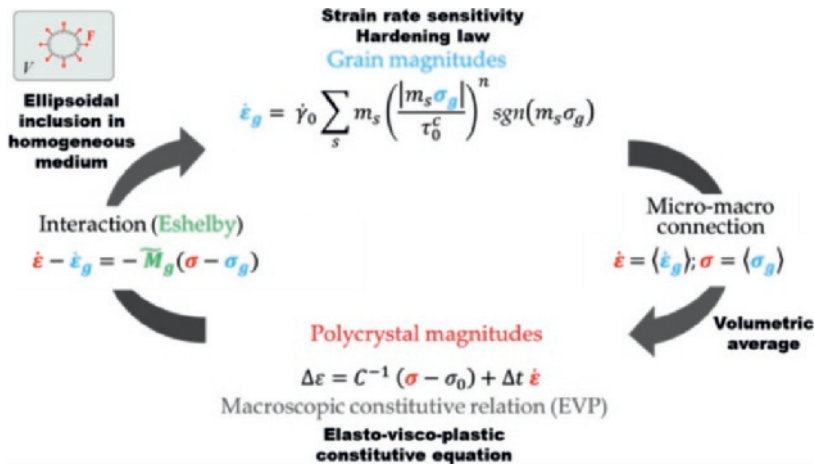


Figure 7-1. VPSC formalism: the behavior of individual grains at the microscopic scale and the whole polycrystal at the macroscopic scale are related by the micro-macro connection and the grain interaction scheme, based on the solution of the Eshelby problem.

## 7.2 Material definition

The first step in order to define a model for the material is to determine the number of phases present in the microstructure. In the current study, the low silicon bainitic multiphase steel is the material to be modelled. Two phases are considered, bainite and martensite. Additionally, the presence of carbides in the microstructure is considered as a barrier for dislocation glide in the hardening model. The fraction of these phases is already discussed in detail in section 4.2.1. Bainite and martensite are the BCC crystal structure phases modelled by VPSC. The input data needed by VPSC are the relative dimensions of the crystallographic cell, the elastic stiffness tensor, and the definitions of the plastic strain modes and their corresponding hardening laws. In addition, microstructural information such as grain shape, crystallographic orientations, volume fraction, lath size and dislocation density of the microstructure constituents at the initial annealed state of the material is required.

### 7.2.1 Mechanical parameters

All the input parameters of VPSC associating to the flow response of the material are referred to the individual grains. These parameters define both the elastic and visco-plastic response of a single crystal.

The elastic response of the polycrystalline aggregate is assumed to be isotropic here. This is an approximation, although it is considered to be valid for the study of plastic deformation. This is due to the fact that the relative significance of elastic strain becomes very small. The Young modulus and Poisson ratio are known from tensile tests, which are 211.9 GPa and 0.29, respectively. Therefore, the elastic stiffness tensor needed by VPSC can be easily calculated with the standard formulation for an isotropic stiffness tensor using Lamé coefficients.

Strain hardening of the material is represented in the VPSC model by a physical hardening law for each of the slip systems that determines the critical shear stress as a function of the accumulated deformation (cf. section 3.7.2.3). The physical hardening model used in the VPSC model is defined by 7 parameters. All these parameters are fitted using static and dynamic tensile tests and the numerical method described in section 7.3.

### 7.2.2 Material texture and microstructural parameters

VPSC simulations require input data specifying the initial grains shape (assumed to be an ellipsoid with an aspect ratio and inclination) and their crystallographic orientation. These data are derived from the EBSD analysis. The texture of the studied materials is shown in figure 7-2 and 7-3. However, in order to provide crystallographic orientations as VPSC input, instead of using the measured textures directly, these data are processed with MTEX software [11]. Considering orthorhombic sample symmetry for annealed cold rolled samples, the ODF corresponding to each phase is calculated from more than 1 million orientations. Later, by using MTEX, approximately 2500 discrete orientations are generated for each phase to be used as crystallographic orientation inputs in VPSC.

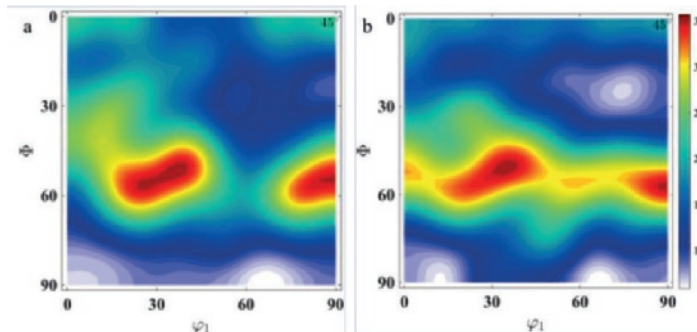


Figure 7-2.  $\varphi_2 = 45^\circ$  section of the orientation distribution function of the HT sample: (a) Bainite and (b) martensite.

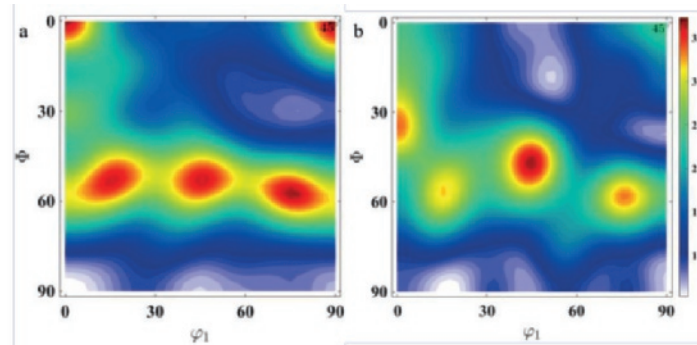


Figure 7-3.  $\varphi_2 = 45^\circ$  section of the orientation distribution function of the LT sample: (a) Bainite and (b) martensite.

There are two possible approaches to consider the grain shape: first, to consider the shape of each grain individually or, second, to assume an average shape for all the grains. The former method requires high computational cost, as the number of Eshelby problems to solve increases proportionally with the number of grains, as explained in section 3.7.2. Figure 7-4 shows the grain properties, which demonstrates a homogeneous shape distribution. Figure 7-4(a) shows a normal distribution in which an average value can be approximated for each grain. Therefore, the aspect ratio of all the grains is calculated using average dimensions given in table 7-1.

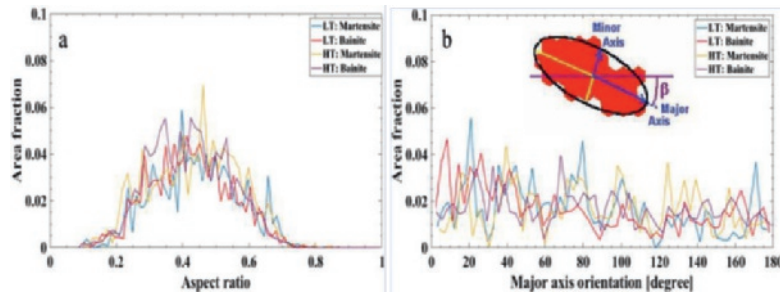


Figure 7-4. Input data needed for the VPSC simulation for both HT and LT samples and their corresponding phases: (a) Grain aspect ratio and (b) Grain inclination with respect to the rolling direction.

Table 7-1 Average grain properties of both phases in the HT and LT samples.

Sample	Phase	Grain shape orientation [degree]	Aspect ratio
HT	Bainite	$84.9 \pm 50.6$	$0.41 \pm 0.12$
	Martensite	$86.9 \pm 46.6$	$0.43 \pm 0.13$
LT	Bainite	$72.4 \pm 53.8$	$0.42 \pm 0.12$
	Martensite	$76.4 \pm 47.5$	$0.44 \pm 0.12$

In addition, microstructural variables of the HT and LT materials are measured as discussed earlier in section 3.4 in chapter 3. The carbon content of the martensite was determined in basis to the nano-hardness measurements, and thus it is 0.28 wt.%. In the case of bainite, the carbon content is calculated based on the heat treatment and it is found to be 0.03 wt.% for both materials. Other microstructural parameters of the HT and LT materials are listed in table 7-2. Dislocation density is measured by EBSD analysis using EDAX-OIM<sup>TM</sup> software.

Table 7-2 Microstructural variables:  $v_f$  is the volume fraction of the phase,  $d$  is the lath size,  $\rho$  dislocation density,  $v_c$  is the volume fraction of carbides and  $d_c$  is the size of carbides.

Sample	Phase	$v_f$ (%)	$d$ ( $\mu\text{m}$ )	$\rho$ ( $\text{m}^{-2}$ )	$v_c$ (%)	$d_c$ ( $\mu\text{m}$ )
HT	Bainite	96.6	1.44	$1.45 \cdot 10^{14}$	3.7	0.07
	Martensite	3.4	0.70	$1.72 \cdot 10^{14}$	0	-
LT	Bainite	97.6	1.17	$1.56 \cdot 10^{14}$	3.2	0.07
	Martensite	2.4	0.60	$1.88 \cdot 10^{14}$	0	-

## 7.3 Fitting of model parameters

All the parameters needed for the VPSC model are derived using either experimental data from quasi-static and dynamic tensile tests of both samples or from literature data. It is important to note that the microstructural parameters of each phase will determine the mechanical response of each constituent phase. The fitting parameters are shared between the two phases of the materials. This reduces the number of fitting parameters and thus computational cost while an accurate fitting between experiments and simulations are observed. The purpose of the fitting process is to determine the set of material parameters that simulates the most similar tensile curves to the ones obtained from experiments. To this purpose, an initial set of parameters is assigned based on literature data. These parameters are listed in table 7-3.

### 7.3.1 Input data

The experimental data used to fit the hardening model parameters are discussed in detail in section 4.2.3 (chapter 4 static and dynamic curves of the HT and LT samples). The quasi-static and dynamic tensile tests of the LT and HT samples used for the fitting are performed at strain rates of  $8 \cdot 10^{-3} \text{ s}^{-1}$  and  $641 \text{ s}^{-1}$ , respectively. In addition, quasi-static curves of the transversal samples, in which their loading directions are parallel to TD, are also used for the fitting process. Therefore, two samples with their corresponding 3 curves (two quasi-static along RD and TD, and one dynamic along RD) are used for the fitting process, which leads to a total of 6 experimental curves as illustrated in section 4.2.2. Eventually, this leads to one set of parameters, which can be used to simulate the LoSi samples under quasi-static and dynamic loading conditions.

The effect of temperature evolution effect is not taken into consideration in the standalone version of VPSC90. Therefore, the dynamic curves used for the fitting are assumed to be isothermal. This assumption is based on geometry of the specimen used at high strain rate tests (GL5), in which this geometry improves the dissipation of heat. Besides, it is shown that the influence of temperature on flow behaviour of steels below  $100^\circ\text{C}$  is negligible [12] and the adiabatic temperature rise in the GL5 specimen prior to the deformation localization is far below  $100^\circ\text{C}$  as shown in table 4-3.

### 7.3.2 Modelling of tensile test

Tensile experiments under static and dynamic loading conditions are simulated using the VPSC model. In order to satisfy the uniaxial loading mode, a particular boundary condition for simulations is imposed, in which stress components in transversal and normal directions are kept to be zero.

### 7.3.3 Fitting procedure

The parameters are fitted in various stages, using different sets of data to fit different parameters, independently or simultaneously, using a method analogous to the one presented by Galan Lopez [13]. The process is partially automatized using a Python script. This script builds input files for VPSC based on experimental data and an input template file (similar to VPSC input files), and calls the standalone version of VPSC90 to perform simulations with variable parameters. Later, it compares the results with experimental data and a least-square algorithm finds a new guess for the parameters that minimises the residual resulting from subtracting simulated and experimental curves parameters. The process is iterative and continues until the solution converges to a minimum. The minimisation method implemented is the Levenberg-Marquardt Algorithm (LMA), that interpolates between the Gauss-Newton algorithm and the method of gradient descent. There are several implementations available for this algorithm. The one used here is the part of `scipy.optimize.leastsq` Python package, which internally uses MINPACK [13].

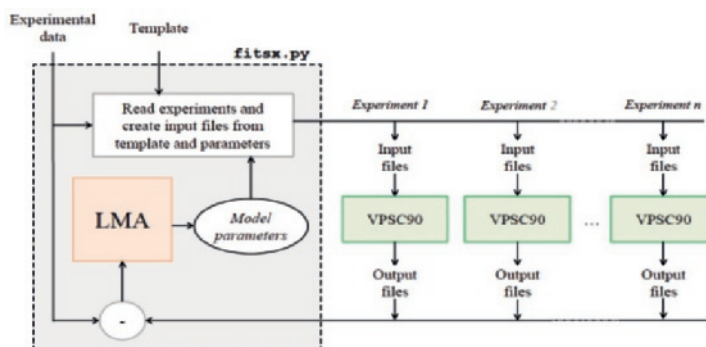


Figure 7-5. Block diagram that shows how the Python script used to fit the material parameters (`fitsx.py`) reads experimental data and a template file to generate input for VPSC based on a guess of the parameters and, after running a VPSC90 simulation for each of the experiments, calculates a new guess for the parameters based on the error between simulated and experimental curves using the Levenberg–Marquardt algorithm [14].

The LMA is effective to find a local minimum. This implies that the method is sensitive to the initial values of the parameters. Therefore, the Python script cannot be used directly to find the desired parameters. Instead, an initial set of parameters is given based on the literature data. Most of the fitting parameters ( $C_1$ ,  $y$ ,  $\beta$ ,  $C_2$  and  $\sigma_{imb}^2$ ) are taken from [15], while the typical value of 0.5 is used for  $\alpha$ , the Hall-Petch constant is set to 10.0 (which is close to the fitted value in [16]),  $C_p$  is set to 2 (which corresponds to cubic particles) and  $n$  is initially considered to be 10.0 (a value typically used in VPSC simulations).  $C_2$  and  $\sigma_{imb}^2$  are related to the stage IV hardening [10] of the flow curve, which is not simulated in the current study, thus, they are not fitted.

### 7.3.4 Deformation mode

In the steels with BCC crystal structure, the main deformation mechanism at the room temperature is by dislocation glide. The two main slip systems are  $12\ \{110\}<111>$  and  $12\ \{112\}<111>$  systems. In total these systems provide 24 variants of crystallographic planes and directions. In the current study, the latent hardening influence is implemented in the physical hardening model as illustrated in equation (28) section 3.7.2.3. This is related to the occurrence of hardening in one slip plane as a result of the slip activity on another slip plane. It should be mentioned that, latent hardening is merely considered for the two slip systems of  $\{110\}<111>$  and  $\{112\}<111>$ . For different combinations of interaction between the slip systems the values are taken from the literature [17].

## 7.4 Results and discussion

The final set of fitted parameters obtained is shown in table 7-3. These parameters are used to model both the HT and LT samples. This is due to the fact that both samples have similar compositions and crystal structure, thus, composition related constant ( $C_1$ ) is expected to be similar. In addition, as the only difference between both samples is their austenization temperature, it is assumed that other fitting parameters do not vary from one sample to another. Alternatively, any microstructural parameters such as dislocation density, grain size, phase fractions and textures are the varying parameters considered for each sample separately. Moreover, table 7-4 lists the latent hardening coefficients used in equation (28) section 3.7.2.3 [17].

Table 7-3. Fitted parameters in VPSC for both LT and HT samples (R-square = 0.96) except  $C_2$  and  $\sigma_{imb}^2$ , which were taken from [10].

Parameters [units]	Description	Value
$C_1$	Constant related to the yield point	2.59
$K_{hp}$	related to the strength of cell boundaries	9.83
$\alpha$	Depends on dislocation structure	0.152
$y$ [nm]	Annihilation distance	6.55
$\beta$	Related to dislocation structure	47.90
$C_p$	Carbide shape	1.53
$n$	Strain rate component of VPSC	10.60
$C_2$ [ $\mu\text{m}^2$ ]	Constant related to incidental necessary boundaries	0.016
$\sigma_{imb}^2$ [ $\mu\text{m}^2$ ]	Constant related to geometrically necessary boundaries	0.255

Table 7-4. Latent hardening coefficients.

$a_{ss'}$	$\{110\} <111>$	$\{112\} <111>$
$\{110\} <111>$	3.0	5.2
$\{112\} <111>$	5.2	5.1

### 7.4.1 Mechanical response under static and dynamic loading conditions

Figure 7-6 (a and b) shows the tensile curves obtained from simulations, and their associated experimental curves, of both the LT and HT samples. A very good fitting between experiments and simulated curves is seen for both materials under quasi-static and dynamic loading conditions. The anisotropy of the quasi-static flow curves is also simulated well in both samples. There is a pronounced scatter in experimental data points of the HT sample loaded along TD (see figure 7-6b). This is in fact the scatter from two repetitions of the tensile test, and this experimental scatter is even higher than the fitting accuracy between experiments and simulations. The model is able to capture the strain hardening and strain rate sensitivity of the materials. In addition, the model can predict well the anisotropy of the flow curves under the quasi-static loading condition. For instance, in the LT sample the quasi-static flow curves along RD and TD are almost identical and this is well predicted by the simulation curves. Similarly, in the HT sample the anisotropy of the flow curves is well captured by the simulations, although the experimental curves demonstrate a pronounced anisotropic tensile behaviour.

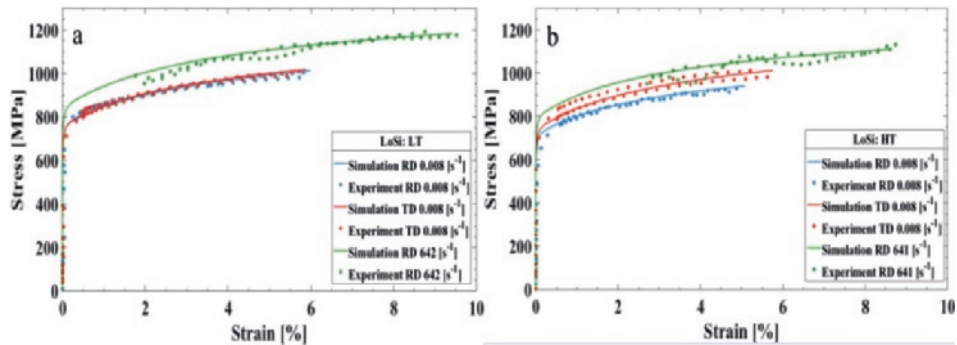
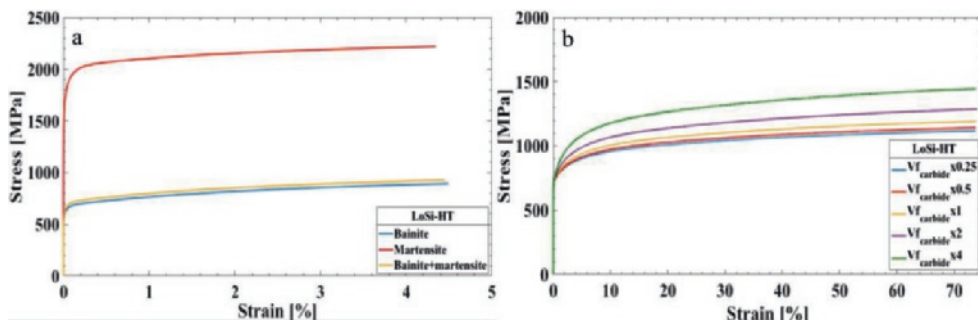


Figure 7-6. Comparison of the flow response between experiments and simulations: (a) The LT sample and (b) The HT sample. Data points demonstrate the experimental curves and lines are simulated curves at low (LD// RD and TD) and high strain rates (LD//RD).

#### 7.4.2 Model sensitivity to microstructural variables

The individual flow response of bainite and martensite considering their corresponding microstructural variables quantified by SEM-EBSD (see table 7-1 and 7-2) is simulated for the HT sample. In addition, in order to evaluate the sensitivity of the model to microstructural variables such as grain size, dislocation density (Geometrically Necessary Dislocations) and carbide volume fraction, various simulations are performed by varying these variables. Results obtained from simulations are shown in figure 7-7.



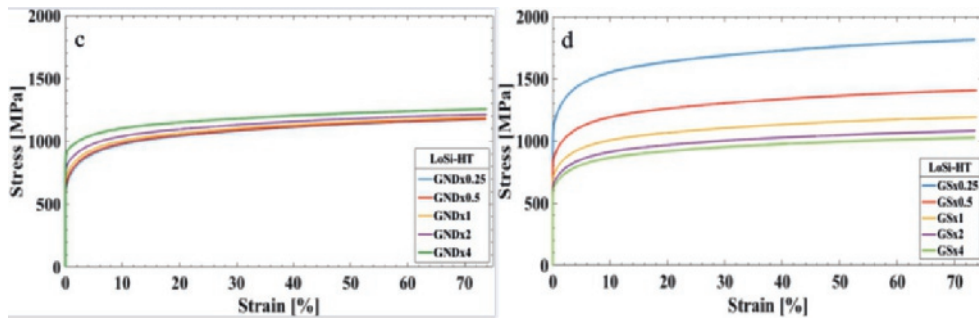


Figure 7-7 Model sensitivity evaluation: (a) individual flow response of bainite and martensite, (b) influence of carbide volume fraction, (c) influence of GNDs and (d) grain size<sup>4</sup> effect.

Figure 7-7(a) demonstrates the individual response of bainite and martensite, in which martensite, as a stronger phase, has approximately 3 times higher strength at identical strain levels compared to bainite. The yellow line reveals the flow response of the real fractions of both constituents (B: 0.966 and M: 0.034) in the HT sample. The individual mechanical response of bainite and martensite are in a good agreement with the experimental curves observed by Tasan *et al.* [18] using nano-indentation integrated with CPFEM simulations.

Figure 7-7(b, c and d) shows the sensitivity of the model to microstructural variables. In figure 7-7(b), the volume fraction of carbides is changed by different factors, where increasing the carbide volume fraction (the effect is equivalent to reducing carbide size as shown in equation (30) of section 3.7.2.3) resulted in strengthening of the material through the generally known process of precipitation hardening and decreasing its volume fraction led to softening. It is also seen that the strain hardening response of the material slightly changes by varying the carbide volume fraction. It is worth noting that Figure 7-7(c) shows the effect of GND density on flow behaviour of the HT sample. The yield point is directly affected by the density of GNDs, in which the higher is the density of dislocations, the stronger the material becomes. The hardening behaviour is not significantly affected by the dislocation density. The softening and strengthening of the material by lowering the dislocation density is not a linear behaviour. The influence of lath size as one of the parameters involved in the model is evaluated in the figure 7-7(d), where lath size inversely shifts the yield point, nevertheless, the hardening behaviour also affected.

<sup>4</sup> Grain size refers to lath width size in equation (30) of section 3.7.2.3.

### 7.4.3 Damage prediction

In previous sections, the VPSC model was used to simulate the mechanical behaviour of the materials under static and dynamic loading conditions. Nevertheless, this model can further be used for texture and also damage prediction at different strain levels. The boundary conditions of tensile tests needed to be imposed in the model. The uniaxial tensile test has particular constraint in which it mainly consists of a macroscopic stress with a principal stress component along the tensile direction. This component is the only non-zero component.

The above boundary condition is valid until the uniform elongation region of a tensile curve. At the onset of necking the stress mode and stress triaxiality change. In the current study, it is assumed that deformation is uniform during the whole test. As mentioned earlier in section 6.2.2 of chapter 6, damage only initiates at the terminal stage of deformation prior to final fracture. Besides, it is important to note that the prediction of susceptible orientations for damage initiation, as a result of stress/strain incompatibilities, should be present first in the experimentally derived deformation texture at the certain macroscopic strain level. Therefore, prior to employing the VPSC model to predict damage initiation sites, it is important to validate the texture predicted by the VPSC model using experimentally derived textures. Figure 7-8(a and b) illustrates the experimental and predicted texture at 5% of tensile deformation, respectively. Similarly, figure 7-9 shows, as in figure 7-8, the experimental and simulated textures at the strain level of 75% in the neck region at the point where damage initiates (see section 6.2.2). The simulated and experimental textures in both figures (cf. fig.7-8 and 7-9) are relatively in a good correspondence. Considering the main components of textures at 5% and 75% deformations, the simulated and experimental textures at 5% are in a better agreement compared to the 75%. In figure 7-8, the main components of the experimental and simulated ODFs correlate one to one. At higher strain levels (cf. figure 7-9), the main components do not correlate well. This may be attributed to the possible difference in strain levels of the experimental and simulated ODFs, and also the different stress mode in the necking region. Eventually, for damage prediction, the texture predicted by VPSC, in which damage initiates is good enough, although the assumed boundary condition for the simulation at this strain level is not completely met due to the necking phenomenon.

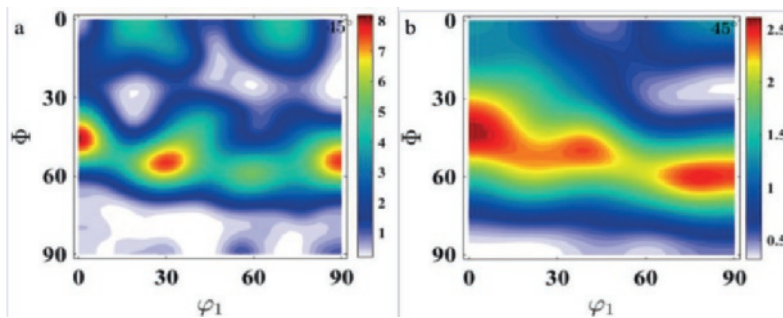


Figure 7-8. Orientation distribution function  $\varphi_2 = 45^\circ$  of the HT sample: (a) texture calculated from interrupted tensile sample at 5% deformation and (b) simulated texture by VPSC at the similar strain level.

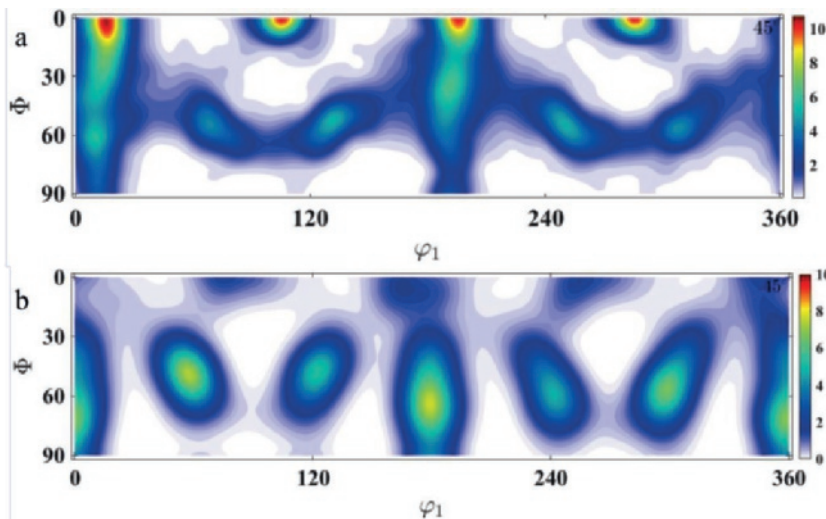


Figure 7-9. Orientation distribution function  $\varphi_2 = 45^\circ$  of the HT sample: (a) texture calculated from the neck region of the fractured tensile sample and (b) simulated texture by VPSC at the strain level 75%.

Damage has been investigated vastly by advanced characterization techniques and CPFEM models [18-20]. As explained earlier in section 7.1, although a 3D microstructure can represent accurately the real character of a material microstructure (e.g. grain size, phases topology and texture) as a RVE, in CPFEM simulations, damage is most often studied in 2D. This is due to the computational efficiency of 2D compared to 3D and also extensive experimental works required to build a 3D microstructure. In CPFEM models damage initiation sites are visualized at microstructural heterogeneities (e.g. at the interface of soft and hard phases) generated by a real or virtual RVE, where stress/strain partitioning occurs.

In a generic concept, the mechanisms leading to stress/strain partitioning in multiphase crystalline materials, as discussed earlier in chapter 2 sections 2.3.1 and 2.3.2, are phase contrast and crystallographic orientation. Normally, the phase contrast (*i.e.* mechanical contrast between two phases) or/and topological mechanism is more emphasized in many research works [21-23]. In the current study, a new method to visualize and study the role of crystallographic orientation in damage initiation is examined by the VPSC model. In fact, the model generates, at the desired time increments, texture files that include the values of each of the stress and strain components for each of the crystal orientations of the phases considered in the simulations. Since the value of each component will depend on crystallographic orientation, it is feasible to represent this information in Euler space. Moreover, the role of phase contrast is also considered using the hardening model introduced in section 3.7.2.3. Eventually, orientations susceptible to damage initiation are represented in the Euler space and validated by experimental results reported in chapter 6 section 6.2.3.

As illustrated above, in the VPSC model, assuming the boundary condition of uniaxial loading, all 6 components of stress and strain are calculated for each grain at each time increment of a simulation. In order to visualize stress/strain components in the Euler space some considerations need to be clarified. First, it is needed to choose an appropriate stress/strain component to study the incompatibilities between all simulated grains. In order to do this, all the components of stress/strain are analysed to find the one with the maximum difference between all the grains in both phases.

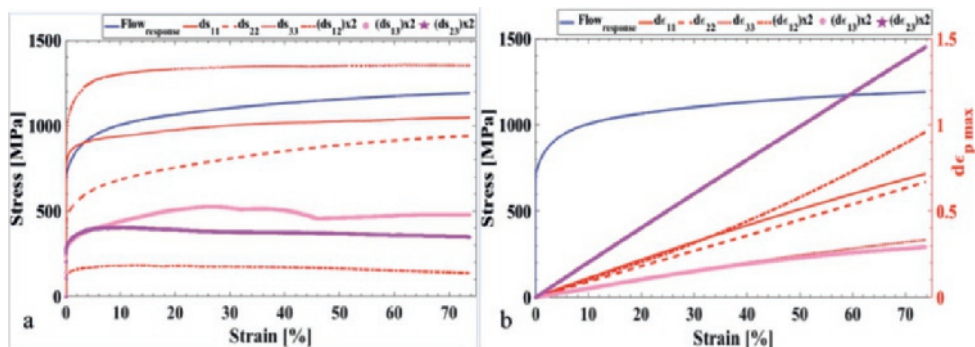


Figure 7-10. Evolution of maximum difference of strain and stress components ( $d\epsilon_{ij}$  and  $d\sigma_{ij}$ ) during the tensile test of HT sample until 75% of deformation: (a) stress components and (b) strain components. The blue curve demonstrates the true tensile curve of HT sample.

Figure 7-10 demonstrates the maximum difference for each of the components of the strain and stress tensors (e.g.  $s_{11}$  component along RD//loading direction) between two grains of any phase with respect to macroscopic true strain in the longitudinal direction of the sample. The stress and strain components of  $s_{33}$  and  $\varepsilon_{23}$  are the ones with the highest differences ( $ds$  and/or  $d\varepsilon$ ) among other components. Therefore, these two components are chosen in order to assess stress and strain maps in the Euler space. This enables to study stress/strain incompatibilities; thereafter, and thus it is possible to predict orientations, in which damage may initiate.

Second, the number of orientations used for the simulation of bainite and martensite are 2460 and 2487, respectively. Third, as discussed in section 6.2.3, three sections ( $\varphi_2 = 15, 45$  and  $75^\circ$ ) of the Euler space are used to visualize damage. This is due to the fact that these three sections have the main components with regard to orientations captured around voids. Therefore, similar sections of stress and strain maps are chosen to study the stress and strain maps derived from the VPSC model.

All the output orientations from the simulation are post-processed in Matlab<sup>®</sup>. A Matlab script is employed to visualize the VPSC output orientations. On the level of sample, triclinic symmetry is assumed due to the fact that damage has been only detected in the necking part of tensile samples, where no sample symmetry is observed. On the crystal level, cubic symmetry is considered. As a result of these symmetries, the orientation space is confined to  $0 < \varphi_1 < 360^\circ$  and  $0 < \varphi_2 < 90^\circ$  and  $0 < \Phi < 90^\circ$ . This orientation space is discretized in volume elements of  $dg = 5^\circ \cdot 5^\circ \cdot 5^\circ$  which results in 23,328 ideal orientations (i.e.  $\varphi_1 = 72 \cdot d\varphi_1$ ,  $\Phi = 18 \cdot d\Phi$  and  $\varphi_2 = 18 \cdot d\varphi_2$ ). In order to find the orientation correspondence of a simulated grain with its ideal counterpart generated by discretization of Euler space, a misorientation threshold (distance) of  $15^\circ$  is considered. In other words, a measured orientation  $j$  belongs to the ideal orientation  $i$  only if its misorientation angle is less than  $15^\circ$ . In order to find the closest representative of a simulated grain, all the misorientations between a simulated orientation and  $n$  ideal orientations are calculated and the one with minimum distance is taken. Accordingly, in the Euler space defined earlier, knowing the above-mentioned symmetries, an orientation may have 3 possible equivalent representation, and thus they are generated by the 3 transformations of each orientation.

After assigning each VPSC simulated orientation to an ideal orientation and its corresponding equivalents, every simulated orientation have specific set of output orientations along with values of strain and stress components. Eventually, stress and strain values plotted in the Euler space are found for every simulated orientation by taking the weighted average value from all VPSC simulated orientations which may belong to a volume element of  $dg$ .

Following the above explanation regarding the method used to visualize stress and strain components in the Euler space, figure 7-11 shows the  $\varepsilon_{23}$  component map at three different sections of  $\varphi_2 = 15, 45$  and  $75^\circ$  overlaid with the contour map of the Void-ODF (VODF), cf. section 6.2.3. The major components of VODF are indicated by the arrows, where often they coincide with either minimum or maximum values of the strain component.

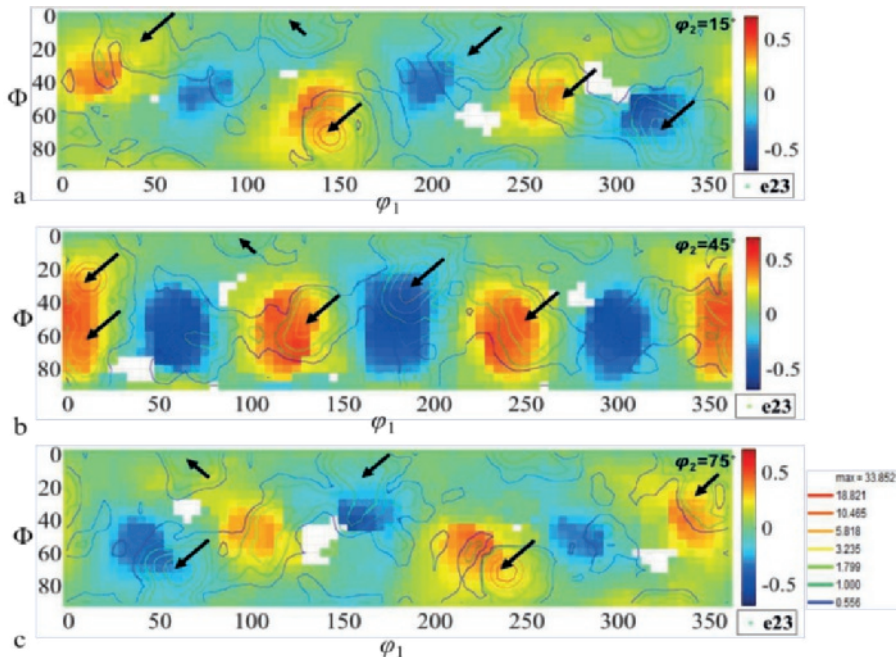


Figure 7-11. The  $\varepsilon_{23}$  component maps at three different sections overlaid with VODF derived from section 6.2.3: (a)  $\varphi_2 = 15^\circ$ , (b)  $\varphi_2 = 45^\circ$  and (c)  $\varphi_2 = 75^\circ$ . The VODF intensity lines are depicted at (c).

Besides the  $\varepsilon_{23}$  component map, it is possible to calculate the equivalent von Mises strain by the following expression [24]:

$$\varepsilon_{eq \ von \ Mises} = \frac{1}{1+\nu} \cdot \sqrt{\frac{1}{2}[(\varepsilon_{11} - \varepsilon_{22})^2 + (\varepsilon_{22} - \varepsilon_{33})^2 + (\varepsilon_{33} - \varepsilon_{11})^2]}$$

where  $\nu$  is the Poisson's ratio, and  $\varepsilon_{11}$ ,  $\varepsilon_{22}$  and  $\varepsilon_{33}$  are the principal components of the strain tensor. Figure 7-12 demonstrates the equivalent von Mises strain map overlaid with the VODF. It is observed

that there is no direct correspondence between highly damaged orientations in the VODF contour map and orientations with maximum and minimum equivalent strain value. However, orientations with lower strain values are less frequent in the VODF. For instance, it is clearly observed that damage is taking place more frequently in the grains that are deformed at least more than 0.45.

Figure 7-13 illustrates the  $s_{33}$  component map similarly at three different sections as in figure 7-11 and 7-12. The main texture components of VODF are mostly located at low stress magnitudes of -200 MPa while few components are also observed at relatively high stress levels between -600 and -800 MPa. It is apparent that VODF does not completely coincide with the maximum and minimum stress levels.

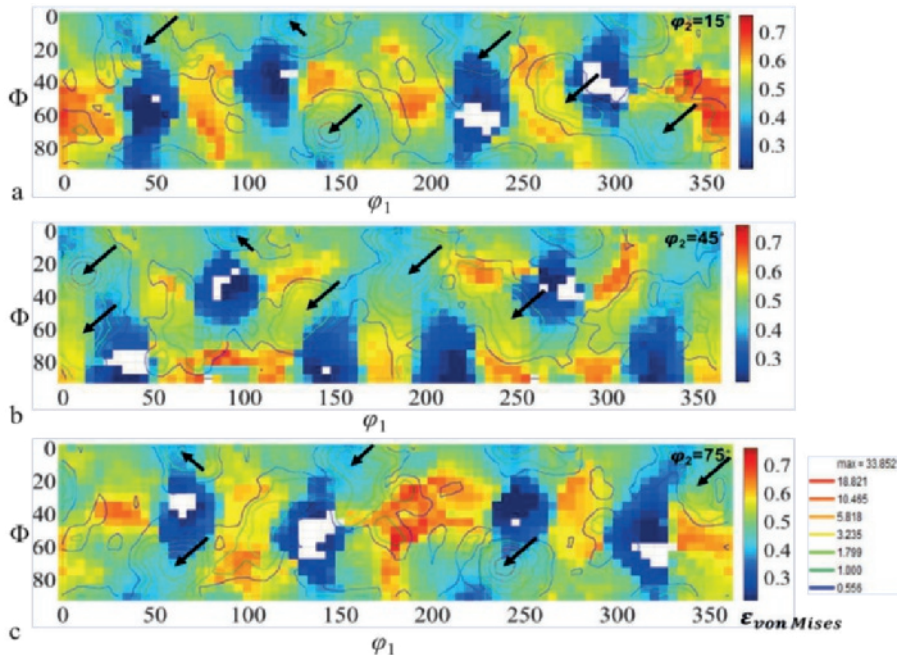


Figure 7-12. The  $\varepsilon_{\text{von Mises}}$  maps at three different sections overlaid with VODF derived from section 6.2.3: (a)  $\varphi_2=15^\circ$ , (b)  $\varphi_2=45^\circ$  and (c)  $\varphi_2=75^\circ$ . The VODF intensity lines are depicted at (c).

Overall, among all the three stress and strain maps (cf. fig 7-11, 7-12 and 7-13), Figure 7-11 demonstrates the best correspondence to the VODF. This may explain the fact that for damage to initiate, the magnitude of equivalent strain in each grain cannot be essentially enough, but also the stress or strain components as directional (vector-based) parameters are also needed to be studied. In particular, the  $\varepsilon_{23}$  component, which demonstrates the highest difference between all orientations

compared to other components (cf. fig 7-10b) can act as a significant strain incompatibility component for damage initiation. Nevertheless, it should be noted that the VODF is a result of a post-mortem analysis (fracture strain  $\approx 112\%$ ), which implies that all orientations are captured after the failure of the material. Therefore, the strain level at which the VODF was calculated may not be exactly the same as in the VPSC simulation (75%). Therefore, the different local strain levels between VPSC simulation and experiment (VODF) can affect the correspondence of the VODF main components with either maximum and minimum values of strain/stress maps derived from the VPSC simulation (cf. fig 7-10, 7-11 and 7-12). In addition, the experimental and simulated textures are not completely identical at the strain level of 75%. Therefore, this may indicate as another factor influencing the correspondence of the VODF components with the maximum and/or minimum of stress/strain maps derived from the simulation.

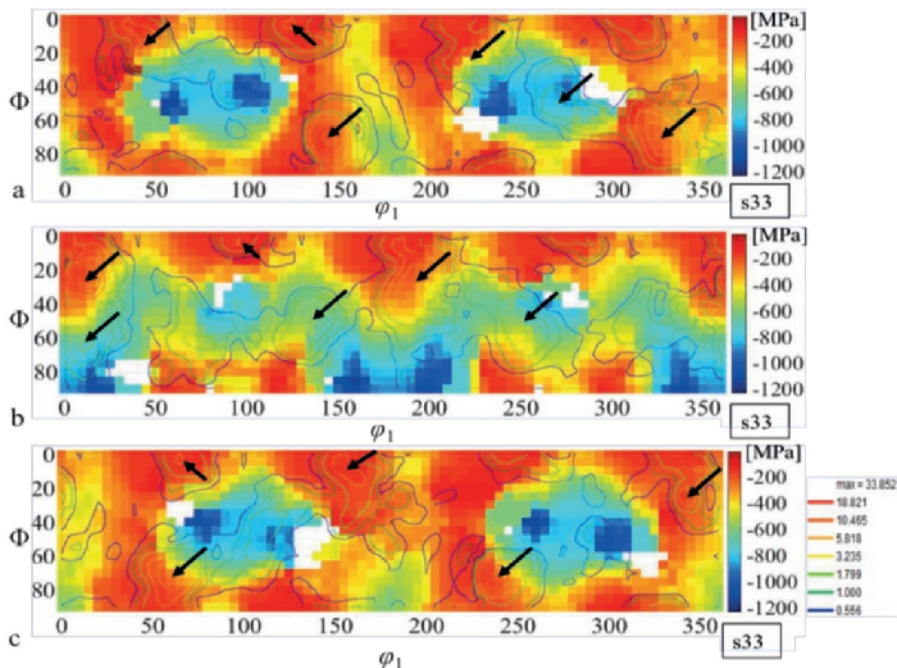


Figure 7-13. The  $s_{33}$  maps at three different sections overlaid with VODF derived from section 6.2.3: (a)  $\varphi_2=15^\circ$ , (b)  $\varphi_2=45^\circ$  and (c)  $\varphi_2=75^\circ$ . The VODF intensity lines are depicted at (c).

## 7.5 Conclusion

In this chapter, the VPSC model was employed to simulate the flow behaviour of two low silicon bainitic/martensitic steels. With one set of fitting parameters, the model was capable to predict the mechanical response of the steels under various strain rates and loading directions. In addition, based on the assumed uniaxial loading boundary condition, the predicted textures at uniform and post uniform strain levels were satisfactory enough. The predicted textures enable to use the model to evaluate the grains' stress/strain levels for the damage prediction. It is important to note that for visualization of susceptible damage initiation sites, the orientation space was chosen due to the fact that the role of crystallographic orientation in damage initiation micro-mechanisms is an important subject, which most often has its own experimental and modelling limitations to be studied. In this particular way of representation, it is possible to study the susceptible damage initiation in the orientation space which can help to study the role of crystallographic orientation in damage initiation. Eventually, two components of  $\varepsilon_{23}$  and  $s_{33}$ , and the von Mises strain were used to study the stress/strain incompatibilities leading to damage initiation. It was shown that  $\varepsilon_{23}$  components coincide well with the VODF which can indicate the importance of this component in nucleation of voids under the uniaxial loading condition.

In order to separately study the susceptible orientations in which their anisotropic deformation behavior leads to damage initiation, it is better to employ this method on a single-phase material. This is due to the fact that microstructural constituents, as micro-mechanical heterogeneities, can blur the effect of crystallographic orientation in damage initiation by partitioning stress/strain between soft and hard phases. The blurring effect is dependent on the mechanical contrast between soft and hard phases and the topology of the hard phase. Moreover, in the current study the uniaxial boundary condition is a farfetched assumption in the necking region. The evolution of stress triaxiality during deformation localization of tensile sample changes the boundary condition of simulation, and thus this can have an impact on the current damage prediction results. Therefore, in the future studies this can be further improved.

Although the complementary usage of the EBSD technique and homogenization crystal plasticity models are well known by the scientific community, its combination as a method to study crystallographically resolved damage initiation had not been used before. The results of this study show that the method is promising and can be successfully used to perform predictions of damage initiation sites in a crystallographic orientation space. However, the interpretation of the results obtained in order

to predict accurately when and how damage will initiate is not an obvious task. Nevertheless, it is expected that with further work and applying the method to other materials and different conditions, it will be possible to refine the method and even develop some damage criterion that can easily be applied in industrial applications.

In the end, this new approach can be used further as a tool to investigate the correlation between crystallographic orientations and damage initiation in various polycrystalline metals.

## References

- [1] P. Van Houtte, S.Y. Li, M. Seefeldt, L. Delannay, Deformation texture prediction: from the Taylor model to the advanced Lamel model, *Int J Plasticity* 21(3) (2005) 589-624.
- [2] R.A. Lebensohn, C.N. Tome, A Self-Consistent Anisotropic Approach for the Simulation of Plastic-Deformation and Texture Development of Polycrystals - Application to Zirconium Alloys, *Acta Metallurgica Et Materialia* 41(9) (1993) 2611-2624.
- [3] F. Roters, P. Eisenlohr, L. Hantcherli, D.D. Tjahjanto, T.R. Bieler, D. Raabe, Overview of constitutive laws, kinematics, homogenization and multiscale methods in crystal plasticity finite-element modeling: Theory, experiments, applications, *Acta Mater* 58(4) (2010) 1152-1211.
- [4] L. Delannay, P.J. Jacques, S.R. Kalidindi, Finite element modeling of crystal plasticity with grains shaped as truncated octahedrons, *Int J Plasticity* 22(10) (2006) 1879-1898.
- [5] O. Diard, S. Leclercq, G. Rousselier, G. Cailletaud, Evaluation of finite element based analysis of 3D multicrystalline aggregates plasticity - Application to crystal plasticity model identification and the study of stress and strain fields near grain boundaries, *Int J Plasticity* 21(4) (2005) 691-722.
- [6] J. Kadkhodapour, A. Butz, S. Ziae-Rad, S. Schmauder, A micro mechanical study on failure initiation of dual phase steels under tension using single crystal plasticity model, *Int J Plasticity* 27(7) (2011) 1103-1125.
- [7] L. Delannay, M.A. Melchior, A.K. Kanjrala, P. Van Houtte, J.W. Signorelli, Cpfem Investigation of the Effect of Grain Shape on the Planar Anisotropy and the Shear Banding of Textured Metal Sheets, *Ceram Trans* 201 (2009) 745-+.
- [8] S.H. Choi, E.Y. Kim, W. Woo, S.H. Han, J.H. Kwak, The effect of crystallographic orientation on the micromechanical deformation and failure behaviors of DP980 steel during uniaxial tension, *Int J Plasticity* 45 (2013) 85-102.
- [9] C.U. Jeong, W. Woo, J.Y. Choi, S.H. Choi, Effect of kinematic stability of initial orientation on deformation heterogeneity and ductile failure in duplex stainless steel during uniaxial tension, *Acta Mater* 67 (2014) 21-31.
- [10] W. Pantleon, Stage IV work-hardening related to disorientations in dislocation structures, *Mat Sci Eng a-Struct* 387 (2004) 257-261.
- [11] R.H.a.H.S. F. Bachmann, Texture Analysis with MTEX – Free and Open Source Software Toolbox Solid State Phenomena 160 (2010) 63-68.
- [12] J. Bouquerel, Y.p. Houbaert, P.p. Verleysen, Modelling and characterisation of multiphase TRIP steel under static and dynamic loading, Ghent university 2008.
- [13] J. Galan Lopez, Crystal plasticity based modelling of the strain rate dependent mechanical behaviour of Ti-6Al-4V, Ghent University. Faculty of Engineering and Architecture, Ghent, Belgium, 2014.
- [14] J.G. Lopez, Crystal plasticity based modelling of the strain rate dependent mechanical behaviour of Ti-6Al-4V, Ingenieurswetenschappen en Architectuur, Ghent university, Ghent, 2013 - 2014.
- [15] O. Leon-Garcia, Micromechanisms of Failure under Static Loading in Sheet Metals for Automotive Applications, Technische Univeriteit Delft, Delft, 2013.
- [16] K.Y. Zhu, O. Bouaziz, C. Oberbillig, M.X. Huang, An approach to define the effective lath size controlling yield strength of bainite, *Mat Sci Eng a-Struct* 527(24-25) (2010) 6614-6619.
- [17] P. Franciosi, Glide Mechanisms in Bcc Crystals - an Investigation of the Case of Alpha-Iron through Multislip and Latent Hardening Tests, *Acta Metall Mater* 31(9) (1983) 1331-1342.
- [18] C.C. Tasan, M. Diehl, D. Yan, C. Zambaldi, P. Shanthraj, F. Roters, D. Raabe, Integrated experimental-simulation analysis of stress and strain partitioning in multiphase alloys, *Acta Mater* 81 (2014) 386-400.
- [19] N. Fujita, N. Ishikawa, F. Roters, C.C. Tasan, D. Raabe, Experimental-numerical study on strain and stress partitioning in bainitic steels with martensite-austenite constituents, *Int J Plasticity* 104 (2018) 39-53.
- [20] C.C. Tasan, J.P.M. Hoefnagels, M. Diehl, D. Yan, F. Roters, D. Raabe, Strain localization and damage in dual phase steels investigated by coupled in-situ deformation experiments and crystal plasticity simulations, *Int J Plasticity* 63 (2014) 198-210.
- [21] T.W.J. de Geus, R.H.J. Peerlings, M.G.D. Geers, Fracture in multi-phase materials: Why some microstructures are more critical than others, *Engineering Fracture Mechanics* 169 (2017) 354-370.
- [22] T.W.J. de Geus, F. Maresca, R.H.J. Peerlings, M.G.D. Geers, Microscopic plasticity and damage in two-phase steels: On the competing role of crystallography and phase contrast, *Mech Mater* 101 (2016) 147-159.
- [23] T.W.J. de Geus, R.H.J. Peerlings, M.G.D. Geers, Microstructural topology effects on the onset of ductile failure in multi-phase materials - A systematic computational approach, *Int J Solids Struct* 67-68 (2015) 326-339.
- [24] G.M. DF Socie, Multiaxial fatigue, Society of Automotive Engineers, Warrendale, PA, 2000.



# Chapter 8 Conclusion

## 8.1 Abstract

Bainitic multiphase steels, belonging to the third generation of advanced high strength steels, have relatively more homogeneous microstructure (*i.e.* less mechanical contrast between matrix and second phase constituents) among high yield stress 800-1000 MPa steel grades. Their enhanced ductility through stabilization of the austenite phase at room temperature with satisfactory high strength made these steel grades good candidates for various automotive components such as car body panels and crash-related components. Deeper understanding of micro-mechanical behaviour of such a multiphase complex steel is of crucial importance to improve the mechanical response of the final component under various loading conditions. For instance, it was reported in chapter 4 that the mechanical performance of such a multiphase steel under the high strain rate deformation was improved. Therefore, these steels demonstrate an enhanced energy absorption during a crash event and also improved formability due to the delay in deformation localization under high strain rate deformations. In addition, investigating failure micro-mechanisms is essential because it is important to predict the failure limit of the material during a forming operation. Accordingly, this is possible by a better understanding of mechanical behaviour of micro-constituents and their topological effect, as they control the strain localization and eventually the global fracture behaviour of the material. Based on the knowledge derived from such an investigation, the optimization of the microstructure is feasible leading to better forming capacity and also fracture resistivity. In this context, the objective of the current thesis was first to study the performance of bainitic multiphase steels under quasi-static and dynamic loading conditions, and second to understand the micro-mechanisms of failure in such a multiphase steel. Therefore, in chapter 4, the quasi-static and dynamic mechanical response of the bainitic multiphase steels were investigated. In chapters 5 and 6 the micro-mechanisms of damage initiation and plastic work dissipation were addressed. Chapter 5 focuses on the role of second phase constituents and their topology (*i.e.* size, shape and distribution) in damage nucleation, whereas, chapter 6 proposes a crystallographically resolved approach to reveal the correlation between crystallographic orientations and damage, and thus the dominant mechanism of plastic work dissipation around the nucleated voids. Eventually, the VPSC model with its physical hardening law was employed in chapter 7 to model the anisotropic flow behaviour of such a multiphase steel at various strain rates. In addition, the model was used to predict

damage initiation sites in the Euler orientation space based on the stress/strain incompatibilities created during plastic deformation among all the simulated grains and phases.

## 8.2 Summary

The quasi-static and dynamic mechanical response of bainitic multiphase steel were studied. Positive strain rate sensitivity was observed for the all bainitic steels under consideration in this thesis. It was shown that tensile properties (both strength and ductility) were increased at high strain rates resulting in improvement of energy absorption. It was shown that the presence of second phase constituents decrease the strain rate sensitivity. Besides, it was demonstrated that the finer microstructure exhibits the lower strain rate sensitivity. Moreover, a comprehensive literature survey on various steel grades in chapter 4 revealed that steels with higher strength demonstrate lower strain rate sensitivity. This correlation was approximated by a power law function, in which the strain rate sensitivity factor of the Johnson-Cook model is correlated to the yield stress at the reference strain rate (quasi-static).

*Therefore, any microstructural strengthening mechanisms in steels can decrease the strain rate sensitivity. A power law function can approximate the correlation between the yield strength and the strain rate sensitivity of the Johnson-Cook model.*

Many studies have been conducted by advanced characterization and modelling techniques on first generation advanced high strength steels to understand the damage initiation micro-mechanisms. This has led to a good understanding on the role of phase contrast and topology in the formation of stress/strain incompatibilities between soft and hard phases. Eventually, at a critical moment these incompatibilities are locally relaxed by nucleation of voids in the context of the ductile failure process. However, a critical question is, whether all these various mechanisms leading to void nucleation, involved at different length scales, are equally important for the global failure of the material. The answer to this question strongly depends on the intrinsic character of materials. Particularly, the global mechanical response of the polycrystalline materials is governed by its microstructure, which is of a statistical nature. Baring this in mind, it was observed that bainitic multiphase steels demonstrate a delay in damage initiation at the bainite/martensite interface compared to the first generation of advanced high strength steels (i.e. DP and IF steels), in which voids are nucleating at terminal stages of

deformation prior to the final failure. In chapter 5, it was shown that the failure of the material is not the direct consequence of earlier damage nucleation and even higher volume fraction of the nucleated voids but rather the deformation localization is the key factor leading to the global fracture. The meso-scale arrangement of the hard phase (martensite) determines whether or not the material goes through the deformation instability at earlier stage and thus fractures at lower strain levels. The martensite banding phenomenon demonstrates to have a detrimental effect on the global mechanical response of bainitic multiphase steels by promoting local shear band formation and thus deformation instability. The topology of martensite bands has two different effects: first on void nucleation activity, and second on promoting deformation instability. The coarser and more connected network of martensite bands results in a lower void nucleation activity while it causes earlier deformation localization. However, the finer and more fragmented networks of martensite bands leads to a higher void nucleation activity while it delays deformation localization.

*It is more important to study the meso-scale arrangement of the hard phase rather than local damage nucleation activity. This is due to the fact that martensite bands, as meso-scale heterogeneities, promote deformation instability while local damage activity is not essentially detrimental to global fracture behaviour of the material.*

Despite the vast efforts that have been spent to develop experimental and modelling tools to understand the role of micro-mechanical heterogeneities and their topology in damage nucleation, few methods have been proposed to resolve the crystallographic orientation aspect of damage initiation. In chapter 6, a new EBSD based method was examined to address the correlation between crystallographic orientation and void initiation. In this regard, 33 voids were analysed using the Orientation Distribution Function (ODF). By comparing the deformation texture at the uniform strain region (UODF) with the Voids-ODF (VODF), it was observed that after void nucleation, stress relaxation is rather governed by the growth process of voids than local plasticity around the voids. In other words, although voids act as stress concentrators, the stress is dominantly relaxed by the void growth process. Therefore, it is expected that VODF may reveal the orientations, in which damage will initiate from. However, it is important to mention that these orientations around voids experience some rotations during further plasticity. This is observed as a result of small deviation between VODF and UODF.

*Eventually, the ODF can be used to explain the mechanisms of stress relaxation after void nucleation. In addition, this post-mortem method can be used to study the correlation between the crystallographic orientation and damage initiation.*

Employing the VPSC model with the physical hardening model provides a strong tool to predict the anisotropic flow behaviour of bainitic/martensitic under various loading conditions. Although the VPSC model is not considered as a damage model among the continuum damage models, the model was used to predict the damage initiation sites in the Euler orientation space based on the evolution and partitioning of stress/strain components between orientations of polycrystalline aggregate. The model calculates the stress/strain components of each grain at any desired macroscopic strain level based on various parameters such as crystallographic orientation, dislocation density, grain size and phase fractions. Various components of the strain tensor were considered and it was shown that the  $\varepsilon_{23}$  component exhibits the highest difference (incompatibility) between all the simulated grains and phases. This strain component was visualised in the Euler orientation space in order to be compared with the VODF map. It was observed that the most damaged orientations coincide with maximum and minimum values of the  $\varepsilon_{23}$  strain component. However, this correspondence was not observed completely with the equivalent von Mises strain map. Therefore, this may explain the fact that in order to study damage initiation critical strain components that may induce damage need to be considered.

## Appendix A Transformation diagrams

### A.1 Continuous Cooling Transformation (CCT) diagrams

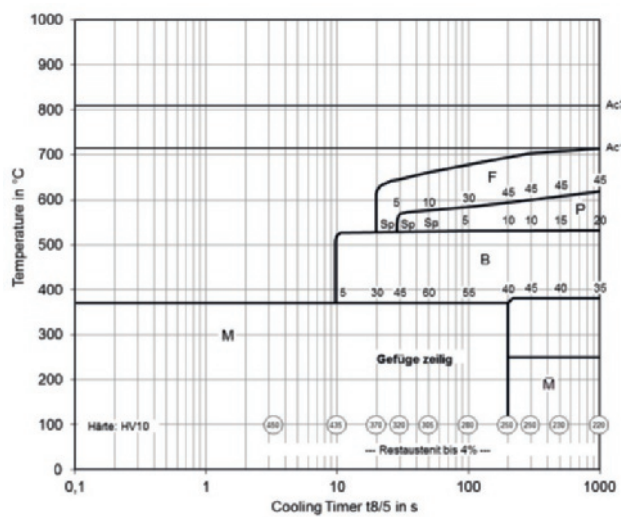


Figure. A.1 CCT diagram of LoSi grade. T8/5 means the time from 800°C to 500°C.

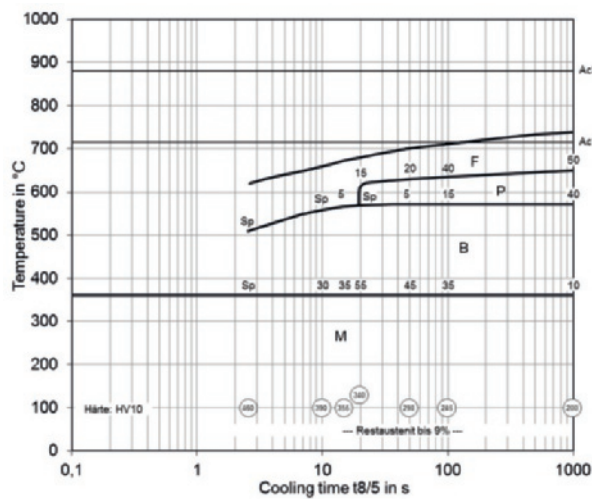


Figure. A.2 CCT diagram of HiSi grade. T8/5 means the time from 800°C to 500°C.

## A.2 Time Temperature Transformation (TTT) diagrams

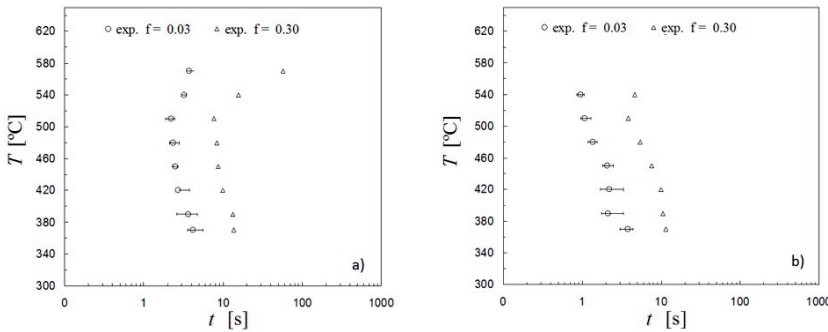


Figure. A.3 CCT TTT diagrams of isothermal transformation to bainite at different temperatures for (a) LoSi and (b) HiSi. F indicates the fraction.

## Acknowledgments

My PhD life with its all ups and downs now is ending, and thus, it is the moment to express my deepest gratitude towards people who have supported and influenced me in different ways. Here, I would like to first apologize to those whom I may forget to mention their names. Definitely, this letter cannot express fully my feelings and sense of gratitude to everyone.

First and foremost, I would like to state my deepest appreciations towards my promoter, Prof. L. A.I. Kestens. I have learned a lot from him not only scientifically but also from his patience, modesty and dedicative attitude. Our conversations, particularly during trips, with regard to my PhD work and its struggles always inspired me to go further and motivated me to overcome issues. His balanced criticality and pragmatic leadership, and great wisdom have always been a source of admiration for me. He treats his researchers not just as employees but as human beings, and his empathy provides a work atmosphere that has allowed me to develop myself independently both in my scientific thinking and as a human being.

Moreover, I would like to also express my appreciation to Prof. J. Sietsma. I still remember my first conversation with him, where his encouragement and personal hints, had significant impact on my decision to start my PhD. I would like to thank Dr. S. Ghodrat who played an important role in starting this project. I would like to appreciate also Prof. P. Verleysen from Ghent university of technology. Her cooperative and dedicative attitude to my work resulted in an interesting scientific collaboration. In addition, I would like to thank my daily supervisor, Dr. J. Galan Lopez. Our scientific discussions and his critical review has always opened a new insight into my work. I have learned a lot from his knowledge and analytical mind-set.

I would like to thank Dr. F. Hisker from ThyssenKrupp Germany and Dr. S.M.C. Van Bohemen from TATA steel Netherlands whom without their scientific contributions, I could not have accomplished this work. I would like to also thank Dr. D. J. Badiola from CEIT Spain, who has supported me scientifically and has been a source of encouragement to me. I want to thank Dr. V. Savran whose coordination and collaboration made my PhD project an excellently organised experience.

I am grateful to all my committee members Prof. A. van Bael, Prof. L. Delannay, Prof. R. Petrov to accept to read my thesis and take the effort to be my committee members and judge my PhD work. I would like to acknowledge TU Delft and the European Commission (EC) for funding my research project.



I would like to also thank my friends and colleagues; Mats, Constantinos, Maria, Alfonso, Ankit, Florian, Alexandra, Jun, Chrysa, Sudhee, Shahrzad, Wei, Tim, Marilia, Peter Klaver, Mohsen, Soroush and Nilgoon. Our daily social activities made my work atmosphere more joyful. I would like to specially thank Mohammad and Banafsheh whose friendship and support was unlimited to me. I would like to also specially thank Soheil and Pantea. I really cannot express my feeling with regard to their support and friendship in my difficult days during the last 4 years. I would like to particularly thank Konstantina. Her emotional support and deep thoughts were always sources of inspiration for me. Moreover, I would like to thank Fedra and our long friendship. Her adorable kindness and patience have always accompanied me. I would like to state my gratitude also to Dr. Hessam and Dr. Salemi for their supports and our constructive discussions. Many thanks go to Behshid who designed the thesis cover and I appreciate her kind heart.

Above all, I would like to thank my mother, father and my sister who supported me during my whole life. Special appreciation goes to my mother with whom I could share all of my moments since I have been living in the Netherlands. She is the symbol of patience and strength to me as an individual. In addition, without the support of my father I could not have the chance to pursue my professional life, and my lovely sister who has been my soul mate since I remember myself.

Behnam,

Delft March 2019



## **List of Publications**

1. Shakerifard. B, Lopez. J. G, Taboada Legaza. M. C, Verleysen. P, Kestens. L. A. I. Strain rate dependant dynamic mechanical response of bainitic multiphase steels. *Materials Science and Engineering A*, 2019, 745, 279-290, doi: 10.1016/j.msea.2018.12.105.
2. Shakerifard. B, Lopez. J. G, Hisker. F, Kestens. L. A. I. Effect of banding on micro-mechanisms of damage initiation in bainitic/martensitic steels. *Materials Science and Engineering A*, 2018, 735, 324-335, doi: 10.1016/j.msea.2018.08.049.
3. Shakerifard. B, Lopez. J. G, Hisker. F, Kestens. L. A. I. Crystallographically resolved damage initiation in advanced high strength steel. *Iop Conf Ser-Mat Sci*, 18th International Conference on Textures of Materials (Icotom-18), doi: Unsp 01202210.1088/1757-899x/375/1/012022.
4. Shakerifard. B, Lopez. J. G, Hisker. F, Kestens. L. A. I. A new methodology to study the role of crystallographic orientations in damage initiation mechanisms using a homogenization based CP model. To be submitted.
5. Shakerifard. B, Lopez. J. G, Kestens. L. A. I. A new electron backscatter diffraction-based method to study the role of crystallographic orientation in ductile damage initiation. Submitted to *Metals*.



# Curriculum Vitae

Behnam Shakerifard

Born 01 September 1989 in Mashhad, Iran

2007-2011 Bachelor: Industrial Metallurgy, Azad University of Tehran (Science and Research Branch), Iran.

Thesis title: *Annealing and microstructure characterization of a high temperature resistance steel used in reactors.*

2012-2014 Master: Materials Science and Engineering, Delft University of Technology, The Netherlands.

Thesis title: *Micro-mechanisms of hot cracking during dissimilar welding of oil/gas clad pipes.*

Supervisor: Prof. dr. ir. M. Hermans

2014-2018 PhD researcher: Materials Science and Engineering, Delft University of Technology, The Netherlands.

Thesis title: *From micro-mechanisms of damage initiation to constitutive mechanical behavior of bainitic multiphase steels.*

Promoter: Prof. dr. Ir. L. A. I. Kestens





